

Iterative Image Processing using a Cavity with a
Phase-conjugate Mirror : Possibilities and
Limitations

by

Kanwai Peter Lo

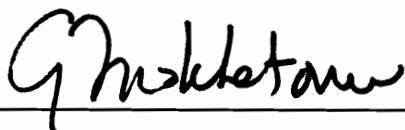
Dissertation submitted to the faculty of the
Virginia Polytechnic Institute and State University
in partial fulfillment of the requirements for the degree of

DOCTOR OF PHILOSOPHY

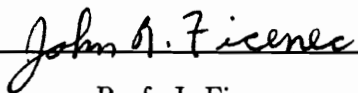
in

Physics

APPROVED:



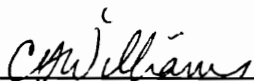
Prof. Guy Indebetouw, Chairman



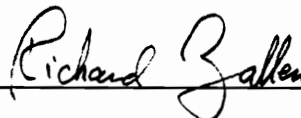
Prof. J. Ficenec



Prof. T. C. Poon



Prof. C. D. Williams



Prof. R. Zallen

September, 1991

Blacksburg, Virginia

Iterative Image Processing using a Cavity with a Phase-conjugate Mirror : Possibilities and Limitations

by

Kanwai Peter Lo

Committee Chairman: Prof. Guy Indebetouw

Department of Physics

(ABSTRACT)

An optical image feedback system utilizing a cavity with a phase-conjugate mirror (PCM) has been studied. A new theory, based on operators, is developed to describe the steady-state output of the cavity. The use of operators allows one to describe the various optical operations and transformations needed in the optical implementation of iterative algorithms. The characteristics of the cavity are discussed using an expansion of the cavity fields in the cavity eigenfunctions.

Several image processing applications using a PCM cavity are proposed and are studied using computer simulations. These theoretical studies indicate that a PCM cavity can be useful in many applications.

Optical phase conjugation was realized using a single crystal of photorefractive BaTiO₃ in a degenerated four-wave mixing geometry. The reflectivity gain from the PCM was optimized experimentally by the geometrical parameters and by the beam-intensity ratios. The ability of the PCM to remove phase distortion as predicted theoretically, was demonstrated experimentally.

The output of a PCM cavity can be substantially influenced by self-oscillations of the cavity above threshold. This was experimentally studied by observing the time evolution of the input. To avoid the influence of self-oscillation, the cavity must be operated below threshold. It is found that the cavity decay time constant diverges at and about threshold. This can be used as an indicator to show whether the cavity has crossed the threshold or to measure how close to threshold the cavity operates.

To verify that a PCM cavity can be used in iterative image processing, an experiment was set up to implement an image restoration scheme based on the Gerchberg

algorithm. It is shown that an optical implementation of the Gerchberg algorithm is feasible for objects made of few pixels. The experiment confirmed that image iteration in a PCM cavity is possible. The limitations of the cavity and the technical difficulties are discussed.

ACKNOWLEDGEMENTS

It is my honor and pleasure to acknowledge all the people who had helped me with the research and the write-up of this dissertation. A word of thank cannot repay the debt I owe them, but it demonstrates that my dissertation would not be possible without them.

First, I would like to express my deepest gratitude to my advisor Professor Guy Indebetouw for his guidance, support, and encouragement. He is my mentor, teacher, and friend. The hours that we spent on discussing Physics and optics have been the most insightful. This dissertation would not be possible without his help.

I am very grateful for the comments and encouragement from my graduate committee. I am thankful for all the care and encouragement from Prof. Clayton D. Williams and Prof. John Ficenec during the process of my job searching. I thank Prof. Tingchung Poon for motivating me to study optics. I thank Prof. Richard Zallen for teaching me Solid State Physics. His classes had given me new understanding on the optical properties of condensed matters.

I would like to thank Prof. Larry Burton and Prof. Jerome Long for letting me use their vacuum deposition equipment. I am grateful for the help of Warren Lewis who evaporated mirrors for my experiments.

I appreciate the kindness of Prof. Ianna of the University of Virginia who let me use his microdensitometer to scan the optical density of my experimental data. I am thankful for the help of Mr. Jonathan Lingel who taught me how to use the microdensitometer and helped me scan some of the data.

I thank the Jeffress Memorial Trusts and NASA for supporting my research.

I am very grateful for all the kindness and friendship of the supportive staff of the Physics department. I thank Dave Miller, Bob Ross, Melvin Shaver and John Miller from the machine shop who have made most of the accessories for my experiments. I thank Chris Thomas, Sheri Turner, Debbie Cruise, Judy Faw, and Lou Terhune who have taken care of all the paperwork during my study. I am also grateful for their willingness to help just when I needed.

I enjoy all the conversations and help from Caisy Ho, my fellow colleague and friend. We support each other with prayers during all these years. I am also grateful for my colleague Raymond Liu to whom I spend many hours in discussion.

I dedicate this dissertation to my wife, Alice, for her love and her selfless support during my graduate study. She cheers me up when I am down. She helps me when I need her the most. My graduate study would be much less enjoyable without her. I would also like to thank my parents for their love and support. I would not be in the United States if they did not encourage me to come. I am also very grateful for Prof. Y. A. Liu and Dr. H. H. Lo, they are like my parents in the United States.

Finally, I thank God and my Lord Jesus Christ for all the providence. He has given me strength to complete the degree, and He gives me peace during all the time of difficulties.

TABLE OF CONTENTS

1	Introduction	1
1.1	Why optical signal processing ?	3
1.2	Coherent optical feedback and iterative processing	3
1.2.1	Optical feedback system in information processing	4
1.2.2	Coherent optical feedback system	5
1.3	Difficulties and limitations of a conventional feedback system	7
1.3.1	Limitation due to losses	8
1.3.2	Limitation due to accumulation of phase error	8
1.4	Optical phase conjugation	9
1.5	Dissertation outline	11
2	Theory of a cavity with a PCM	13
2.1	Introduction	13
2.2	Cavity with one PCM : Operator Theory	14
2.2.1	Steady-state fields equations	14
2.2.2	Feedback parameter of the cavity	17
2.3	Characteristics and limitations	19
2.3.1	Double-path feedback loop	19
2.3.2	Feedback parameter	21
2.3.3	Phase cancellation	22
2.4	Conclusion	25

3 Application of a cavity with a PCM in image processing : Theoretical study and simulation	26
3.1 Introduction	26
3.2 Contrast control of an image	27
3.3 Image Restoration	31
3.3.1 Inverse filtering	32
3.3.2 Extrapolation of a band-limited function	35
3.3.3 Gerchberg Algorithm	36
3.3.4 Simulation of the Gerchberg algorithm	40
3.3.5 Optical implementation	44
3.4 Conclusion	48
4 Realization of a PCM with photorefractive BaTiO₃ : Theory and experimental investigation	50
4.1 Introduction	50
4.2 Photorefractive effect	51
4.2.1 Band-transport model	52
4.2.2 Photorefractive effect in BaTiO ₃	58
4.3 Phase conjugation using degenerated four-wave mixing in photorefractive BaTiO ₃	62
4.4 Optimization of the PCM gain	67
4.4.1 Optimization of the geometry	67
4.4.2 Optimization of the intensity ratios of the interacting beams	70
4.5 Experimental measurement of the PCM reflectivity	75
4.5.1 PCM reflectivity versus pumps ratio	78
4.5.2 PCM reflectivity against signal-to-pump ratio	80
4.5.3 PCM reflectivity against total beam intensity	80
4.6 PCM fidelity and stability	84
4.6.1 PCM fidelity	84
4.6.2 PCM stability	87
4.7 Conclusion	88

5	The transient behavior of a PCM cavity	89
5.1	Introduction	89
5.2	Effect on the output image quality when the PCM cavity is above the threshold of self-oscillation	90
5.3	Decay time of PCM cavity	93
5.4	Conclusion	96
6	Image resolution enhancement/ extrapolation : an example of the use of a cavity with a PCM in iterative processing	97
6.1	Experimental setup	98
6.1.1	General description	98
6.1.2	Object generation	100
6.1.3	Low-pass filter	100
6.1.4	The PCM cavity	102
6.1.5	Observation and recording of the image	104
6.2	Experimental results	106
6.3	Discussion	111
6.4	Conclusion	119
7	Summary	120
7.1	Recommendation	123

LIST OF FIGURES

1.1	A block diagram of an optical feedback system	6
1.2	An illustration of the removal of phase distortion by a PCM	10
2.1	Schematic diagram of a cavity with a PCM	15
2.2	Block diagram of the feedback cavity with a PCM.	18
2.3	Common path geometry of the Fabry-Perot cavity with a PCM	20
2.4	Two PCM cavity	23
3.1	Diagram of a setup for the optical implementation of contrast enhancement	28
3.2	The theoretical calculation of the contrast control using feedback	30
3.3	Diagram of a setup for the implementation of inverse filtering	33
3.4	Pictorial description of the Gerchberg algorithm	38
3.5	Comparison of the two-point object with the restored objects	41
3.6	Comparison of the power spectrum of the two-point object	42
3.7	A plot of the sum of absolute spectral error against the number of iterations using the Gerchberg algorithm	43
3.8	Comparison of the restoration of a three-point object	45
3.9	Comparison of the power spectrum of the restoration of a three-point object	46
3.10	Diagram of a setup for the optical implementation of the Gerchberg algorithm	47
4.1	The band-transport model	53

4.2	Wave vector diagram for two-wave mixing	57
4.3	Two-wave mixing Geometry	60
4.4	Degenerate four-wave mixing geometry	64
4.5	Wave vectors diagram for four-wave mixing	65
4.6	Plot of the coupling coefficient against the grating angle	69
4.7	Plot of the coupling coefficient against the signal beam angle	71
4.8	Contour plot of the PCM reflectivity versus log of signal-to-pump ratio and log of pump ratios	73
4.9	PCM reflectivity curves for various log signal-to-pump ratio	74
4.10	Experimental setup for the measurement of the PCM reflectivity	76
4.11	Expanded geometry of the interacting beams in four-wave mixing	77
4.12	Experimental measurement of PCM reflectivity against log pump ratios for fixed signal-to-pump ratio	79
4.13	Experimental measurement of PCM reflectivity against log signal-to- pump ratio for fixed pumps ratio	81
4.14	Experimental measurement of PCM reflectivity against total beam in- tensity for a fixed signal-to-pump ratio	82
4.15	Schematic experimental setup for the restoration of phase distortion	85
4.16	Demonstration of a phase distortion “healing” by a PCM	86
5.1	Schematic diagram of the experimental setup to observe the continuous evolution of an input image with the cavity is above threshold	91
5.2	Time sequence of evolution of the image in a PCM cavity above threshold	92
5.3	Typical rise and decay of the cavity field in a PCM cavity	94
5.4	Experimental measurement of the decay time constant in a PCM cavity versus the log of pumps ratio	95
6.1	Block diagram of the experimental setup	99
6.2	Diagram of the setup used to generate objects consisting of several lines	101
6.3	Schematic diagram of the optical cavity used to implement the Gerch- berg algorithm	103

6.4	Plot the photographic density versus input intensity for T-max film developed in Kodak D-76 developer	105
6.5	Setup used for the experimental implementation of the Gerchberg algorithm	107
6.6	Trace through the intensity distribution of the degraded image of a input and the restored image	109
6.7	Output at port 1 showing the extrapolated spatial frequency spectrum	110
6.8	Trace through the intensity distribution of the degraded image of a input and a restored image using a one-path geometry	112
6.9	Experimental result of the restoration of a three-pixel object using a one-path geometry	113
6.10	Diagram of the setup used to observe the competition of two sets of gratings in the same interaction region of the PCM	116
6.11	Results of an experiment showing the competition between a strong and a weak signal sharing the same interaction region in the PCM . .	118

LIST OF TABLES

4.1	Material parameters used for the calculations	59
-----	---	----

Chapter 1

Introduction

The purpose of this study is two-fold : to explore the possibility of using a Fabry-Perot cavity with one phase-conjugate mirror (PCM) for iterative image processing, and to test this possibility experimentally by implementing a specific image restoration algorithm.

An optical system with feedback makes spatial image processing analogous to the use of electronic feedback possible [1, 2]. Such a device would offer the possibility of performing two-dimensional iterative processing in real time. Some of the iterative algorithms have shown outstanding performances in solving signal recovery and restoration problems [3, 4, 5, 6] as well as in accomplishing signal recognition and selection tasks [7, 8, 9].

An optical implementation of iterative algorithms requires feedback and gain. The performances of passive, conventional feedback systems are limited by cavity losses and by accumulation of phase error from each round-trip [10]. Several methods have been used to achieve optical gain. They include stimulated emission amplification [1, 11, 12], and two-wave mixing in photorefractive materials [13, 8, 9, 14]. The problem of phase error accumulation, however, remains formidable, especially in devices with feedback operating close to threshold of self-oscillation.

In this project, a PCM is used in an optical feedback loop to alleviate some of these

problems simultaneously. In principle, a PCM can introduce gain to the feedback signal, compensate for the cavity losses, and restore the phase of the wavefront after each pair of round-trips [15, 16, 17]. It thus provides an environment to implement feedback algorithms without accumulation of phase errors.

To build such a cavity, a semi-transparent mirror, a PCM, and other intra-cavity elements such as lenses and filters are used as the basic components. The mirror and the PCM act as the image feedback devices. The intra-cavity elements are used to implement the necessary optical transformations and filtering for different applications. Due to the use of a PCM, the properties of the cavity differ from a conventional cavity in many aspects. It is therefore important to understand the characteristics of a PCM cavity, and how these characteristics affect the implementation of image-processing algorithms.

Optical phase conjugation can be realized using many media and methods [18, 19]. Among them, the four-wave mixing geometry in photorefractive material [20, 21] is chosen to implement the PCM. The criteria for this choice will be discussed. Since optical gain is required in the feedback, the performance of the PCM is evaluated. The optimization of its gain will be studied experimentally and its ability to restore phase aberration will be demonstrated.

To demonstrate that a PCM cavity can be used in iterative processing, an image restoration algorithm based on the Gerchberg algorithm [22] will be implemented optically in such a cavity. This experiment serves as a test of this idea. Some of the limitations of the cavity will emerge and will be discussed.

This chapter serves as an introduction to the present study. In section 1.1, the motivations for using optics in general to process data is discussed. An optical system with feedback is found to have many uses, and its classification and some of the applications are summarized in section 1.2. Some of the limitations of implementing iterative procedures in a conventional cavity are discussed in section 1.3. Some of the basic properties of a PCM will be discussed in section 1.4. In section 1.5, the outline of this dissertation is described.

1.1 Why optical signal processing ?

Processing signals by optical means was first motivated by the vast amount of data obtained by radars and used in making maps, and by the similarity between the technique used to process these data and optical processing techniques [23]. The field greatly benefitted from the invention of the laser and the development of off-axis holography in the early 1960s [24]. Many successful coherent optical processing techniques are direct consequences of these inventions. Some of the outstanding achievements, to name just a few examples, are found in pattern recognition [25, 26], numerical processing [27], and optical transformation [28, 29].

While many of the above processing techniques can be performed by an electronic computer, several merits still make optical signal processing appealing [30]. First, the two-dimensional format is suitable for image handling and manipulation. There is no need for image sampling and quantization as in digital electronic computers. Secondly, a typical optical processor has two (spatial) degrees of freedom. Massive optical communication in a parallel sense is possible, avoiding the bottle neck of a conventional Von Neumann type of computer [30]. The trade-off in using an optical processor is usually in the lack of flexibility in implementing optical processes (it cannot be easily programmed) and the lower accuracy (analog devices cannot deal with noise as efficiently as digital computers).

1.2 Coherent optical feedback and iterative processing

The term “feedback” in an electronic circuit is well known : It means that a portion of the output electrical signal is being combined with the input signal and returned to the circuit. In an optical feedback system, a portion of the output image is modified by a feedback optical system, combined with the input, and then returned to the forward optical system [1]. The closed-loop feedback system thus produces transfer characteristics which would be impossible or would be difficult to achieve in a non-recursive optical system.

1.2.1 Optical feedback system in information processing

The methods for processing an image optically can be classified into coherent, incoherent, and hybrid optical processing techniques. In a coherent optical feedback system, the coherence length of the light source is many times longer than the round-trip path length of the cavity. This allows a definite phase relationship between the feedback and the input fields. In a conventional feedback cavity the phase relationship depends on the round-trip length of the cavity. To vary the phase of the feedback signal, the cavity length is tuned to provide a positive, negative, or complex feedback [6]. Both positive and negative feedback have been found useful in image processing [31, 3]. Several applications in image restoration, contrast control, the analog solution of partial differential equations [6, 32, 33], and matrix inversion [34] have been demonstrated optically.

In an incoherent optical feedback system, the coherence length of the source is shorter than the round-trip length of the cavity. Therefore the feedback image is added to the input in intensity, not amplitude. These systems are limited to positive feedback [35].

In a hybrid feedback system, incoherent or coherent light is used in the processing and electronics is used in the feedback loop. The use of television electronics or spatial light modulators can easily achieve contrast reversal and can therefore implement positive or negative feedbacks. These hybrid implementations of optical and electronic elements have a wide range of applications. Some examples are found in space-variant processing, ghost image elimination, and in edge and contrast enhancement [36, 37, 38].

It is difficult to determine whether a coherent imaging system is superior to an incoherent or a hybrid system. The result of any such comparison depends on the applications [39]. However, from the standpoint of linear filtering operations, a coherent illumination is often simpler and more flexible [39]. Furthermore, positive and negative feedback can be more easily achieved in a coherent system without additional pieces of equipment. It is for these reasons that the work mentioned here focuses on

the coherent feedback option.

1.2.2 Coherent optical feedback system

The relation of the output $E_o(x', y')$ of an optical system to an input field $E_i(x, y)$ can be described by

$$E_o(x', y') = \iint_{Aperture} S_1(x, y; x', y') E_i(x, y) dx dy, \quad (1.1)$$

where the kernel $S_1(x, y; x', y')$ of the integral is called the impulse response of the optical system. For simplicity, the integral is represented by an operator

$$\hat{S}_1 \equiv \iint_{Aperture} S_1(x, y; x', y') dx dy. \quad (1.2)$$

An optical system is said to be space-invariant if its impulse response $S_1(x, y; x', y')$ depends only on the distances $(x - x')$ and $(y - y')$. The kernel is written simply as :

$$S_1(x, y; x', y') = S_1(x - x', y - y'). \quad (1.3)$$

The physical meaning of this equation is that the image of a point-source object changes only in location, not in functional form, as the point source spans the object field [39].

Using these notations, an optical feedback system can be represented by the block diagram of figure 1.1. The two-dimensional field amplitude distribution E_i is the input to the system, which consists of the forward operator \hat{S}_f and the feedback operator \hat{S}_b . The optical operators are assumed to be linear and space-invariant optical systems which may include lenses, filters etc. The output E_o of the feedback system is related to the input by the simple relationship

$$E_o = \hat{S}_f(E_i + \beta \hat{S}_b E_o), \quad (1.4)$$

where β is the feedback parameter of the system. In image processing applications, it is assumed that these optical operators contain imaging elements such that the output E_o is re-imaged pixel to pixel onto E_i .

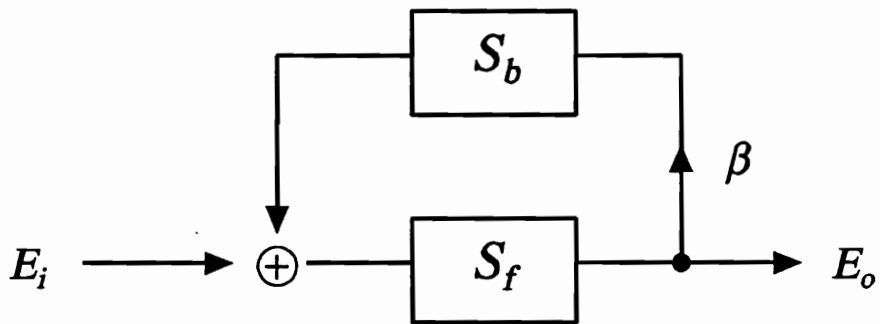


Figure 1.1: A block diagram of an optical feedback system. It consists of a forward and feedback optical system represented by operator \hat{S}_f and \hat{S}_b , respectively. The transfer characteristic of the feedback system is difficult to achieve or not assessable in a linear-optical system

If we assume that these operators commute (with some justifications in section 2.3.3 and 3.3.3) and that their eigenfunctions ϕ_n form a basis for a class of functions that includes E_i and the output E_o of the feedback system, then

$$\begin{aligned} E_j &= \sum_n e_{jn} \phi_n \quad ; j = i, o, \\ \hat{S}_l \phi_n &= \lambda_{ln} \phi_n \quad ; l = f, b. \end{aligned} \quad (1.5)$$

On substituting equations 1.5 into equation 1.4, the relationship between the input and the output coefficients is given by

$$e_{on} = \lambda_n e_{in}, \quad (1.6)$$

where the eigenvalues λ_n of the closed loop system are given by

$$\lambda_n = \frac{\lambda_{fn}}{1 - \beta \lambda_{fn} \lambda_{bn}}. \quad (1.7)$$

The conditions for this analysis to be valid are that the eigenfunctions of the operators must be orthogonal and form a complete set. Furthermore, to be able to process more or less arbitrary inputs, the mode structure of the cavity must be rich enough to represent arbitrary field amplitude distributions. One way of insuring this in a conventional resonator is to require that the eigenvalues (λ_{fn} and λ_{bn}) are all positive and nonzero [31, 40]. This means that the kernel of the integral equation is Hermitian. If λ_{fn} and λ_{bn} are not single signed, then according to equation 1.7, the feedback may be negative for some modes and positive for others, depending on the sign of the product of the eigenvalues [31]. In this case, the cavity will support only eigenmodes with positive product $\lambda_{fn} \cdot \lambda_{bn}$, thus restricting severely the type of input that can be processed.

1.3 Difficulties and limitations of a conventional feedback system

The performance of a passive, conventional feedback system is limited by the cavity losses and by the accumulation of phase errors in each round-trip. These two points are elaborated in the following sections.

1.3.1 Limitation due to losses

In a passive feedback system, the feedback signal is extracted from the cavity either by plane mirrors [6] or by spherical mirrors [41, 42, 43]. The output of the feedback system is usually through the same semi-transparent feedback mirror. As a result, only a fraction < 1 of the cavity field is being fed back and combined with the input. A similar situation occurs at the input mirror plane. These losses, together with the losses in the intra-cavity elements, grow geometrically with the number of round-trips. In systems where diffractive elements (such as holograms which typically have less than a few percent efficiency) are needed, the performance of an optical feedback system is severely limited by small effective number of round-trips.

Several methods have been proposed to achieve optical gain. They includes stimulated emission amplification [11, 12], two-wave mixing [13] and four-wave mixing [8, 9] in photorefractive materials.

1.3.2 Limitation due to accumulation of phase error

Since the feedback image adds coherently to the input, the phase errors in the feedback image become important. At each round-trip in the cavity, these phase errors accumulate and propagate to the next iteration. The sum of these phase errors modifies the transfer function of the optical feedback system and limits the performance of the optical processor.

Some improvements have been made in optical feedback system design in order to reduce the effect of phase errors. An example is the use of a spherical mirror to replace the combination of a plane mirror and a lens as the feedback device [41, 44]. By reducing the number of optical elements in the cavity, the amount of phase error accumulated in each round-trip can be reduced to less than $\pi/5$ in each round-trip [43]. This limits the number of effective round-trips to about 10 since a phase error of π is unacceptable. In applications which require a large number of iterations, the problem of phase errors remains. Examples which require many iterations include super-resolution [10], and restoration of noisy images [4].

1.4 Optical phase conjugation

Optical phase conjugation is a process which produces a wavefront reversal (figure 1.2) via non-linear optical effects. A device which performs optical phase conjugation is called a PCM (phase-conjugate mirror) or a wavefront reversal mirror. The “reflected” beam from a PCM is a phase-conjugate version of the incident beam which propagates backward.

The main attractive feature of a PCM is its ability to remove phase distortion. This ability can be understood through the following example. A forward-propagating plane wave can be represented by

$$E_f(\vec{r}, t) = \frac{1}{2} A_f(\vec{r}) e^{i(\vec{k} \cdot \vec{r} - \omega t)} + \text{complex conjugate (c.c.)}, \quad (1.8)$$

where $A_f(\vec{r})$ is the slowly varying complex scalar amplitude of the field $E_f(\vec{r}, t)$. Mathematically, the reversed wavefront $E_r(\vec{r}, t)$ is represented by the complex conjugate of the spatial part and is given by

$$E_r(\vec{r}, t) = \frac{1}{2} A_f^*(\vec{r}) e^{i(\vec{k} \cdot \vec{r} + \omega t)} + \text{c.c.} \quad (1.9)$$

The reversed wavefront will have an amplitude distribution the complex conjugate of that of the incident wave and it propagates in the reversed direction. Comparing equation 1.8 and equation 1.9, one can also obtain E_r by replacing t by $-t$. This is the reason why the optical phase conjugation is sometimes referred to as a time-reversal operation.

The distortion removal property of a PCM is illustrated in figure 1.2. A monochromatic plane wave (1) is incident on a non-uniform medium described by the electric permittivity $\epsilon(\vec{r})$. Assume that $\epsilon(\vec{r})$ is real, which represents a passive, non-absorptive medium (for example, a lens or turbulent atmosphere). After passing through the distorting region, the distorted wave (2) enters the PCM. The phase-conjugate wave (3) returns through the same distortion and emerges from the medium without distortion (4). The ability of this time-reversal wavefront to correct the phase distortion can be visualized by realizing that both the forward and reversed wave satisfy the

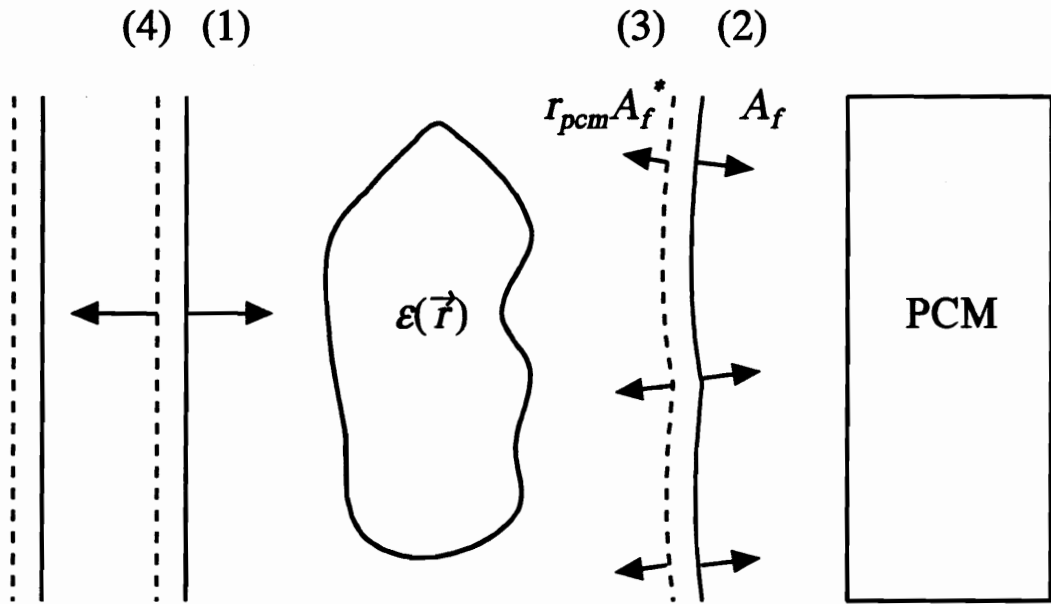


Figure 1.2: An illustration of the removal of phase distortion by a PCM. The PCM is assumed to be ideal with infinite dimension, so that all the scattering can be returned back to the scatterer. The PCM's amplitude reflectance is assumed to be homogenous and is being represented by a complex number r_{pcm} and a complex conjugate operation.

same wave equation in the region on the left of the PCM. The wave equation in this region can be described by

$$\nabla^2 E + \omega^2 \mu \varepsilon(\vec{r}) E = 0. \quad (1.10)$$

On substituting E from equation 1.8 into equation 1.10, and using the slowly varying amplitude approximation, the equation is simplified to

$$\nabla^2 A_f + [\omega^2 \mu \varepsilon(\vec{r}) - k^2] A_f - 2i\vec{k} \cdot \vec{\nabla} A_f = 0. \quad (1.11)$$

Since the field E_r also satisfies the same wave equation and propagates in the reverse direction of E_f , the emerging field from the distorting medium is, therefore, undistorted.

1.5 Dissertation outline

In chapter two, the theory of a Fabry-Perot cavity with one ideal PCM is developed. The steady-state output of this feedback cavity is studied. By making appropriate assumptions, the transfer characteristics of the cavity are determined. The properties of a PCM cavity are illustrated by using some realistic examples.

One of the ways to study the possibility of using a PCM cavity in image processing is by studying some applications. Some examples are discussed theoretically in chapter three. These examples serve to demonstrate the use of a PCM cavity in a large variety of applications but they are not exhaustive. These applications include contrast enhancement, inverse filtering, and restoration of a band-limited image. Among these examples, a restoration scheme based on the Gerchberg algorithm [22] is studied in detail. The results of computer simulations are presented.

In chapter four, the realization of the optical phase conjugation is demonstrated experimentally. A theory of the generation of the phase-conjugate beam in photorefractive materials using a four-wave mixing geometry is outlined, and the experimental setup for the PCM is shown. Since gain is necessary in an optical feedback system,

the reflectivity gain from the PCM needs to be optimized. The optimization procedure includes geometrical and parametrical factors which are studied separately. The ability of the PCM to remove phase distortion is demonstrated. Since a long term stability of the reflectivity of the PCM is desired, methods are discussed to achieve a relatively stable output.

The presence of a PCM in the feedback cavity alleviates problems of losses and phase errors in the use of feedback in optical processing. However, due to the gain from the PCM, the cavity becomes active. Since this is also a non-linear feedback system, it has a potential for self oscillation and can exhibit chaotic behavior. This is clearly not a desirable attribute in image processing. In chapter five, the effect of self oscillation to the output of the cavity will be shown. Another interesting phenomenon concerning the dynamics of this cavity is that the decay time of such a cavity diverges near the threshold of self-oscillation. Some observations of this interesting phenomenon are made. This cavity behavior can be used to indicate whether the cavity is above threshold.

The experimental details of an optical implementation of an iterative algorithm in a PCM cavity is described in chapter six. The iterative algorithm is based on the Gerchberg algorithm to improve the resolution of a low-pass image. The results of the experiment indicate that some improvements are achieved. Some practical aspects and the limitations of the system are identified.

Finally, chapter seven summarizes the project. Some of the limitations of the cavity are stated which may provide some guidance for the continuation of this project.

Chapter 2

Theory of a cavity with a PCM

2.1 Introduction

There is not much written in the literature on the use of a PCM cavity in iterative image processing. General descriptions of the cavity do not go far enough to incorporate the image processing capability of such a cavity [15, 16, 17]. It is therefore the objective of this chapter to develop a general theory of the cavity with a PCM, based on operators (section 2.2). The use of operators accommodates various optical operations and transformations needed in the optical implementation of iterative algorithms.

Some of the characteristics of a PCM cavity useful to image processing have already been discussed by other authors. For example, AuYeung *et al* [15] and Belanger *et al* [45] have pointed out that if the PCM is perfect, any distribution which can be phase conjugated is able to oscillate and is thus an eigenmode of the cavity. Thus the cavity allows an arbitrary input image to oscillate and is well suited to implement image processing algorithms. AuYeung *et al* [15] have pointed out that an arbitrary field used as input to the cavity will reproduce itself after two round-trips, which indicates that a PCM cavity needs to be described using a two-path geometry (as will be shown in section 2.3) when it is used in image processing. Lam and Brown [46]

have shown that the phase of the feedback does not depend on the cavity length but on the relative phase due to the PCM. Therefore, to change the phase of the feedback, one needs to alter the phase of the amplitude reflectance from the PCM (section 2.2.2), and not the cavity length as in a conventional cavity. In section 2.3, additional characteristics due to the presence of the PCM in the cavity are discussed. The cavity's peculiarities and characteristics are demonstrated with examples. Some limitations of using such a cavity in the area of image processing are presented.

2.2 Cavity with one PCM : Operator Theory

In this section, an analysis leading to the steady-state field equations and the transfer function of the cavity is presented.

2.2.1 Steady-state fields equations

A Fabry-Perot cavity with one conventional mirror M and a PCM is shown in figure 2.1. The input E_i' is from the left and the output E_o is the field transmitted by the cavity. The transmission and reflection on the input mirror, which may include 2-D masks or filters, are represented by the operators \hat{T} and \hat{R} respectively. The PCM, which is assumed ideal, is represented by a reflectivity operator $\hat{\mu}_i$, with $i = 1$ or 2 at locations 1 or 2 :

$$\hat{\mu}_i = r_{pcm_i} \hat{p}c = |r_{pcm_i}| \exp(\psi_{pcm_i}) \hat{p}c \quad i = 1, 2. \quad (2.1)$$

In this expression, r_{pcm_i} is the steady-state, complex amplitude reflectance of the PCM at the locations $i = 1$ or 2 , and ψ_{pcm_i} is the phase term introduced by the PCM. The operator $\hat{p}c$ denotes a phase conjugation operator. The phase ψ_{pcm_i} depends on the phase conjugation mechanism. For example, in degenerate four-wave mixing (section 4.3) using a photorefractive material (e. g. $BaTiO_3$), the phase of the PCM reflectance, with negligible absorption and assuming a real coupling constant,

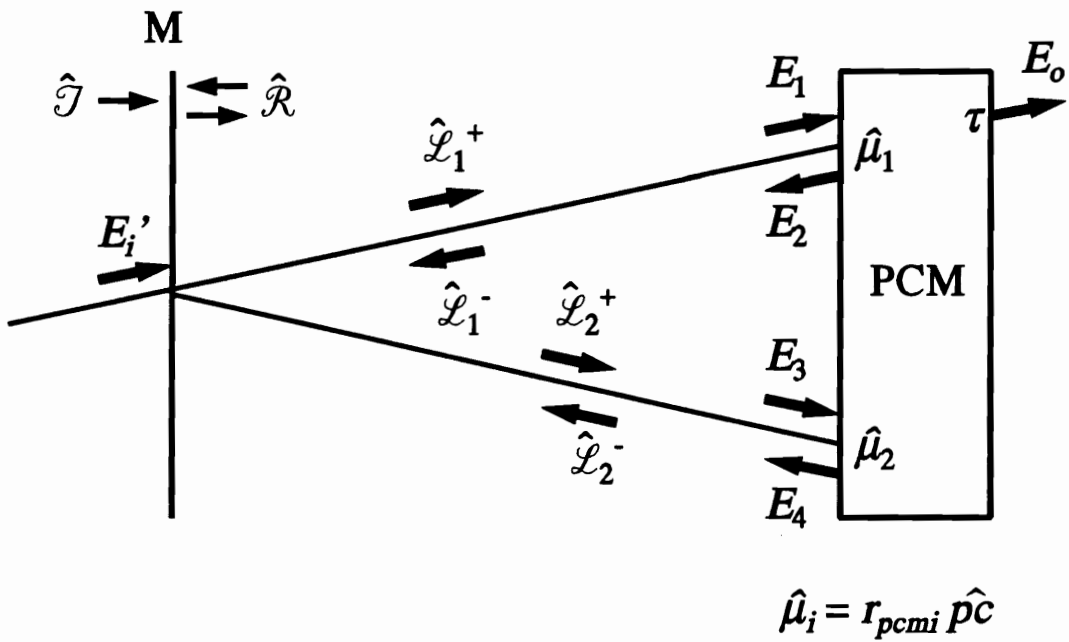


Figure 2.1: Schematic diagram of a cavity with a PCM. The transmission and reflection on the mirror are represented by the operators \hat{T} and \hat{R} the reflectivity of the PCM is characterized by the operators $\hat{\mu}_i$. The operators \hat{L}_i^\pm describe the transfer of the optical field from the input mirror to the PCM and back along the primary and the secondary path, respectively.

is simply given by the sum of the phases of the pump beams [47] :

$$\psi_{pemi} = \phi_{1i} + \phi_{2i}. \quad (2.2)$$

An expression for the steady-state output of the cavity shown in figure 2.1 is now derived. It is assumed that the field propagates in the cavity along two separate paths. The primary path contains the counter-propagating fields E_1 and E_2 . The secondary path contains the fields E_3 and E_4 . These fields are defined at the entrance plane of the PCM. Note (from figure 2.1) that the field E_1 results from the summation of field contributions which have been phase conjugated an even number of times while the field E_3 is the sum of contributions having experienced an odd number of phase conjugations. As will be discussed in the next section, the purpose of the two distinct paths is to allow for the spatial separation of these two fields.

The field transformations from the entrance mirror M to the PCM and back along the primary and the secondary paths are described by the four linear operators $\hat{\mathcal{L}}_i^\pm$, $i=1, 2$. These operators may include e.g. : free space propagation, Fourier transformations, spatial masks or spatial frequency filters...etc [3].

The steady-state fields satisfy the following boundary conditions :

$$\begin{aligned} E_1 &= E_i + \hat{\mathcal{L}}_1^+ \hat{\mathcal{R}} \hat{\mathcal{L}}_2^- E_4 \\ E_2 &= \hat{\mu}_1 E_1 \\ E_3 &= \hat{\mathcal{L}}_2^+ \hat{\mathcal{R}} \hat{\mathcal{L}}_1^- E_2 \\ E_4 &= \hat{\mu}_2 E_3, \end{aligned} \quad (2.3)$$

where E_i is related to the input field E_i' defined at the input mirror M by

$$E_i = \hat{\mathcal{L}}_i^+ \hat{\mathcal{T}} E_i'. \quad (2.4)$$

On substituting in equation 2.3, the following fields equations for E_1 and E_3 are obtained :

$$E_1 = E_i + \hat{\mathcal{L}}_1^+ \hat{\mathcal{R}} \hat{\mathcal{L}}_2^- \hat{\mu}_2 \hat{\mathcal{L}}_2^+ \hat{\mathcal{R}} \hat{\mathcal{L}}_1^- \hat{\mu}_1 E_1, \quad (2.5)$$

$$E_3 = \hat{\mathcal{L}}_2^+ \hat{\mathcal{R}} \hat{\mathcal{L}}_1^- \hat{\mu}_1 E_1. \quad (2.6)$$

If the output is taken as the field E_1 transmitted by the PCM at location 1, that is :

$$E_o = \tau E_1, \quad (2.7)$$

where τ is the PCM transmittance, the steady-state output expression is found to be :

$$E_o = \tau E_i + \hat{\mathcal{L}}_1^+ \hat{\mathcal{R}} \hat{\mathcal{L}}_2^- \hat{\mu}_2 \hat{\mathcal{L}}_2^+ \hat{\mathcal{R}} \hat{\mathcal{L}}_1^- \hat{\mu}_1 E_o. \quad (2.8)$$

Figure 2.2 shows the conventional block diagram of the feedback system described by equation 2.8.

2.2.2 Feedback parameter of the cavity

In this section, the feedback parameter β of the cavity with a conventional semi-transparent input mirror is determined.

The input mirror M combines the input image with the feedback image. The phase of the feedback ψ determines the type of feedback. As in electronics, $\psi = 2m\pi$ is positive feedback and $\psi = (2m + 1)\pi$ is negative feedback, where m is an integer. For other values of ψ , complex feedback is achieved.

If the input mirror M is a conventional semi-transparent mirror with transmission and reflection coefficients t and r respectively, equation 2.8 takes the simpler form

$$\begin{aligned} E_o &= \tau E_i + \beta \hat{\mathcal{L}}_1^+ \hat{\mathcal{L}}_2^- \hat{p}c \hat{\mathcal{L}}_2^+ \hat{\mathcal{L}}_1^- \hat{p}c E_o, \\ E_o &= \tau E_i + \beta \hat{\mathcal{O}} E_o. \end{aligned} \quad (2.9)$$

where the operator $\hat{\mathcal{O}}$ is recognized as the feedback loop operator which consists of a double round-trip in the cavity, and the feedback parameter β is defined as

$$\beta = |r|^2 r_{pcm1}^* r_{pcm2} = |r|^2 |r_{pcm1}| |r_{pcm2}| e^{i\psi}. \quad (2.10)$$

The phase ψ of the feedback parameter is given by $\psi = -\psi_{pcm1} + \psi_{pcm2}$, where ψ_{pcm1} and ψ_{pcm2} are the phases of PCM reflectance at location 1 (primary path) and 2

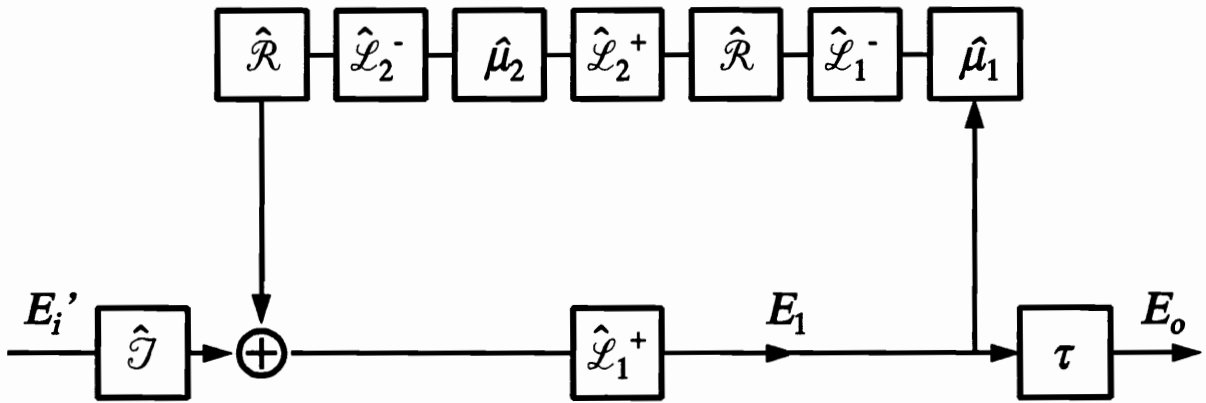


Figure 2.2: Block diagram of the feedback cavity with a PCM.

(secondary path), respectively. On substituting equation 2.2 into the phase of the feedback parameter (equation 2.10), the phase ψ is found to be

$$\psi = \phi_{12} + \phi_{22} - \phi_{11} - \phi_{21}. \quad (2.11)$$

It is seen that the phase ψ of the feedback is composed of the phases of the pump beams at location 1 and 2. This offers the possibility of controlling the phase of the feedback parameter through the phase of the pump beams.

2.3 Characteristics and limitations

In this section, three unique characteristics of the PCM cavity of figure 2.1 are highlighted and their consequences discussed.

2.3.1 Double-path feedback loop

The feedback loop operator in equation 2.9 includes two round-trips in the cavity. In the PCM cavity of figure 2.1, where the two paths are spatially separated, the output given by equation 2.7 includes only the field contributions which have been phase conjugated an even number of times. If the two paths overlap, the output must be taken as the superposition of the fields E_1 and E_3 . In general, these two fields interfere and the output is not a simple function of the input.

An example is shown in figure 2.3. If the lens inside the cavity is one focal length away from the input mirror and from the PCM, the transfer operators are given by

$$\hat{\mathcal{L}}^{+(-)} = e^{ikl^{+(-)}} \hat{\mathcal{F}}, \quad (2.12)$$

where $\hat{\mathcal{F}}$ is a Fourier transform operator, and $l^{+(-)}$ is the cavity optical length for the forward (backward) path.

On substituting from equation 2.12 into equation 2.5, using an input mirror with transmittance and reflectance t and r respectively, and using the fact that the successive application of two Fourier transform operators $\hat{\mathcal{F}}\hat{\mathcal{F}}$ is nothing but an inversion

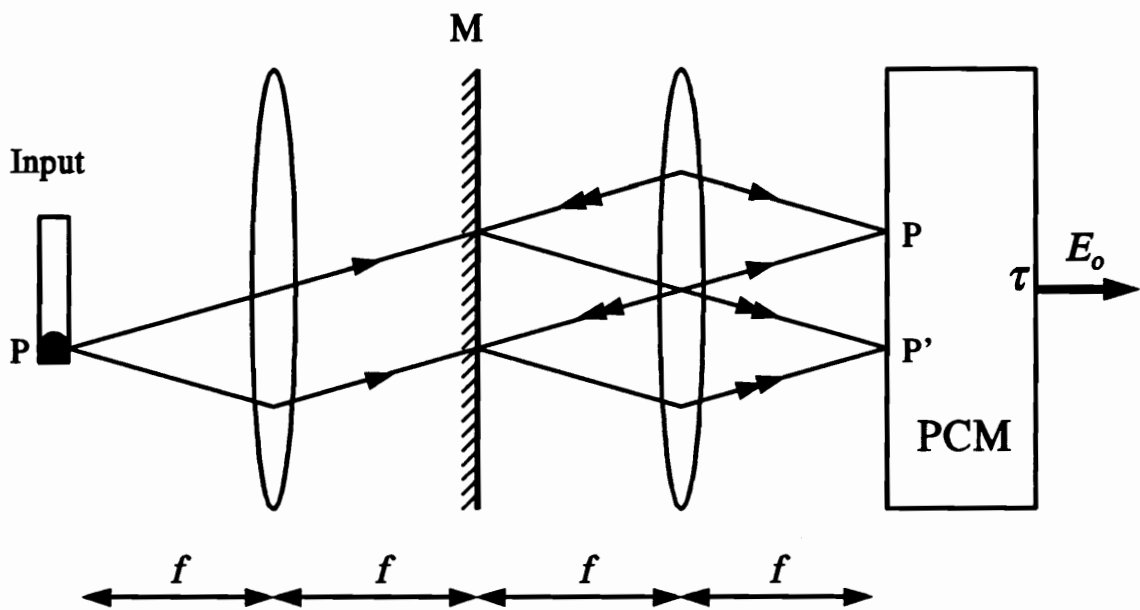


Figure 2.3: Common path geometry of the Fabry-Perot cavity with a PCM. The output of the cavity is $E_o = \tau (E_1 + E_3)$, and E_1 is proportional to the input while E_3 is proportional to the phase conjugate of the inverted input.

of coordinates, the cavity fields are found to be

$$\begin{aligned} E_1(x, y) &= E_i(x, y) + \beta E_1(x, y) \\ E_3(x, y) &= \tau r_{pcm1} e^{ikl} E_1^*(-x, -y) \end{aligned} \quad (2.13)$$

where $l = l^+ + l^-$ is the round-trip optical path length of the cavity, and β is given by equation 2.10. The output of the cavity is the sum of the cavity fields E_1 and E_3 :

$$\begin{aligned} E_o(x, y) &= \tau [E_1(x, y) + E_3(x, y)] \\ &= \frac{\tau}{1 - \beta} E_i(x, y) + \frac{\tau r r_{pcm1} e^{ikL}}{1 - \beta^*} E_i^*(-x, -y). \end{aligned} \quad (2.14)$$

It is seen that the output is a superposition of a field proportional to the input $E_i(x, y)$ and a field proportional to the phase conjugate of a coordinate inverted input $E_i^*(-x, -y)$. This particularity of a PCM cavity output has been found very useful to realize self-referencing and inverting interferometers [48]. It can also be used to produce holograms, or to perform multiple transforms simultaneously.

In image processing, however, this superposition of several fields at the output is, in general, not wanted. One way to avoid this problem is to provide for two distinct and spatially separated paths in the cavity, as was assumed to be the case in the previous section (figure 2.1). Another way is to use an input which occupies only one quadrant of the input field and to synthesize a Hermitian cavity input satisfying $E_i(x, y) = E_i^*(-x, -y)$. The third way is to use a unidirectional ring cavity as described by Klumb *et al* [49].

2.3.2 Feedback parameter

The second important characteristic of the PCM cavity is that the phase of the feedback parameter is determined by the phase difference of the PCM reflectance at two different locations (equation 2.10), unlike that of a conventional cavity in which the feedback parameter depends only on the cavity length.

In principle, it is possible to control the phase of the feedback parameter by controlling the phases of the pump beams at the two locations 1 and 2 (figure 2.1). In

practice, however, it may not be easy to change the phases of the amplitude reflectance at these locations independently. It is particularly difficult for a cavity which uses a photorefractive BaTiO₃ crystal as the PCM. In a typical four-wave mixing experiment to realize optical phase conjugation in a photorefractive material (section 4.3), only one interaction region is established by the set of counter-propagating pumps. The phase of the reflectance will be the same at location 1 and 2 because they share the same pumps in the interaction region. If the PCM reflectance of the primary and the secondary path have the same phase, the feedback parameter becomes $\beta = |r|^2 |r_{pcm1}| |r_{pcm2}|$, which is a real positive number. Thus, in this particular case, the cavity feedback is always positive.

One possible geometry, which may make it easier to control the phase of the PCM reflectance independently for the two paths, is obtained by unfolding the cavity into a two-PCM cavity, as shown in figure 2.4. The steady-state output of this cavity is again given by equation 2.9. The only difference is that, in the expression of the feedback parameter (equation 2.10) the beam-splitter transmittance replaces the input mirror reflectance.

2.3.3 Phase cancellation

The third characteristic of the PCM cavity to be discussed is a direct consequence of the phase healing property of the PCM. As already mentioned, this is necessary to avoid phase error accumulations in the cavity, but it seriously restricts the kinds of operations that the system can perform since it also cancels the phase included in the operations

For example, any phase filtering operation will be canceled. To show this, let us assume that the transfer operators in both paths represent complex spatial filtering operations, that is :

$$\hat{\mathcal{L}}_i^{+(-)} = e^{ikl_i^{+(-)}} \hat{\mathcal{F}} \hat{\mathcal{S}}_i \hat{\mathcal{F}}, i = 1, 2 \quad (2.15)$$

where $l_i^{+(-)}$ is the forward (backward) optical path length along path i and $\hat{\mathcal{S}}_i$ is an operator representing the transmission of the field through a filter with a complex

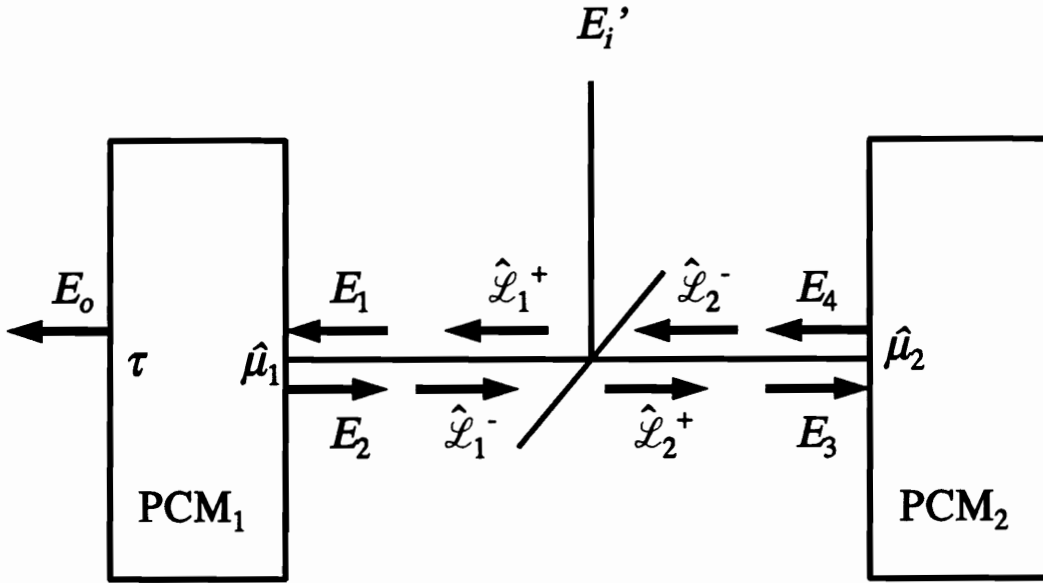


Figure 2.4: Unfolded cavity with two PCMs allowing for the independent control of the reflectivity $\hat{\mu}_1$ and $\hat{\mu}_2$ and thus for the control of the phase of the feedback parameter.

amplitude transmittance t_i . In the following, the operator \hat{S}_i^* is defined as representing the transmission through a filter with the complex conjugate transmittance t_i^* .

On substituting from equation 2.15 into equation 2.9 and using the following relationships :

$$\begin{aligned}\hat{\mathcal{F}}\hat{p}c &= \hat{p}c\hat{\mathcal{F}}^{-1} & (2.16) \\ \hat{\mathcal{F}}\hat{\mathcal{F}}f(x,y) &= \hat{\mathcal{I}}f(x,y) = f(-x,-y), \text{ (coordinate inversion operator),} \\ \hat{p}c\hat{p}c &= \hat{I}, \text{ (identity operator),} \\ \text{and } \hat{S}_i\hat{p}c &= \hat{p}c\hat{S}_i^*,\end{aligned}$$

the following steady-state output of the cavity is obtained :

$$E_o = \tau E_i + \beta \hat{\mathcal{F}}\hat{S}_1\hat{S}_2\hat{S}_2^*\hat{S}_1^*\hat{\mathcal{F}}^{-1} E_o, \quad (2.17)$$

where $\hat{\mathcal{F}}^{-1}$ is the inverse Fourier transform operator. As defined, \hat{S}_1 and \hat{S}_2 obviously commute and have a common set of eigenfunctions $\{\phi_k\}$ with complex eigenvalues $\lambda_{ik}, i = 1, 2$:

$$\hat{S}_{1(2)}\phi_k = \lambda_{1(2)k}\phi_k. \quad (2.18)$$

Assuming that the $\{\phi_k\}$ are orthogonal and form a complete set, the fields E_i and E_o can be expanded as

$$E_{i(o)} = \sum_k e_{i(o)k}\phi_k. \quad (2.19)$$

On substituting from equation 2.19 into equation 2.17, and comparing the coefficients of ϕ_k , the following relationship between the input and output coefficients is obtained :

$$e_{ok} = \frac{1}{1 - \beta|\lambda_{1k}|^2|\lambda_{2k}|^2} \tau e_{ik}. \quad (2.20)$$

Clearly, only the magnitude square of the eigenvalues of the filter operators \hat{S}_1 and \hat{S}_2 enter this transfer relationship. If they were phase-only filters (there eigenvalue is unit amplitude and they can be represented by the functional form of $e^{i\theta}$), their effects would be perfectly canceled after each round-trip pair. Therefore iterative

algorithms which call for a phase filter in the feedback loop cannot be implemented with a cavity having a PCM.

It is interesting to contrast this result with some general conditions that the operators must satisfy to allow an expansion of the input and the output in series of their eigenfunctions, something which so far is assumed valid without justification.

Indeed, for the operator analysis to be valid, the eigenfunctions of the operators must be orthogonal and form a complete set. Furthermore, to be able to process more or less arbitrary inputs, the mode structure of the cavity must be rich enough to represent arbitrary spatially band-limited field amplitude distributions. In a conventional cavity, this means that the eigenvalues of the system are all positive and non-zero (section 1.2.2). The PCM cavity, with its phase cancellation property will automatically produce closed-loop PSF which are real. It therefore seems that, to the extent that the transverse eigenmodes of the PCM cavity are degenerate, there is no restriction to the class of signals that can be processed. More realistically, the cavity can accommodate a broad class of suitably band-limited functions. Since the closed-loop operator is self-adjoint Hilbert Schmidt, the solution of equation 2.9 has the general form [31]

$$E_o = \tau E_i + \sum_n \frac{\tau \lambda_n \langle E_i, \phi_n \rangle}{(\beta^{-1} - \lambda_k)} \phi_n, \quad (2.21)$$

where $\langle \cdot, \cdot \rangle$ indicates an inner product and it is assumed that β^{-1} is not one of the eigenvalues of the operator $\hat{\mathcal{O}}$.

2.4 Conclusion

An operator theory to describe a cavity with a PCM is developed. Some of the characteristics and limitations of the cavity are discussed. They include the need for a double-path geometry in the cavity when it is used in image processing, the feedback parameter of the cavity does not depend on cavity length but on the phase of the PCM, and only operations with real eigenvalues can be accommodated by the cavity.

Chapter 3

Application of a cavity with a PCM in image processing : Theoretical study and simulation

3.1 Introduction

In this chapter, some applications of a cavity with a PCM in image processing are discussed theoretically. These examples serve as a demonstration of the wide spectrum of use of a PCM cavity in the area of image processing.

Using the operator theory developed in chapter two, it is demonstrated that a PCM cavity can be used in many areas of image processing. These include contrast control, inverse filtering, and image restoration. A possible optical setup to realize each application and the simulated results are included. The actual implementation of an image restoration algorithm and the experimental results are presented in chapter six.

3.2 Contrast control of an image

The contrast of an image recorded on film or captured by an optical system and read by a spatial-light modulator (SLM) should sometimes be altered in order to extract useful information. For example, the contrast of an X-ray photograph often needs to be enhanced, whereas the contrast of an aerial picture often needs to be reduced. An optical feedback cavity with a PCM can be used to accomplish this task. It will be shown in this section that such a cavity will transmit light according to the input intensity at each pixel and thereby achieving a contrast control.

Figure 3.1 shows a PCM cavity which can be used to control the contrast of an image. The input mirror M is placed at the front focal plane of the lens L_2 . The transparency or SLM which contains the image is inserted at the back focal plane of the lens L_2 , and its amplitude transmittance is represented by $f(x, y)$. The image transparency and the PCM entrance plane are placed in the front and back focal plane of L_3 . In a coherent system, this configuration optically implements a Fourier transformation $\hat{\mathcal{F}}$ of the image $f(x, y)$ on the PCM plane (back focal plane of lens L_3) [39]. The optical setup between the mirror plane and the PCM plane form a so-called 4- f (4 focal length) system, in which an inverted image of the mirror plane is formed on the PCM plane. The system is illuminated with a unit amplitude plane wave E_{in} . The transmitted beam at the back of the PCM is re-imaged on the output plane. This setup is similar to the one proposed by Jablonowski and Lee [6] except that the end mirror is replaced by a PCM.

The transmittance of the front mirror and of the PCM are t' and τ respectively. The forward and backward operator to be used in the analysis developed in the previous chapter are defined as :

$$\begin{aligned}\hat{\mathcal{L}}_1^{+(-)} &= e^{ikl_1} \hat{\mathcal{F}} f(x, y) \hat{\mathcal{F}} \\ \hat{\mathcal{L}}_2^{+(-)} &= e^{ikl_2} \hat{\mathcal{F}} \hat{\mathcal{F}},\end{aligned}\tag{3.1}$$

where l_i is the optical path length along path i . On substituting from equation 3.1

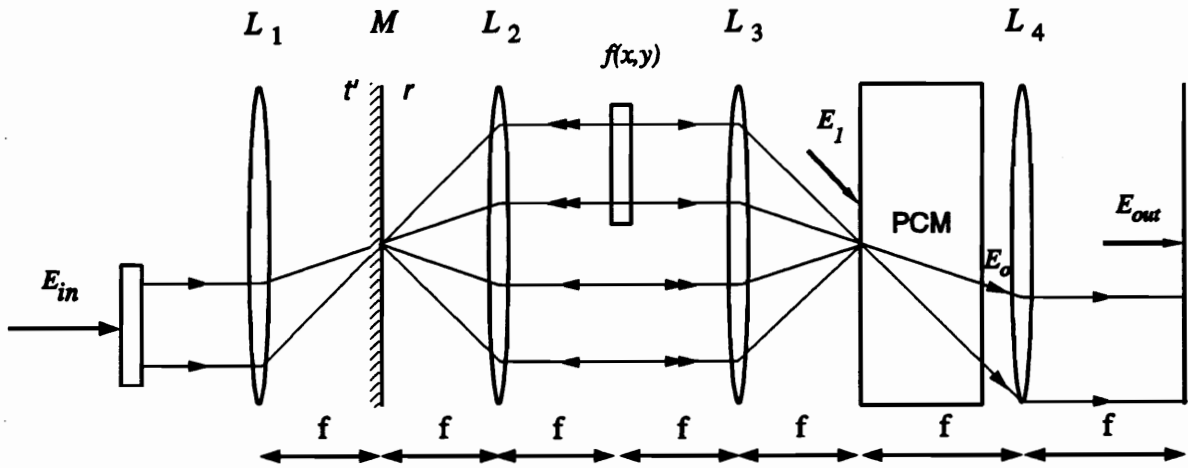


Figure 3.1: Diagram of a setup for the optical implementation of contrast enhancement. E_{in} is a plane wave of unit amplitude. The object $f(x,y)$ is placed inside the cavity. The output of the cavity is extracted behind the PCM.

into equation 2.9, the steady-state output of the cavity is found to be :

$$E_o = \tau E_i + \beta \hat{\mathcal{F}} |f(x, y)|^2 \hat{\mathcal{F}}^{-1} E_o. \quad (3.2)$$

where $E_i = t' \hat{\mathcal{L}}_1^+ \hat{\mathcal{F}} E_{in}$. To obtain the field distribution E_{out} at the output plane, E_i is substituted back into equation 3.2 and both sides of the equation are Fourier transformed :

$$\hat{\mathcal{F}} E_o = \tau t' \hat{\mathcal{I}} f(x, y) \hat{\mathcal{I}} E_{in} + \beta \hat{\mathcal{I}} |f(x, y)|^2 \hat{\mathcal{F}}^{-1} E_o. \quad (3.3)$$

The operator $\hat{\mathcal{I}}$ represents the coordinate inversion operator and the following relationships hold :

$$\begin{aligned} \hat{\mathcal{I}} \hat{\mathcal{I}} &= \hat{I}, (\text{identity operator}), \\ \hat{\mathcal{I}} f(x, y) &= f(-x, -y) \hat{\mathcal{I}}, \\ \hat{\mathcal{I}} \hat{\mathcal{F}}^{-1} &= \hat{\mathcal{F}}. \end{aligned} \quad (3.4)$$

Using these relationships to transform equation 3.3, and using $E_{out} = \hat{\mathcal{F}} E_o$, the output is found to be

$$E_{out} = \frac{\tau t' f(-x, -y) e^{ikl_1}}{1 - \beta |f(-x, -y)|^2}, \quad (3.5)$$

where $E_{in} = 1$ is used since a plane wave illumination is assumed. The phase term e^{ikl_1} appears only in the numerator and will not affect the output when the intensity $I_{out} = |E_{out}|^2$ is recorded, hence it can be dropped from equation 3.5.

The relation between the output I_{out} and the intensity transmittance $I_{in} = |f(-x, -y)|^2$ of the input is non-linear. A calculation of the output intensity versus input intensity for positive ($\beta = 1$), negative ($\beta = -1$), and no feedback ($\beta = 0$) situation is shown in figure 3.2 using $\tau = 0.55$ and $t' = 0.32$. The solid line represents the intensity transmittance of the input without feedback. The two dotted curves represent the two extreme cases when the phase of the feedback is $\psi = 0$ (positive feedback) or π (negative feedback). It is seen that when $\psi = 0(\pi)$, the contrast increases (decreases).

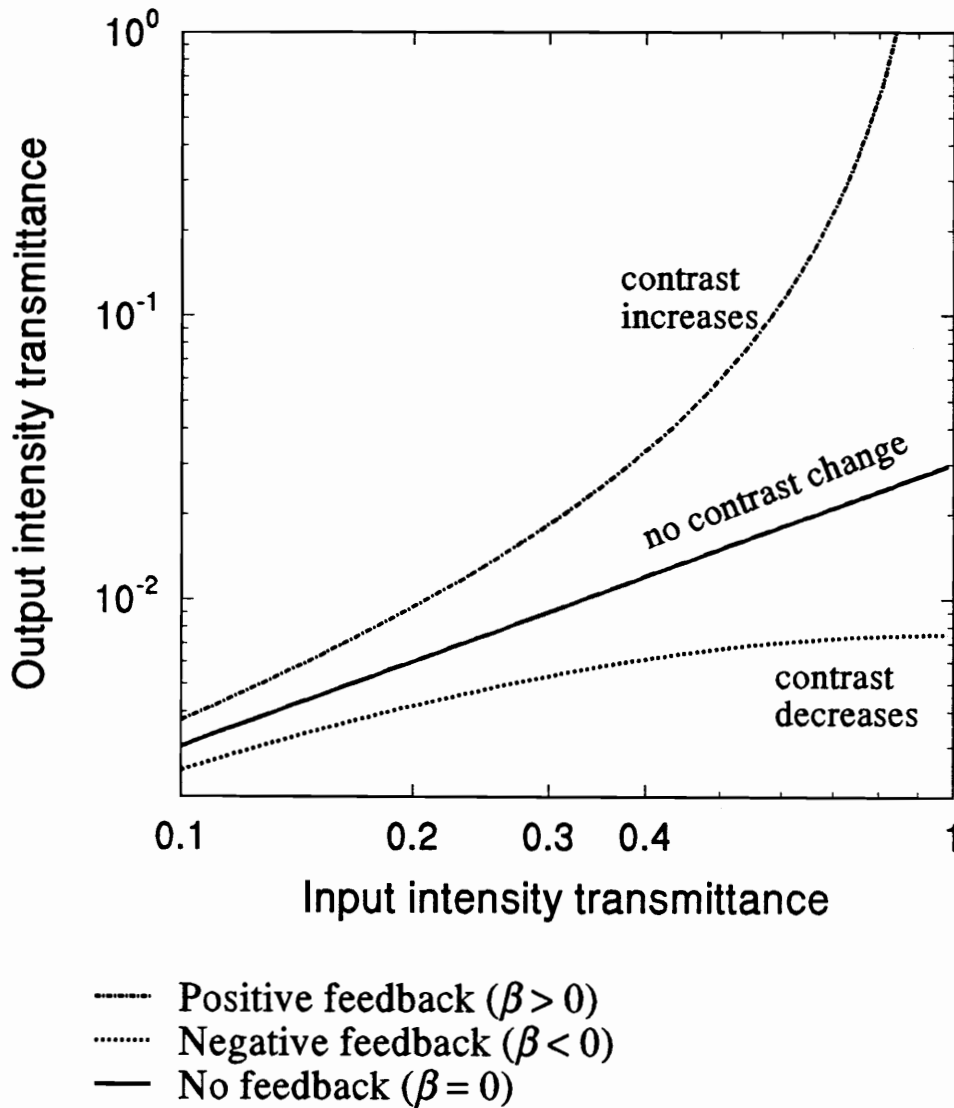


Figure 3.2: The theoretical calculation of the contrast control using feedback. The amplitude transmittance τ is 0.55 for the PCM and t' is 0.32 for the mirror. The solid line represents the intensity transmittance of an input without feedback (reference) ($\beta = 0$). The dotted lines represent the two extreme cases when the feedback of the cavity is positive ($\beta = 1$) or negative ($\beta = -1$).

3.3 Image Restoration

The second application of a PCM cavity is on image restoration. Prior to the discussion of the implementation of image restoration algorithms, the relationship between the observed, distorted image $g(x, y)$ and the original image $f(x, y)$ needs to be defined. In general, the original function $f(x, y)$ is transmitted through a distorting channel, and is being recorded as $g(x, y)$. Many kinds of distortions or degradations can be described by a Fredholm integral equation of the first kind [50, 51],

$$\int_D h(x, y; x', y') f(x', y') dx' dy' = g(x, y), \quad (3.6)$$

where $h(x, y; x', y')$, defined in the domain D , is a known kernel which relates $f(x, y)$ to $g(x, y)$. A partial list of physical and mathematical problems modeled after equation 3.6 (for example, antenna de-smoothing in radio astronomy, reconstruction of pictures from their projections in medical diagnostics, deconvolution in spectroscopy, etc) is given in reference [50].

When the domain D spans the linear space L_2 , the Fredholm integral equation 3.6 for a space-invariant imaging system takes on the form of a two-dimensional convolution of the object image with the point-spread function :

$$\iint_{-\infty}^{\infty} h(x - x', y - y') f(x', y') dx' dy' = g(x, y). \quad (3.7)$$

If the Fourier transforms of the functions $f(x, y)$, $g(x, y)$ and $h(x - x', y - y')$ are represented by their respective spatial spectra $F(\xi, \eta)$, $G(\xi, \eta)$, and $H(\xi, \eta)$, where (ξ, η) are coordinates in the spatial frequency domain B , then by invoking the convolution theorem, the spectra $F(\xi, \eta)$ and $G(\xi, \eta)$ are simply related by

$$H(\xi, \eta) F(\xi, \eta) = G(\xi, \eta). \quad (3.8)$$

At this point, the method of recovery depends on the nature of $H(\xi, \eta)$. If $H(\xi, \eta)$ does not have zeros in the linear subspace L_2 , then restoration is achieved simply by multiplying the distorted spectrum $G(\xi, \eta)$ by the inverse of $H(\xi, \eta)$

$$F(\xi, \eta) = \frac{1}{H(\xi, \eta)} G(\xi, \eta), \quad (\xi, \eta) \in B. \quad (3.9)$$

It is seen that the spectrum of the object and of the distorted image, are related by the multiplication inverse of the kernel's spectrum. The technique of restoring a distorted image using equation 3.9 is called inverse filtering.

If the spectrum $H(\xi, \eta)$ has zeros over $(\xi, \eta) \in B$, direct inversion cannot be used, therefore iterative methods are needed to recover $f(x, y)$.

3.3.1 Inverse filtering

To implement the restoration scheme of equation 3.9, two kinds of operations are required. They are Fourier transformation and ordinary multiplication. Through the use of a coherent light source, a lens, and a photographic transparency mask, these two operations are easily performed by coherent optical means. Inverse filtering has been demonstrated using a spatial filtering technique and a conventional feedback cavity [6, 32]. The recovery of a distorted image through the use of a spatial filter alone is strongly limited by the dynamic range available with photographic film or spatial light modulators which are used to store the spatial mask. In general, a feedback cavity provides a larger dynamic range than spatial filtering alone. Therefore, a feedback cavity is preferred in implementing the inverse filtering.

To implement the inverse filtering in a cavity with a PCM, only one filter $S(\xi, \eta)$ is needed in the primary path. The secondary path does not need a filter. The geometry of this implementation is shown in figure 3.3.

In calculating the transfer function of the cavity, it is more convenient to work in the spatial frequency domain than to define the fields at the front surface of the PCM as was done in chapter two. The cavity field E_1 is defined immediately behind the spatial filter S , and E'_i immediately behind H as shown in figure 3.3. In steady-state, the cavity field E_1 is given by :

$$E_1 = E_i + S\hat{\mathcal{F}}_r\hat{\mathcal{F}}\hat{\mathcal{F}}\hat{\mu}_2\hat{\mathcal{F}}\hat{\mathcal{F}}_r\hat{\mathcal{F}}S\hat{\mathcal{F}}\hat{\mu}_1\hat{\mathcal{F}}E_1. \quad (3.10)$$

Using the relationships in equation 2.16 and defining the feedback parameter as $\beta =$

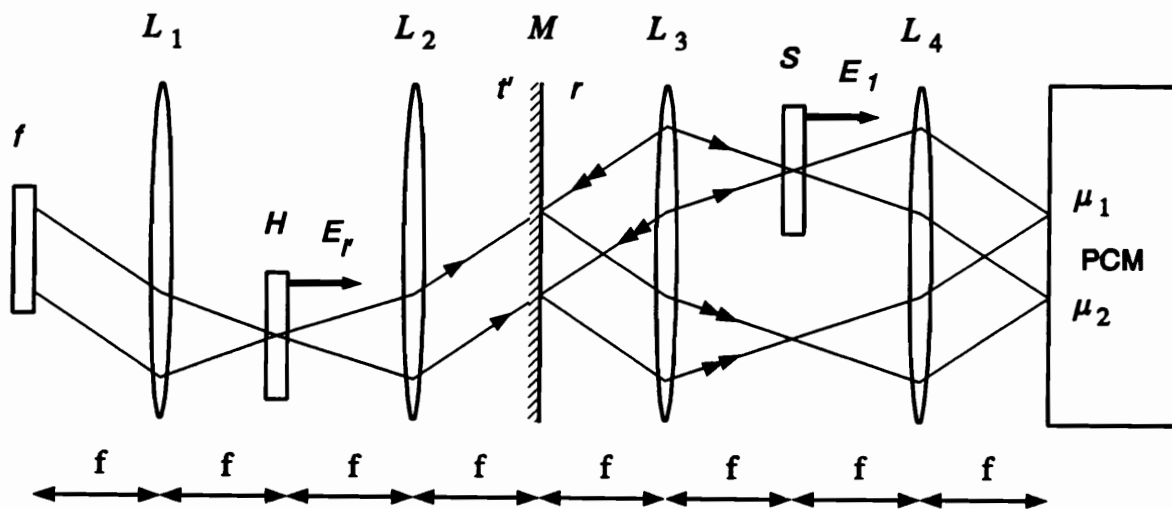


Figure 3.3: Diagram of a setup for the implementation of inverse filtering. H represents the degradation filter, and S represents the restoration filter.

$|r|^2 r_{pcm1}^* r_{pcm2}$ as before, a simple form of the cavity field E_1 is obtained :

$$E_1 = E_i + \beta |S|^2 E_1, \quad (3.11)$$

where E_i is related to E'_i by $E_i = t' S \hat{\mathcal{F}} \hat{\mathcal{F}} E'_i$. The transfer function T of the cavity is thus given by :

$$T = \frac{E_1}{E'_i} = \frac{t' S \hat{\mathcal{I}}}{1 - \beta |S|^2}, \quad (3.12)$$

where $\hat{\mathcal{I}}$ is the coordinate inversion operator.

To proceed with the calculation of the filter S , note that the condition for a complete restoration is that the product of the transfer function of the cavity and the degradation filter is equal to a constant c ,

$$TH = c. \quad (3.13)$$

Thus S must satisfy

$$\frac{t' S \tilde{H}}{1 - \beta |S|^2} = c \quad (3.14)$$

where \tilde{H} represents the coordinate inverted H . For negative feedback, set $\beta = -1$; the equation becomes

$$\begin{aligned} \frac{S \tilde{H}}{1 + |S|^2} &= \frac{c}{t'} \\ S \tilde{H} &= \frac{c}{t'} (1 + |S|^2). \end{aligned} \quad (3.15)$$

If H is real, then S has to be real to satisfy the above equation. Therefore, the spatial filter S can be calculated simply as :

$$S = \frac{t' \tilde{H}}{2c} \pm \sqrt{\left(\frac{t' \tilde{H}}{2c}\right)^2 - 1}. \quad (3.16)$$

Since \tilde{H} is an amplitude-only filter, thus S is also an amplitude-only filter. The restoration is, therefore, not subject to the limitation due to phase cancellation discussed in chapter two (section 2.3.3) and it can be realized in a PCM cavity.

3.3.2 Extrapolation of a band-limited function

If the distortion is due to a low-pass or a band-pass system where $H(\xi, \eta) = 0$, $(\xi, \eta) \in B$, the recovery of $f(x, y)$ is much more complicated. In the following analysis, only one class of such a recovery problem will be considered, in which its elements are either objects having a limited spatial extent or objects having a limited spatial frequency spread. Although the terminologies are different, these two elements are basically the same. For instance, a function with a limited frequency spread has an infinite spatial extent, while a function with a limited spatial extent has spatial frequencies extending to infinity.

The theoretical foundation establishing that a resolution beyond the low-pass limit is possible, rests on two mathematical theorems [39]. They are :

Theorem 1 *The two-dimensional Fourier transform of a spatially bounded function is an analytic function in the spatial frequency domain.*

Theorem 2 *If any analytic function in the spatial frequency plane is known exactly in a small (but finite) region of that plane, then the entire function can be found (uniquely) by means of analytic continuation.*

The concept of analytic continuation of a function is most easily understood by using an example invoking the sampling theorem in one-dimension. Let the function $f(x)$ be space limited with a spatial extent $[-K, K]$. Then, by the sampling theorem, the object spectrum $F(\xi)$ can be represented exactly by an infinite set of discrete samples at n/K , where n is an integer,

$$F(\xi) = \sum_{n=-\infty}^{\infty} F\left(\frac{n}{K}\right) \text{sinc}\left[K\left(\xi - \frac{n}{K}\right)\right], \quad (3.17)$$

where the $\text{sinc}(x) = \sin(x)/x$. This equation means that the spectrum of F at a spatial frequency $\xi \neq n/K$ is represented by the sum of all the contributions from every sampling point. The smoothing function is a sinc function being offset to each of the sampling locations, and the weighting factor is the value of the spectrum at

each sampling point. A low-pass filter transmits only a finite range of frequencies, say up to $n = \pm N$. If this finite set of samples is used to reconstruct the image, some resolution will be lost. But if the spectral information between the sampling points is also known, it can be used to determine the sample values outside the pass-band (extrapolation). This is because data at $\xi \neq n/K$ contains information from all the samples outside the pass-band since the sinc functions attached to these samples extend into the pass-band. Therefore the spatial frequency $F(\xi)$ contains non-zero contribution from the sampling points outside the pass-band.

Several iterative algorithms have been proposed to extrapolate the spectrum of a function with known limited extent. They have been shown to offer convergence, at least in a noise-free environment. Many of them are based on amplitude-only filtering. They are thus not affected by the limitations discussed in chapter two, and should be realizable with a PCM cavity. One such algorithm, namely the Gerchberg algorithm, is briefly reviewed in the next section to provide a means of comparison with the operation of the PCM cavity used in the experiment described in chapter six.

3.3.3 Gerchberg Algorithm

The aim of the Gerchberg algorithm is to iteratively recover a function $f(x, y)$ defined in the spatial domain D from bandlimited data $g(x, y)$, which means that its spatial spectrum $G(\xi, \eta)$ vanishes outside the spatial frequency domain B .

The spatial and spatial frequency truncation operators \hat{T}_D and \hat{T}_B are defined as

$$\begin{aligned} \hat{T}_D f(x, y) &= \begin{cases} f(x, y) & , \forall (x, y) \in D \\ 0 & , \text{otherwise} \end{cases} \\ \hat{T}_B F(\xi, \eta) &= \begin{cases} F(\xi, \eta) = \hat{\mathcal{F}} f(x, y) & , \forall (\xi, \eta) \in B \\ 0 & , \text{otherwise.} \end{cases} \end{aligned} \quad (3.18)$$

In this expression, the Fourier transform $\hat{\mathcal{F}}$ of a complex function f is defined by

$$\hat{\mathcal{F}} f(x, y) = \iint_{-\infty}^{\infty} f(x, y) e^{-i2\pi(\xi x + \eta y)} dx dy. \quad (3.19)$$

Similarly, the inverse Fourier transform $\hat{\mathcal{F}}^{-1}$ of a function $F(\xi, \eta)$ is defined by

$$\hat{\mathcal{F}}^{-1}F(\xi, \eta) = \iint_{-\infty}^{\infty} F(\xi, \eta)e^{i2\pi(\xi x + \eta y)}d\xi d\eta. \quad (3.20)$$

The m th estimate of $f(x, y)$ is obtained by adding a part of the spectrum that extends beyond the domain B to the $(m - 1)$ th estimate, according to the recursive relation

$$g^{(m)}(x, y) = \hat{T}_D\{g(x, y) + \hat{\mathcal{F}}^{-1}[\hat{I} - \hat{T}_B]\hat{\mathcal{F}}\hat{T}_Dg^{(m-1)}(x, y)\}. \quad (3.21)$$

In this expression, $[\hat{I} - \hat{T}_B]$ is a complementary operator defined as

$$[\hat{I} - \hat{T}_B]G(\xi, \eta) = \begin{cases} 0 & , \forall(\xi, \eta) \in B \\ G(\xi, \eta) & , \forall(\xi, \eta) \notin B, \end{cases} \quad (3.22)$$

and the first estimate is

$$g^{(1)}(x, y) = \hat{T}_Dg(x, y) = \hat{T}_D\hat{\mathcal{F}}^{-1}\hat{T}_B\hat{\mathcal{F}}f(x, y). \quad (3.23)$$

Figure 3.4 is a pictorial description of the algorithm.

A comparison of equation 3.21 with equation 2.8 shows that this algorithm can be implemented with a PCM cavity having a round-trip operator

$$\begin{aligned} \hat{\mathcal{O}} &= \hat{T}_D\hat{\mathcal{F}}^{-1}[\hat{I} - \hat{T}_B]\hat{\mathcal{F}}\hat{T}_D \\ &= [\hat{I} - \hat{\mathcal{G}}]\hat{T}_D, \end{aligned} \quad (3.24)$$

where $\hat{\mathcal{G}} = \hat{T}_D\hat{\mathcal{F}}^{-1}\hat{T}_B\hat{\mathcal{F}}$.

The eigenfunctions $\{\phi_k\}$ of the operator $\hat{\mathcal{G}}$ are assumed to be complete in the space of functions with a limited domain D , with $\hat{\mathcal{G}}\phi_k = \lambda_k\phi_k$, and one can then substitute the expansions

$$\hat{T}_Dg^{(m)} = \sum_k e_k^{(m)}\phi_k \quad (3.25)$$

into equation 3.21 and obtain the recurrence formula for the expansion coefficients of the m th Gerchberg estimate [52] :

$$e_k^{(m)} = \frac{1 - (1 - \lambda_k)^m}{\lambda_k} e_k^{(1)}. \quad (3.26)$$

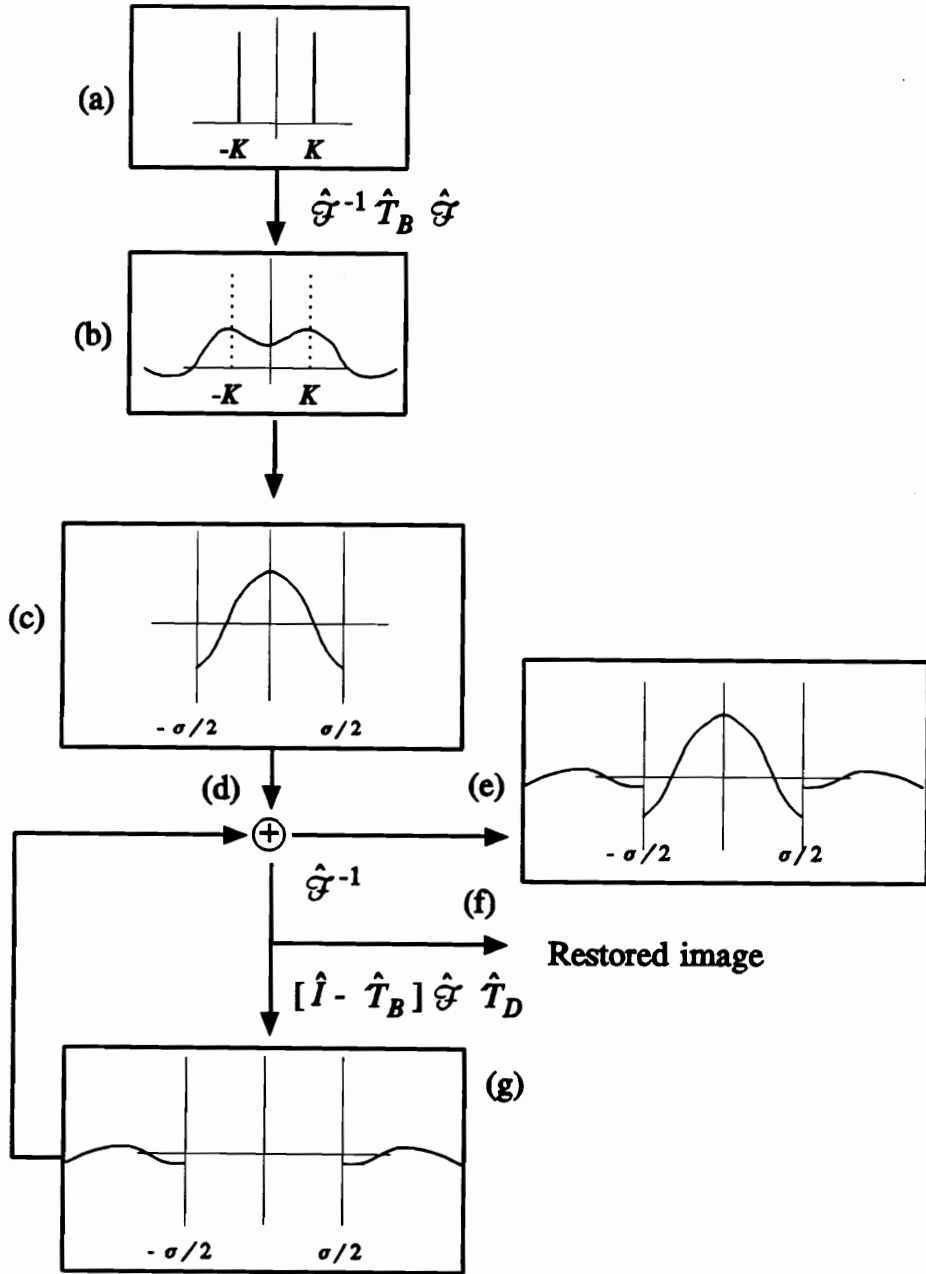


Figure 3.4: Pictorial description of the Gerchberg algorithm. (a) input object, (b) distorted object (after low-pass filter), (c) frequency distribution of the low-pass object, (d) coherent addition, (e) output of the coherent addition at the spatial frequency domain, (f) restored object after m th iterations, (g) part of the feedback operation which includes the truncation in the space domain and the high-pass operation in the spatial frequency domain.

Before carrying on the discussion, two short remarks are in order.

The first is that in an optical implementation of the algorithm described by equation 3.21, it will not be possible to terminate the process after a prescribed number of iterations. In that sense, the feedback algorithm implemented in a cavity with a PCM is not, strictly speaking, iterative. When the number of iterations is large,

$$e_k^{(m)}(m \rightarrow \infty) \rightarrow \frac{1}{\lambda_k} e_k^{(1)}, \quad (3.27)$$

indicating that the final estimate is similar to the output of an inverse filter.

The second remark concerns the expansions in series of eigenfunctions. A special case, corresponding to a simple rectangle function for the truncation operators, has been extensively studied. In this case, the eigenfunctions $\{\phi_k\}$ are the prolate spheroidal wave functions [53] which satisfy :

$$\int_{-K}^K \frac{\sin \sigma(x-x')}{\pi(x-x')} \phi_k(x') dx' = \lambda_k \phi_k(x), \quad (3.28)$$

where λ_k is real, ≤ 1 , and $\lambda_k \rightarrow 0$ as $k \rightarrow \infty$. The integral, with its limits $[-K, K]$, is exactly represented by the operator $\hat{\mathcal{G}} = \hat{T}_D \hat{\mathcal{F}}^{-1} \hat{T}_B \hat{\mathcal{F}}$ used before. A summary of the properties of the spheroidal wavefunctions and their applications to optics can be found in [53, 54]. Of particular importance to image restoration are the orthogonality and the completeness of the set [54],

$$\begin{aligned} \text{(orthogonality)} \quad \int_{-K}^K \phi_i(x) \phi_j(x) dx &= \begin{cases} \lambda_i & , i = j \\ 0 & , i \neq j \end{cases} \\ \text{(completeness)} \quad \sum_{k=0}^{\infty} \lambda_k^{-1} \phi_k(x) \phi_k(x') &= \delta(x-x'), \text{ for } x, x' \in D, \end{aligned} \quad (3.29)$$

where $\delta(x-x')$ is the Dirac delta function. These relationships justify the expansion in equation 3.25.

However, even in this simple case, the eigenfunctions are very tedious to calculate. The main advantage in trying to implement these algorithms optically is that the eigenfunctions need not be calculated or even known. With the appropriate operators in the cavity, the eigenfunctions will automatically be the cavity eigenmodes.

3.3.4 Simulation of the Gerchberg algorithm

A computer program was written to simulate the extrapolation of the spectrum of a distorted image based on the Gerchberg algorithm. A two-point object f is used as the original function. The object is assigned to a complex array $f[x]$ of 128 elements, only the sixty-first and the sixty-seventh elements are non-zero, and $f[61] = f[67] = 1$. The spectrum $F[\xi]$ of the object is therefore represented by a cosine function. The low-pass operation is performed by a truncation in the spatial frequency domain B . The object is Fourier transformed to and from the spatial frequency domain using a variant of the Cooley-Tukey complex forward (backward) fast Fourier transformation algorithm (FFT) [55]. A low-pass operation [56] is performed in the spectrum $F[\xi]$ with the nineteenth element to the one-hundred-and-tenth element set to zero.

The low-pass spectrum G is fed into the iteration loop according to equation 3.30 :

$$G^{(m)} = G + [\hat{I} - \hat{T}_B] \hat{\mathcal{F}} \hat{T}_D \hat{\mathcal{F}}^{-1} G^{(m-1)} \quad (3.30)$$

The m th iteration result of the restoration is shown along with the original object in figure 3.5. For the first 10 iterations, the rate of convergence is high and it then slow down and it continuous to slow down as the original spectrum is being approached. In fact, it is predicted that the estimated spectrum approaches the original spectrum only after an infinite number of iterations [10]. The power spectrum of the extrapolated function is shown along with the original spectrum in figure 3.6.

The sum of the absolute spectrum error is calculated according to the following equation and shown in figure 3.7

$$\text{error sum} = \sum_{k=1}^{128} |F[k] - G^{(m)}[k]|. \quad (3.31)$$

In a noise free environment, it can be shown that the sum of the absolute error approaches zero after a very large number of iterations [57].

It is interesting to ask whether the Gerchberg algorithm could be used to restore more complex objects. Santis *et al* [10] have shown that the iterative algorithm is less effective on an object with a larger space-bandwidth product (more complex). In an

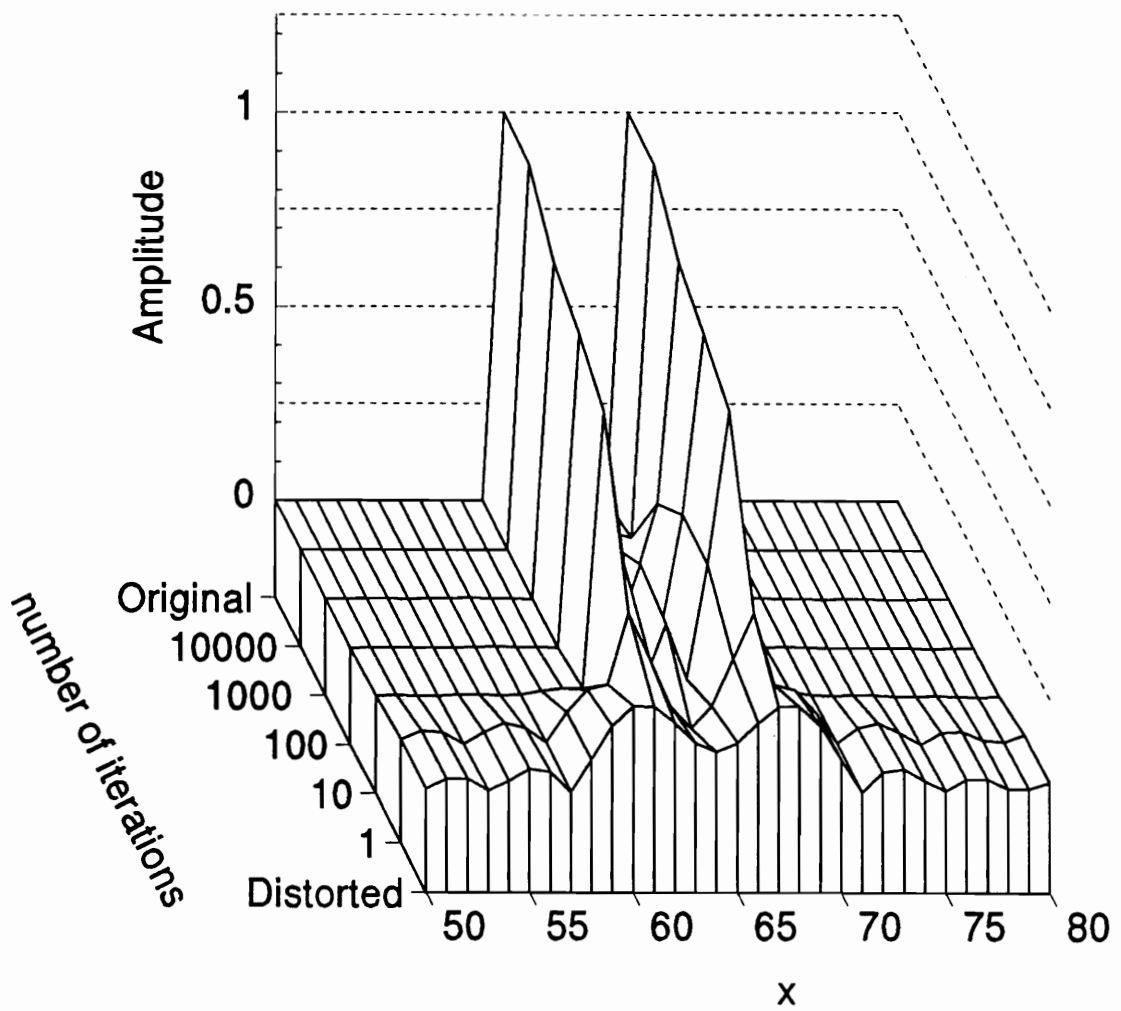


Figure 3.5: A comparison of the two-point object with the restored objects after various numbers of iterations.

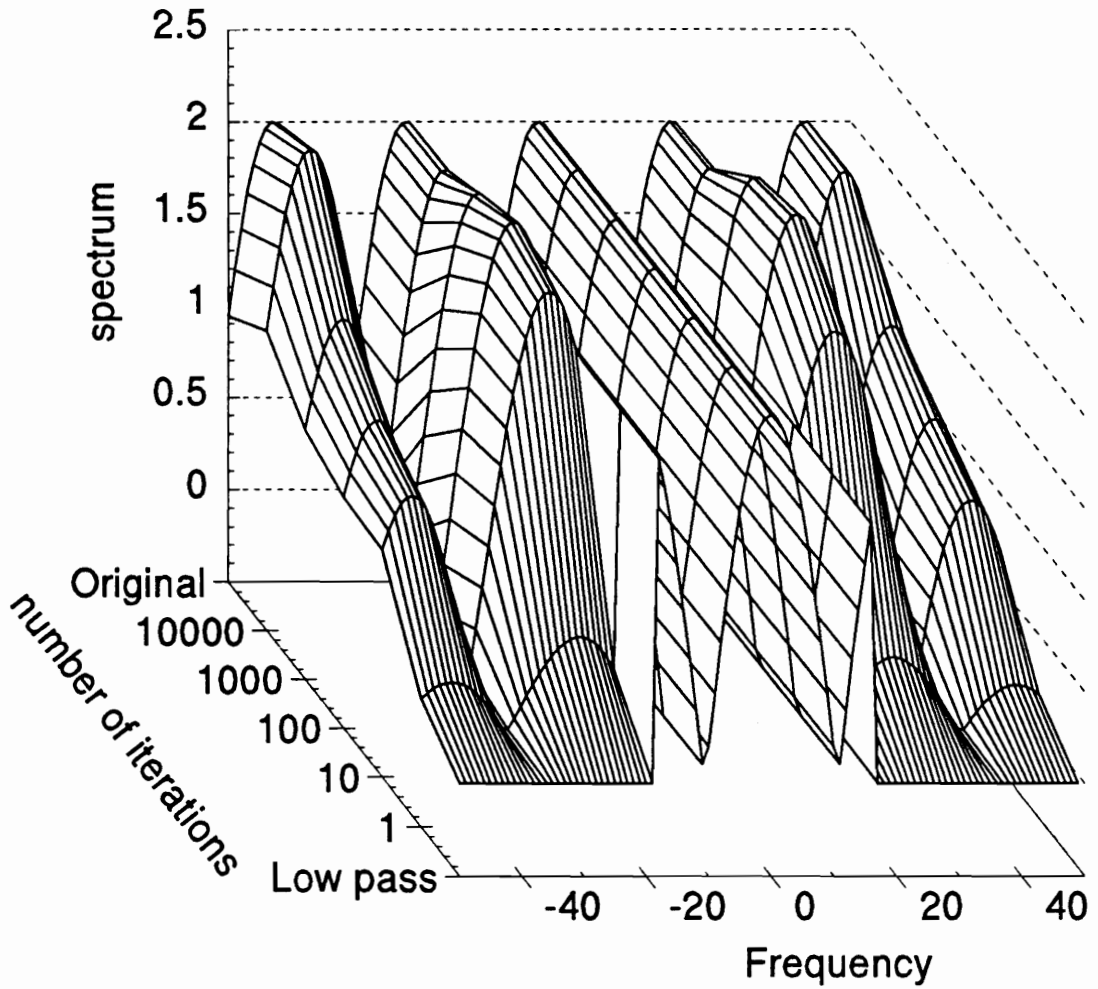


Figure 3.6: A comparison of the power spectrum distribution of the original two-point object and that of the restored objects after various numbers of iterations.

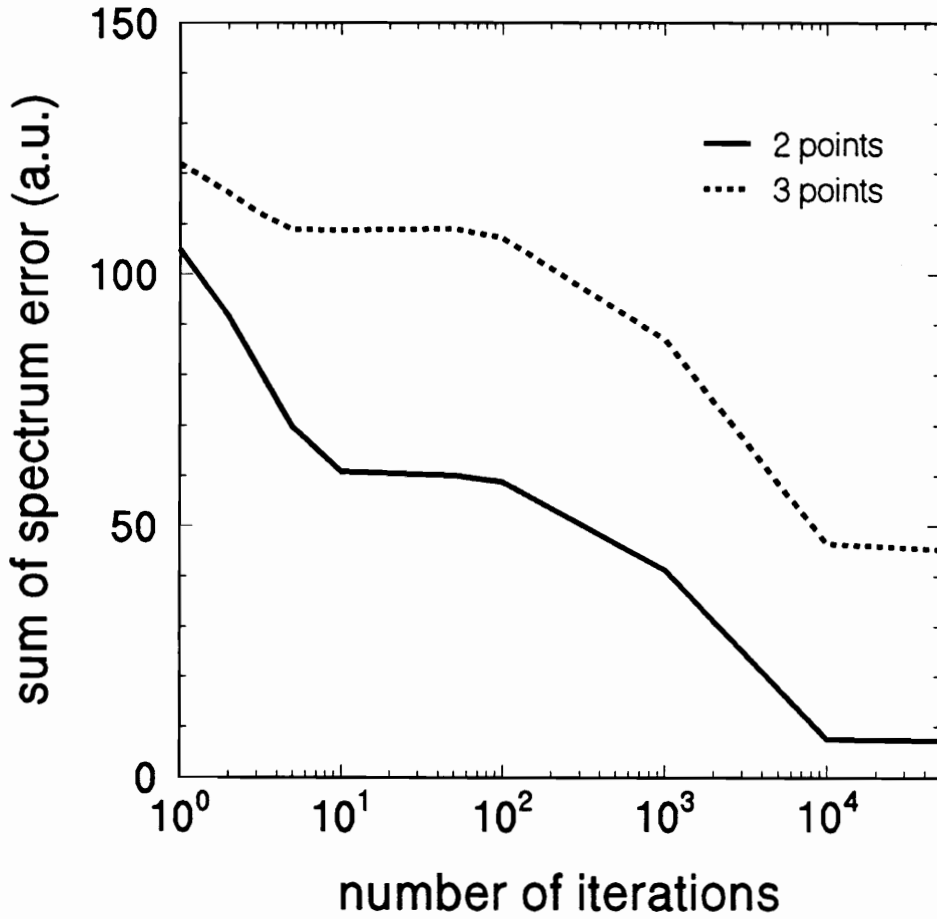


Figure 3.7: A plot of the sum of absolute spectral error against the number of iterations using the Gerchberg algorithm. The curves for a two-point object and a three-point object are shown together for comparison.

attempt to verify this, an extra point inside the two-point object was added to make it a three-point object, $f[61] = f[64] = f[67] = 1$. The rest of the array elements were set to zero. The spectrum of this object is a cosine function with amplitude of two units added to a dc term of amplitude equals to one. The same low-pass window was used as before, the result is shown in figure 3.8 and figure 3.9. The sum of the absolute spectrum error is plotted against number of iterations in figure 3.7. It is seen that the sum of the absolute error drops monotonically but at a slower rate than for the two-point object. This is in accord with the predictions of Santis [10, 54].

3.3.5 Optical implementation

The optical system considered for implementing equation 3.21 is shown in figure 3.10. It is similar to the set-up of Marks *et al* [5, 58] except that a PCM is replacing his conventional mirror. The input data $g(x, y)$ is placed in the front focal plane of lens L_1 . The input mirror of the cavity, placed in the back focal plane of L_1 , has a transparent opening representing the spatial frequency truncation operator \hat{T}_B . The transmittance and reflectance operators $\hat{\mathcal{T}}$ and $\hat{\mathcal{R}}$ of that mirror are thus given by

$$\hat{\mathcal{T}} = \hat{T}_B, \quad \hat{\mathcal{R}} = r[\hat{I} - \hat{T}_B], \quad (3.32)$$

where r is the amplitude reflectance of the mirror. A slit, of width equal to the spatial extent of the object representing the spatial truncation operator \hat{T}_D , is placed at the back focal plane of L_2 . No operator is needed in the spatial domain of the secondary path. The output field equation of this cavity is found to be

$$E_1 = E_i + \beta \hat{T}_D \hat{\mathcal{F}} [\hat{I} - \hat{T}_B] \hat{\mathcal{F}} \hat{p} c \hat{\mathcal{F}} [\hat{I} - \hat{T}_B] \hat{\mathcal{F}} \hat{T}_D \hat{p} c E_1, \quad (3.33)$$

where

$$E_i = \hat{T}_D \hat{\mathcal{F}} \hat{T}_B \hat{\mathcal{F}} g(x, y), \quad (3.34)$$

and $\beta = |r|^2 r_{pcm1}^* r_{pcm2}$ as before. The other operators are as defined in chapter two.

Using the relationships of equation 2.16 together with the fact that \hat{T}_D , \hat{T}_B and $[\hat{I} - \hat{T}_B]$ are projection operators \hat{P} satisfying $\hat{P}^2 \phi = \hat{P} \phi$ and $\hat{P} \hat{p} c = \hat{p} c \hat{P}$, equation 3.33

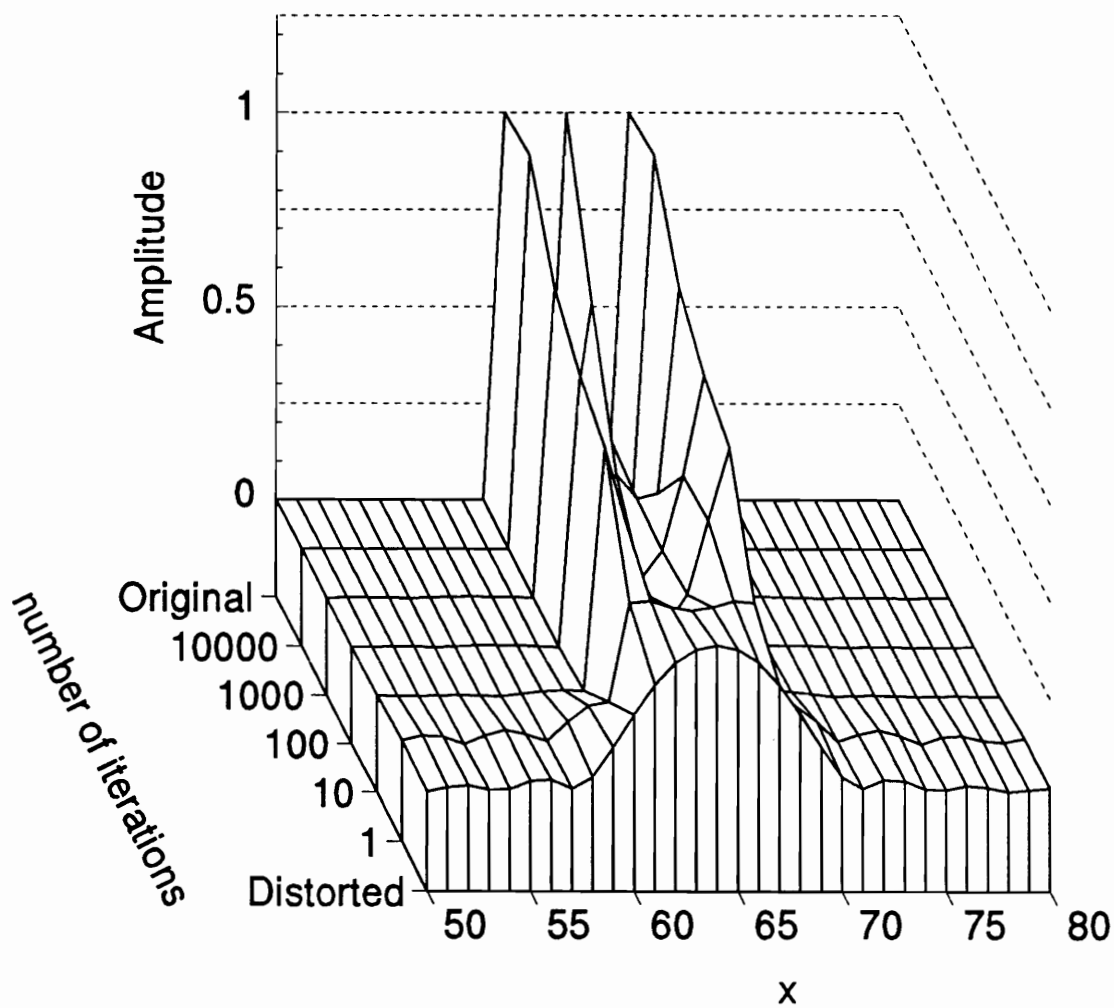


Figure 3.8: A comparison of the restoration of a three-point object after various numbers of iterations.

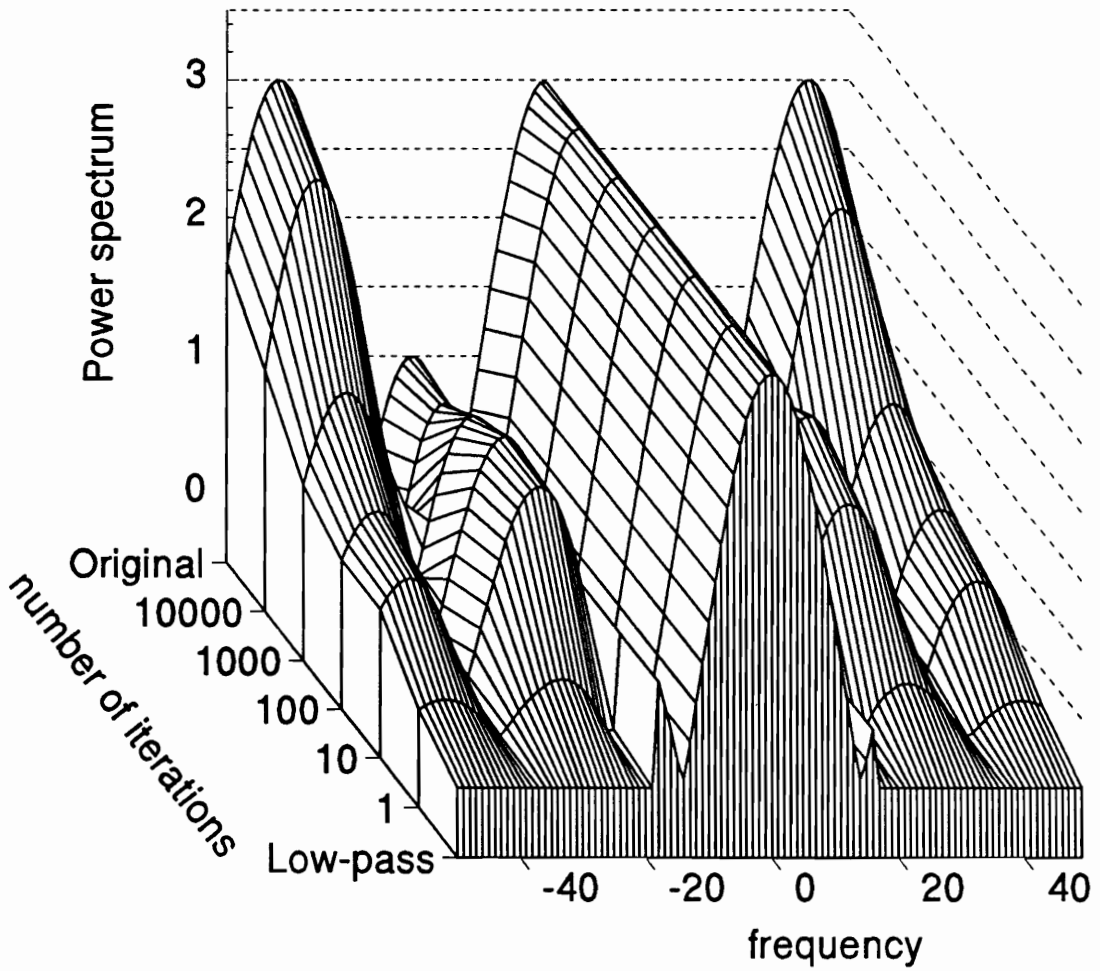


Figure 3.9: A comparison of the power spectrum of the restoration of a three-point object after various numbers of iterations.

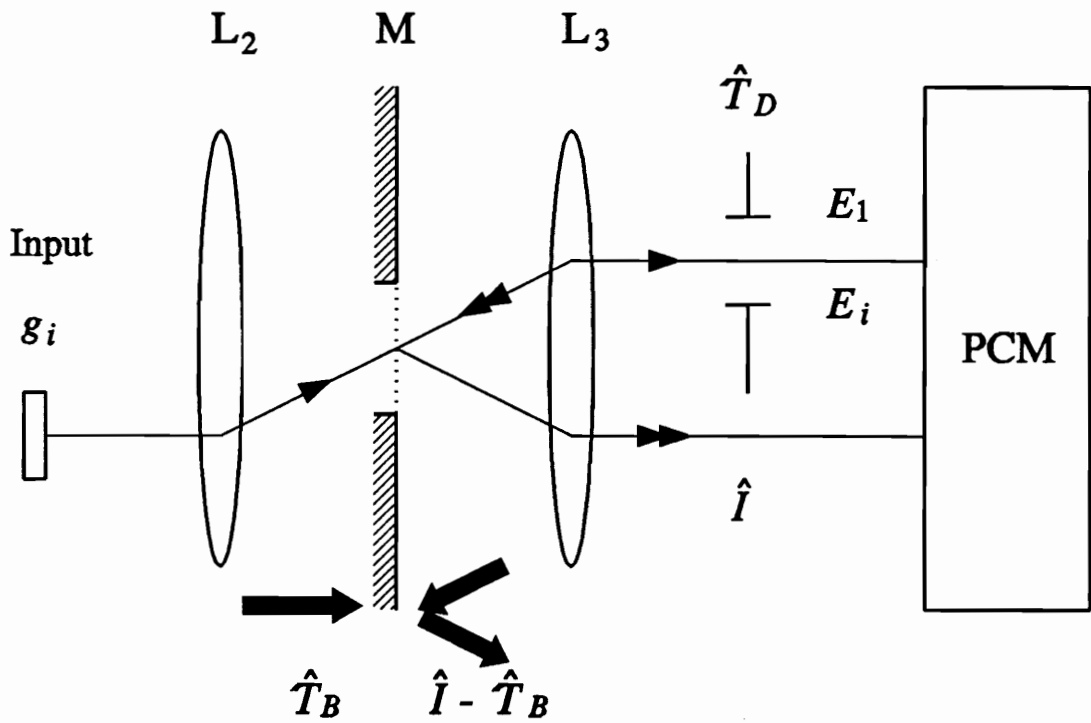


Figure 3.10: Diagram of a setup proposed for the optical implementation of the Gerchberg algorithm. The input mirror implements the complementary spatial frequency truncation operator $[\hat{I} - \hat{T}_B]$. The primary path contains a spatial truncation operator \hat{T}_D in plane P . The secondary path is empty corresponding to an identity operator \hat{I} .

takes the form

$$E_1 = E_i + \beta \hat{T}_D \hat{\mathcal{F}} [\hat{I} - \hat{T}_B] \hat{\mathcal{F}}^{-1} \hat{T}_D E_1, \quad (3.35)$$

which is equivalent to equation 3.21 if $g^{(m)} (m \rightarrow \infty) \rightarrow E_1$ and if the high-pass filter $[\hat{I} - \hat{T}_B]$ is spatially inverted. It can be shown that if \tilde{T}_B is defined as the coordinated inverted \hat{T}_B and

$$\tilde{T}_B(\xi, \eta) = \hat{T}_B(-\xi, -\eta), \quad (3.36)$$

then

$$\hat{\mathcal{F}}[\hat{I} - \hat{T}_B] \hat{\mathcal{F}}^{-1} = \hat{\mathcal{F}}^{-1}[\hat{I} - \tilde{T}_B] \hat{\mathcal{F}}. \quad (3.37)$$

It is assumed that the eigenfunctions $\{\phi_k\}$ of the truncation/low-pass operator $\hat{\mathcal{G}} = \hat{T}_D \hat{\mathcal{F}}^{-1} \tilde{T}_B \hat{\mathcal{F}}$ form a complete set

$$\hat{\mathcal{G}} \phi_k = \lambda_k \phi_k, \quad (3.38)$$

where λ_k is the eigenvalue when $\hat{\mathcal{G}}$ operates on ϕ_k . On expanding $\hat{T}_D E_1$ and $\hat{T}_D E_i$ in terms of $\{\phi_k\}$:

$$\hat{T}_D E_{1(i)} = \sum_k e_{1(i)k} \phi_k, \quad (3.39)$$

and substituting these expansions into equation 3.35, the expansion coefficients of the output are found to be

$$e_{1k} = \frac{1}{1 - \beta(1 - \lambda_k)} e_{ik}. \quad (3.40)$$

If the feedback parameter is close to unity (cavity near threshold), the output coefficients become

$$e_{1k} \simeq \frac{1}{\lambda_k} e_{ik} (\beta \rightarrow 1), \quad (3.41)$$

showing that the output of the cavity approaches that of an inverse filter.

3.4 Conclusion

In this chapter, the application of a PCM cavity to contrast control, inverse filtering, and image restoration was discussed from a theoretical point of view. The

optical implementations of these three applications was also discussed. The feasibility of image restoration using the Gerchberg algorithm was tested by a numerical simulation. A set-up for implementing this scheme optically was proposed and some of the requirements and limitations were discussed.

Chapter 4

Realization of a PCM with photorefractive BaTiO₃ : Theory and experimental investigation

4.1 Introduction

One of the key elements in a PCM cavity is the PCM itself. The ability of a PCM to “heal” phase errors and the possibility of introducing some gain into the cavity give the PCM cavity substantially different characteristics from that of a conventional cavity. For the experiments, degenerate four-wave mixing (4WM) in photorefractive BaTiO₃ was selected to achieve optical phase conjugation with gain. In this chapter, the characteristics of this PCM are tested experimentally. In particular, its abilities to produce gain and remove phase distortions are investigated.

The photorefractive effect describes a phenomenon in certain materials which exhibit change of refractive index n when light passes through them [20]. Materials that exhibit such changes are referred to as photorefractive materials. In section 4.2, the ability of photorefractive media to record a real-time index grating due to the

photorefractive effect is explained. A theory based on the band transport model is outlined to explain this effect. The dependence of the index grating on material parameters is demonstrated for BaTiO₃. Using this index grating in photorefractive material, a four-wave mixing (4WM) geometry is used to realize the PCM. In this geometry, a third beam is scattered from the real-time phase grating to produce the phase conjugate signal. The geometry and the coupling of the beams are outlined in section 4.3. In section 4.4, the optimization of the PCM using various design parameters is discussed. In sections 4.5 and 4.6 the capability of the PCM is investigated experimentally. The ability of the PCM to provide optical amplification is demonstrated, and the reflectivity of the PCM against various beam intensity ratios is measured. In section 4.6 the ability of the PCM to heal a phase distortion is observed.

4.2 Photorefractive effect

Light-induced refractive changes in nonlinear, frequency doubling crystals was, at first, called “optical damage” in the late 1960’s [59, 60, 61]. These changes can persist in the dark from picoseconds to days, depending on the materials, and can be erased by flooding the medium with light. Light-induced phase gratings are produced by the interference fringes of two coherent beams in these materials. It has been proposed to use these gratings for high density holographic optical storage [62, 63, 64].

The interest in photorefractive materials was renewed in the late 1970’s because of the possibility of using the light-induced phase grating in these materials to obtain coherent optical gain and to construct PCMs. This section is used to outline the band-transport model to explain the formation of a phase grating in photorefractive materials. The understanding of the theory enables us to optimize a PCM using these materials.

4.2.1 Band-transport model

There are two physical models currently being used to explain the photorefractive effect. They are the band-transport model developed by Kukhtarev *et al* [65] and the charge-hopping model developed by Feinberg [20]. Since the charge hopping model is a special case of the band-transport model when the lifetime of the free charge carriers is short, only the band-transport model will be discussed.

In the band-transport model, it is assumed that impurities X , which can exist in two valency states, are present in the materials and their energy levels are in the band gap. These impurities provide donor and acceptor sites for the light-induced free charges. The photo-excited charge carriers can be electrons or holes (or both) depending on the material. For example, if the dominant charge carriers are electrons (holes), then the donor sites are X (X^+) and the acceptor sites are X^+ (X). For simplicity, electrons are assumed to be the dominant charge carriers in the following calculations.

In the band-transport model, it is assumed that photo-excited electrons are ejected from filled donor sites to the conduction band. The charges migrate through diffusion or drift and recombine with acceptor sites in the dark regions. This mechanism is illustrated in figure 4.1 (extracted from reference [66]). In this figure, an interference pattern is formed by two coherent beams, called the signal beam E_s and the pump beam E_1 . Let the two beams be represented by

$$E_j = \frac{1}{2} \hat{e}_j A_j e^{i(\vec{k}_j \cdot \vec{r} - \omega t)} + \text{c.c.}, \quad j = 1, s, \quad (4.1)$$

where the A_j are the slowly varying electric field amplitudes, the \hat{e}_j are the polarization vectors, and the \vec{k}_j are the wave vectors. The intensity of the interference fringes $I(\vec{x})$ is

$$I(\vec{x}) = I_o (1 + m \cos \vec{k}_g \cdot \vec{x}), \quad (4.2)$$

where $I_o = |A_1|^2 + |A_2|^2$, $\vec{k}_g = \vec{k}_s - \vec{k}_1 =$ grating wave vector. The dimensionless modulation index m is

$$m = \frac{2A_1^* A_s}{I_o} (\hat{e}_s \cdot \hat{e}_1). \quad (4.3)$$

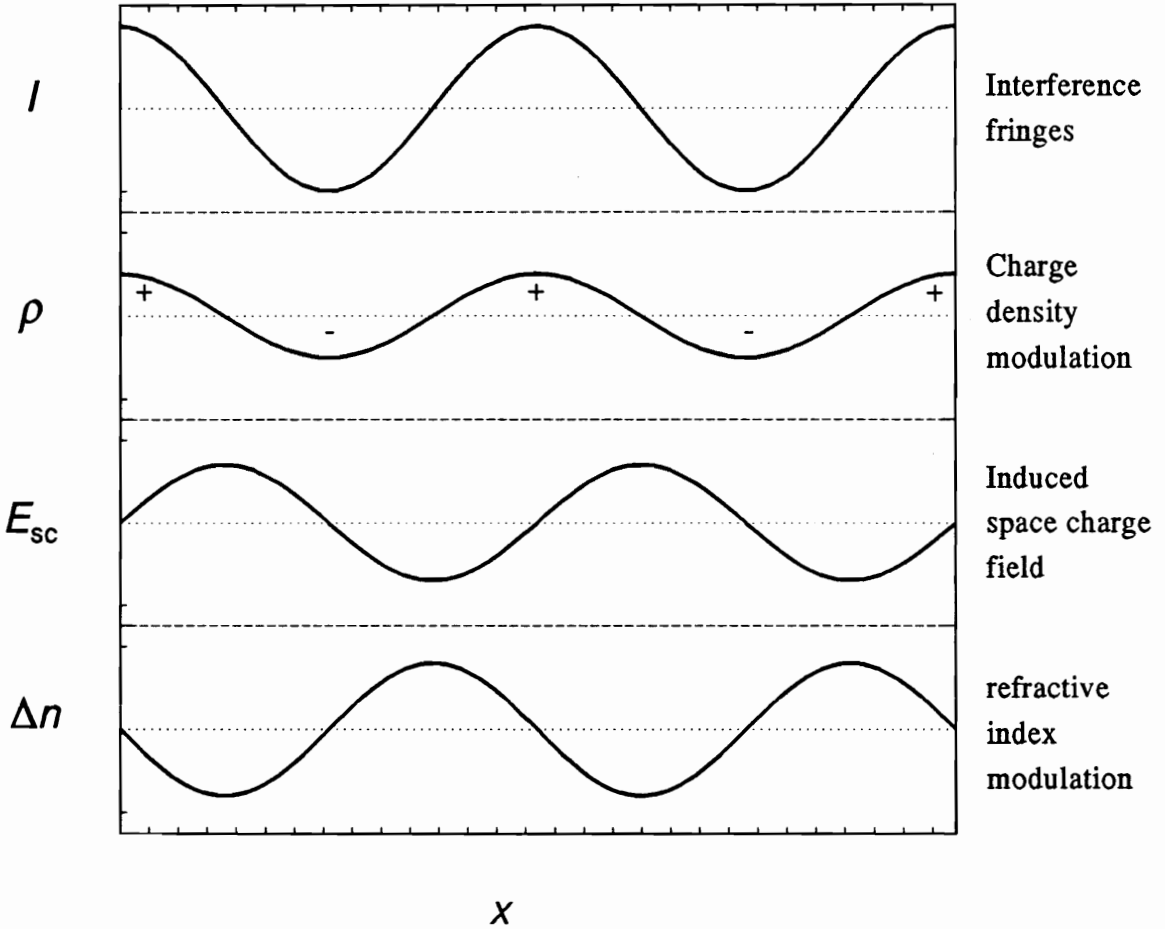


Figure 4.1: The band-transport model after Kukhtarev *et al* [65]. (a) Photo-electrons are excited into the conduction band, and re-trapped into empty donors in other sites. (b) The space charge field E_{sc} created by this redistribution of charge creates a index grating via the linear Pockel effect. Notice that there is a phase shift between the index grating and the interference fringes. This phase difference results in one of the beam being amplified at the expense of the other beam.

The bright fringes create a larger photoproduction rate of electrons at the fringe locations. These electrons migrate to the dark regions through diffusion and/or drift and are trapped by the acceptors. The charge density $\rho(\vec{r})$ in the bright regions is, therefore, positive relatively to the dark regions. The charge distribution induces a space charge field $E_{sc}(\vec{r})$, and this field distorts the index ellipsoid and induces a change of refractive index Δn via the linear electro-optic effect [67]. For small modulation, Δn is found to be

$$\Delta n = -\frac{1}{2}n_o^3 r_{eff} E_g, \quad (4.4)$$

where r_{eff} is the effective electro-optic coefficient which describes the change of the index ellipsoid with the space charge field along the direction of E_{sc} . In general, the r_{eff} is maximum along a direction which is dictated by the structure of the electro-optic tensor and geometrical parameters such as the incident angles of the mixing beams. A more detailed calculation of r_{eff} will be discussed in section 4.2.2, and its optimization will be discussed in section 4.4.1. Under the assumption that the change in refractive index is small, one writes Δn and E_{sc} as first order modulation

$$\begin{aligned} \Delta n &= \frac{1}{2}n_I e^{i\vec{k}_g \cdot \vec{r}} + \text{c.c.}, \\ E_{sc} &= \frac{1}{2}\tilde{E}_{sc} e^{i\vec{k}_g \cdot \vec{r}} + \text{c.c.}, \end{aligned} \quad (4.5)$$

then, on substituting equation 4.5 into equation 4.4

$$n_I = -\frac{1}{2}n_o^3 r_{eff} \tilde{E}_{sc}. \quad (4.6)$$

In general, the phase grating has a phase shift ϕ (spatial shift of the grating) with respect to the interference fringes and depends on m . Therefore, the index grating modulation can be written as [68]

$$n(\vec{r}) = n_o + \frac{1}{2}n_I e^{i\vec{k}_g \cdot \vec{r}} m e^{-i\phi} + \text{c.c.} \quad (4.7)$$

Using the band-transport model, \tilde{E}_{sc} and ϕ are found to be [65]

$$\begin{aligned} \tilde{E}_{sc} &= E_p \left[\frac{E_o^2 + E_d^2}{E_o^2 + (E_d + E_p)^2} \right]^{1/2}, \\ \tan \phi &= \frac{E_d(E_d + E_p) + E_o^2}{E_o E_p}, \end{aligned} \quad (4.8)$$

where E_o is a spatially uniform field applied in the direction of E_{sc} , E_d and E_p are the electric field characteristic of diffusion and the maximum space charge field achievable with the available number of traps, respectively,

$$\begin{aligned} E_d &= \frac{k_B T k_g}{e}, \\ E_p &= \frac{e p_d}{\epsilon_o \epsilon k_g}. \end{aligned} \quad (4.9)$$

In this equation $k_g = |\vec{k}_g|$, k_B is the Boltzmann's constant, T is the absolute temperature, e is the electron charge, ϵ_o is the permittivity of free space, ϵ is the dc relative permittivity of the material (which is geometry dependent, and will be calculated in section 4.2.2), and p_d is the density of traps.

On substituting equation 4.7 into the wave equation 1.10 and using the dielectric constant (at optical frequency) $\epsilon(\vec{r}) = [n(\vec{r})]^2$, the wave equation becomes explicitly dependent on $n(\vec{r})$:

$$\nabla^2 E + \frac{\omega^2}{c^2} [n(\vec{r})]^2 E - \mu_o \frac{\partial}{\partial t} \sigma E = 0, \quad (4.10)$$

where σ is the conductivity of the material, E is the sum of all the optical frequency electric fields in the material,

$$E = E_s + E_1. \quad (4.11)$$

On substituting E and equation 4.1 into the wave equation 4.10, and extracting the components that match the phase of E_s and E_1 , the wave equation is split into two parts :

$$\begin{aligned} \nabla^2 E_s + \frac{\omega^2}{c^2} n_o^2 E_s + \frac{\omega^2}{c^2} n_o n_{Im} e^{-i\phi} E_1 + i\omega \mu_o \sigma E_s &= 0, \\ \nabla^2 E_1 + \frac{\omega^2}{c^2} n_o^2 E_1 + \frac{\omega^2}{c^2} n_o n_{Im}^* e^{i\phi} E_s + i\omega \mu_o \sigma E_1 &= 0. \end{aligned} \quad (4.12)$$

The phase matching condition is imposed to select the non-vanishing terms. This condition can be understood by realizing that the wave equation 4.10 can also be expressed in an integral form with integral limits equal to that of the interaction length l in the material. Under the assumption that $2\pi \ll (\vec{k}_s - \vec{k}_g) \cdot \vec{r}$, and $(\vec{k}_g - \vec{k}_1) \cdot \vec{r}$, the terms with these phase terms vanish under the integrations. A more physical picture

of the phase matching condition is shown in figure 4.2. In this figure, the field E_s and E_1 induce a phase grating with the wave vector \vec{k}_g . To produce a field from the total field E illuminating on the grating, the vector sum of the wave vectors of the incident field and the grating vector must match the wave vector of the field. For example, to produce E_1 , E_s is scattered from the grating, the wave vector \vec{k}_1 is the combination of

$$\vec{k}_1 = \vec{k}_s - \vec{k}_g. \quad (4.13)$$

Therefore, the field E_s scattered from the modulation m^* will produce a wave in the direction of E_1 . Similarly, the field E_1 scattered from the modulation m produces a wave in the direction of E_s .

The equations 4.12 can be simplified by using the slowly varying envelop approximation (SVEA) [18]. In SVEA, the amplitudes A_j are assumed to be varying slowly both in time (comparing with one cycle) and in space (compared with one wavelength) such that $\frac{1}{A_j} \frac{\partial A_j}{\partial r_j} \ll |\vec{k}_j|$ and $\frac{1}{A_j} \frac{\partial A_j}{\partial t} \ll \omega, j = 1, s$. Using this approximation, the terms $\frac{\partial^2 A_j}{\partial r_j^2}$ can be neglected. Further simplification can be made by assuming that the angles of incidence of the beams are roughly the same for the two beams, such that $\alpha_s = \alpha_1 = \alpha'$ and $\frac{\partial}{\partial r} = \cos \alpha' \frac{\partial}{\partial z}$. The coupled wave equation 4.12 is then simplified to :

$$\begin{aligned} \frac{\partial A_s}{\partial z} - i \frac{\omega}{2c \cos \alpha'} n_I m e^{-i\phi} A_1 + \alpha A_s &= 0, \\ \frac{\partial A_1}{\partial z} - i \frac{\omega}{2c \cos \alpha'} n_I m^* e^{i\phi} A_s + \alpha A_1 &= 0, \end{aligned} \quad (4.14)$$

where $\alpha = \frac{\mu_o \sigma c}{2n_o}$ is the linear absorption coefficient. The phase shift in equation 4.14 is an important variable in determining the energy exchange of the interacting beams. A phase difference $\phi \neq 0$ leads to energy coupling between the two interacting beams, and the exchange is maximum when $\phi = \pi/2$ [69]. As a result, a weaker beam can be amplified at the expense of the stronger beam. This provides a means for coherent image amplification of the weaker signal beam of up to more than 1000 times using a single crystal BaTiO₃ [70]. This phenomenon is generally referred to as two-wave mixing (2WM) in photorefractive media since two interacting beams are present inside

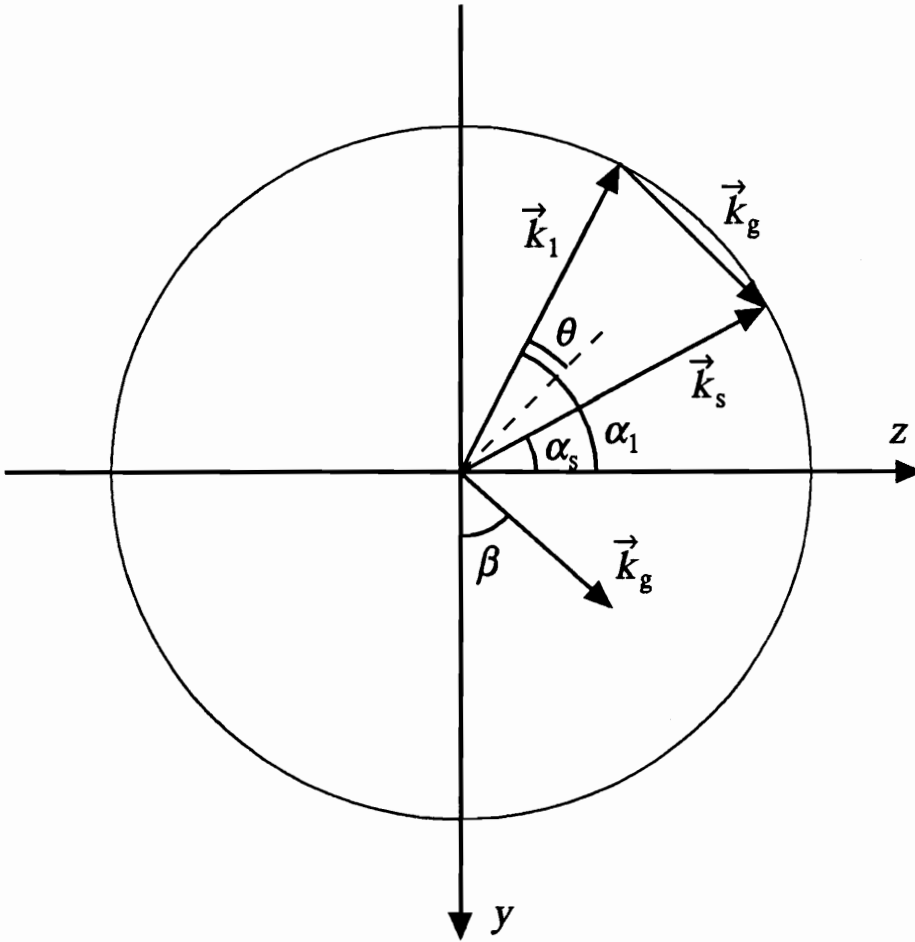


Figure 4.2: Wave vector diagram for two-wave mixing. The grating wave vector $\vec{k}_g = \vec{k}_s - \vec{k}_1$. To obtain \vec{k}_s from \vec{k}_1 , the field E_1 with wave vector k_1 is scattered from the grating with wave vector \vec{k}_g .

the interacting region.

4.2.2 Photorefractive effect in BaTiO₃

To demonstrate the dependence of r_{eff} on geometrical factors, the example of photorefractive BaTiO₃ is chosen.

A single crystal BaTiO₃ has a tetragonal structure at room temperature, and it belongs to point group $4mm$ (symmetry C_{4v}) (a detailed description of its structure and properties relevant to our discussion can be found in Klein [71]). It has a large coefficient in its electro-optic tensor which results in a large r_{eff} and a large index grating modulation when the grating direction is properly selected. It also has a large dielectric constant which results in slow response time [71]. A list of material constants of BaTiO₃ for the following calculation is shown in table 4.1.

The effective electro-optic coefficient r_{eff} is given by [20, 68] :

$$r_{eff} = \frac{-1}{n_\lambda n_o^3} (\hat{e}_3 \cdot \vec{\epsilon}_\omega) (\vec{\mathcal{R}} \cdot \hat{e}_g) (\vec{\epsilon}_\omega \cdot \hat{e}_2), \quad (4.15)$$

where n_λ is either n_e or n_o depending on whether the mixing beams have either extraordinary or ordinary polarization. The dielectric tensor (at optical frequency) $\vec{\epsilon}_\omega$ is diagonal in a coordinate system attached to the crystal principal axes. In the following calculation, the optical axis \hat{c} is along the y direction, and the x axis is out of the plane of the paper (figure 4.3). \hat{e}_g is the grating unit vector, $\hat{e}_g = \vec{k}_g / |\vec{k}_g|$. $\vec{\mathcal{R}}$ is the third rank electro-optic tensor. Using the coordinate system in figure 4.3, $\vec{\mathcal{R}}$ for BaTiO₃ is given by [67]

$$\vec{\mathcal{R}} = \begin{matrix} & \begin{matrix} x & y & z \end{matrix} \\ \begin{matrix} xx \\ yy \\ zz \\ yz \\ xz \\ xy \end{matrix} & \begin{pmatrix} 0 & 0 & r_{13} \\ 0 & 0 & r_{33} \\ 0 & 0 & r_{13} \\ 0 & r_{42} & 0 \\ r_{42} & 0 & 0 \\ 0 & 0 & 0 \end{pmatrix} \end{matrix} \quad (4.16)$$

Table 4.1: Material parameters used for the calculations

parameter	value	description
n_e	2.424	extraordinary refractive index at $514nm$
n_o	2.488	ordinary refractive index at $514nm$
$\epsilon_{ }$	4300	DC dielectric constant (electric field parallel \hat{c})
ϵ_{\perp}	106	DC dielectric constant (electric field perpendicular \hat{c})
p_d	$2 \cdot 10^{22} m^{-3}$	trap density

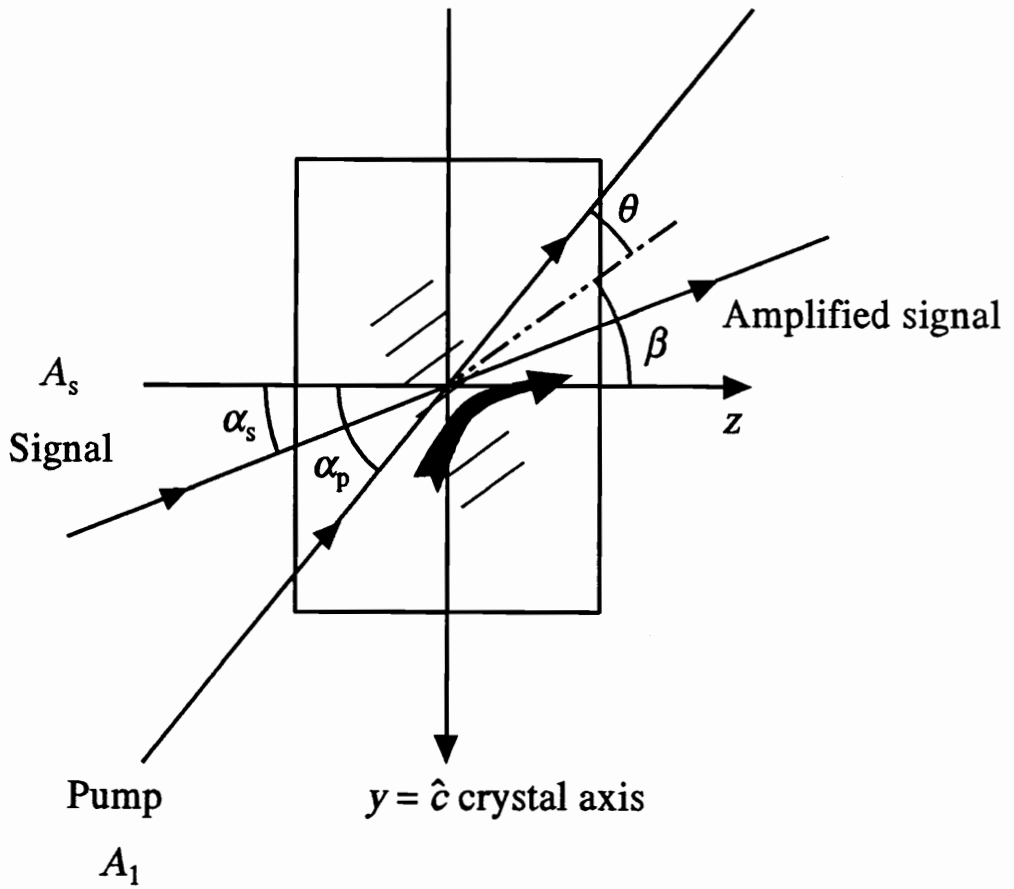


Figure 4.3: Two-wave mixing Geometry. The two interacting beams are the signal beam A_s and the pump beam A_1 . The angles α_s and α_p represent the angle between the signal beam and the pump beam with the z -axis respectively. These angles are defined inside the crystal.

and thus

$$\vec{\mathcal{R}} \cdot \hat{e}_g = \sum_{k=x,y,z} r_{ijk} e_{gk} = \begin{pmatrix} r_{13}e_{gz} & 0 & r_{42}e_{gx} \\ 0 & r_{33}e_{gz} & r_{42}e_{gy} \\ r_{42}e_{gx} & r_{42}e_{gy} & r_{13}e_{gz} \end{pmatrix}. \quad (4.17)$$

The values of r_{13} , r_{33} , r_{42} , in the unit of $10^{-12}V/m$ are 8, 23, and 820 respectively at $30^\circ C$. It is to be noted that the r_{42} is much larger than the other two coefficients.

To find an expression for r_{eff} in which the beam incidence angles appear explicitly, two angular parameters are commonly defined. They are the angle 2θ between the signal and the pump 1 and the angle β between the grating vector and the crystal axis :

$$\begin{aligned} \theta &= \frac{\alpha_s - \alpha_p}{2}, \\ \beta &= \frac{\alpha_s + \alpha_p}{2}, \end{aligned} \quad (4.18)$$

where α_s and α_p are the angles between the signal and the pump with the z -axis respectively, as shown in figure 4.3.

Ordinary-polarization beams : When ordinary polarized beams are used (polarization normal to the plane of figure 4.3), and using the coordinate system defined in figure 4.3, the polarization vectors and the grating vector are given by

$$\begin{aligned} \hat{e}_2 &= \hat{e}_3 = \begin{pmatrix} 1 \\ 0 \\ 0 \end{pmatrix}, \\ \hat{e}_g &= \begin{pmatrix} 0 \\ -\cos \beta \\ -\sin \beta \end{pmatrix}, \\ \vec{\epsilon}_\omega &= \begin{pmatrix} n_o^2 & 0 & 0 \\ 0 & n_e^2 & 0 \\ 0 & 0 & n_o^2 \end{pmatrix}. \end{aligned} \quad (4.19)$$

On substituting these relationships into equation 4.15, a simple form for the effective electro-optic coefficient is found :

$$r_{eff} = r_{13} \sin \beta. \quad (4.20)$$

Extraordinary-polarization beams : When extraordinary polarized beams are used in the two- or four-wave mixing (polarization in the plane of figure 4.3), the following expressions for the polarization vectors, in addition to the grating unit vector \hat{e}_g given in equation 4.19, are used :

$$\hat{e}_2 = \begin{pmatrix} 0 \\ \cos \alpha_p \\ -\sin \alpha_p \end{pmatrix}; \quad \hat{e}_3 = \begin{pmatrix} 0 \\ \cos \alpha_s \\ -\sin \alpha_s \end{pmatrix}. \quad (4.21)$$

On substituting these vectors into equation 4.15, the effective electro-optic coefficient is calculated as

$$r_{eff} = \frac{1}{2n_o^3n_e} (n_e^4 r_{33} \sin \beta \cos \alpha_s \cos \alpha_p + 4n_o^2 n_e^2 r_{42} \cos \beta \sin 2\beta + n_o^4 r_{13} \sin \beta \sin \alpha_p \sin \alpha_s). \quad (4.22)$$

In comparing equation 4.20 and equation 4.22, it is seen that when the interacting beams have ordinary polarization, r_{eff} does not contain the large electro-optic coefficient r_{42} . Therefore, it is concluded that the interacting beams have to be in extraordinary polarization in order to construct a PCM with gain using photorefractive BaTiO₃. In addition to that, the grating \hat{e}_g cannot be parallel or perpendicular to the \hat{c} axis.

The relative permittivity in equation 4.9 depends on the grating direction \hat{e}_g , and it is given by

$$\varepsilon = \hat{e}_g \cdot \vec{\varepsilon} \cdot \hat{e}_g = \varepsilon_{\perp} \cos^2 \beta + \varepsilon_{\parallel} \sin^2 \beta, \quad (4.23)$$

where $\vec{\varepsilon}$ is the DC relative permittivity tensor. In the coordinate system given in figure 4.3, $\vec{\varepsilon}$ is diagonal, and the non-zero elements are given by $\varepsilon_{11} = \varepsilon_{33} = \varepsilon_{\perp} = 106$ and $\varepsilon_{22} = \varepsilon_{\parallel} = 4300$ [67].

4.3 Phase conjugation using degenerated four-wave mixing in photorefractive BaTiO₃

The idea to use a phase-conjugate signal to remove phase errors by means of a hologram was first introduced by Kogelnik in 1965 [72]. In this method, the in-

interference fringes of the signal and the reference beam are recorded on film. The phase-conjugate signal is generated by reading the hologram with a beam propagating in the reverse direction of the reference beam. The disadvantages of this method are that the process is not real time, and a new hologram is needed for each signal.

Since the two-wave mixing in photorefractive media can produce a real-time hologram of the signal and the reference beam, it is natural to extend this method to generate a real-time phase-conjugate signal. The four-wave mixing geometry used to produce phase conjugation is shown in figure 4.4. To generate a phase-conjugate signal, the signal beam E_4 and the pump beam E_1 (the reference beam) first induce an index grating inside the medium. A third beam E_2 is incident at the Bragg angle (therefore it is counter propagating with the pump beam E_1) on this grating. E_2 will diffract off the phase grating and generates a phase-conjugate beam which propagates in the reverse direction of the signal beam. The term four-wave mixing (4WM) refers to this physical process by which four interacting fields couple with each other in the medium. In the particular case when all four interacting beams are of the same frequency ω , then the process is referred to as degenerate four-wave mixing.

Let the electric field associated with the j th beam be

$$\vec{E}_j(\vec{r}, t) = \hat{e}_j A_j(\vec{r}) e^{i(\vec{k}_j \cdot \vec{r} - \omega t)} + \text{c.c.}, \quad (4.24)$$

where \hat{e}_j is the polarization of the beam, \vec{k}_j is the wave vector, $j = 1, 2, 3, 4$. The signal beam is A_4 , and A_1, A_2 are the two counter-propagating pump beams. The phase conjugate signal A_3 propagates in the reverse direction of A_4 . All the angles are defined inside the crystal as shown in figure 4.4.

The wave-vector diagram of the interacting beams is shown in figure 4.5. The phase conjugate beam A_3 is produced by the scattering of pump beam A_2 off a phase grating with grating vector \vec{k}_g formed by the interference of A_1 and A_4 . This phase grating consists of two elements $\vec{k}_g = \vec{k}_4 - \vec{k}_1 = \vec{k}_3 - \vec{k}_2$. The first element is produced by the interference of pump A_1 and signal A_4 . The second element is produced by the interference of pump A_2 and phase conjugate A_3 . There are three other sets of gratings with grating vector $\vec{k}_{II} = \vec{k}_1 - \vec{k}_3 = \vec{k}_4 - \vec{k}_2$, $\vec{k}_{III} = \vec{k}_1 - \vec{k}_2$, and $\vec{k}_{IV} =$

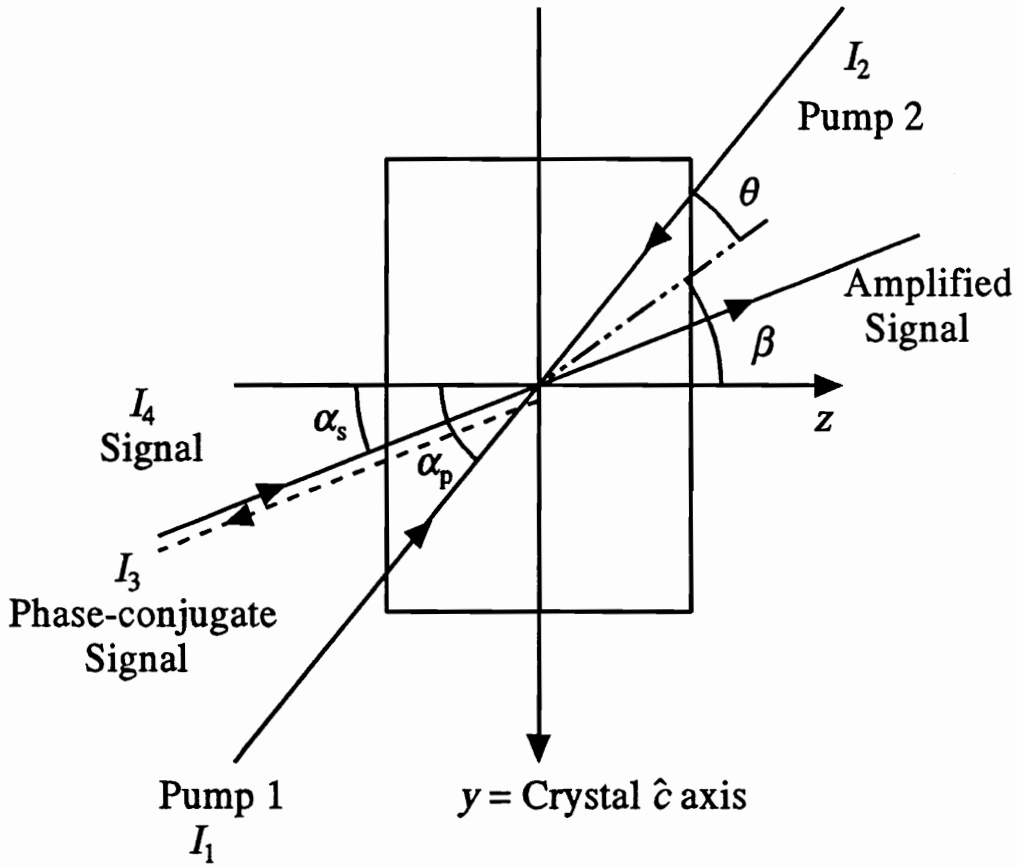


Figure 4.4: Degenerate four-wave mixing geometry. The four interacting beams are A_j , $j = 1, 2, 3, 4$. A_1 and A_2 are counter propagating pump beams usually referred to as pump 1 and pump 2 respectively, A_4 is the signal beam, and A_3 is the phase conjugate beam. α_s and α_p are the angle of the signal beam and the pump A_1 with the z -axis respectively. These angles are defined inside the crystal.

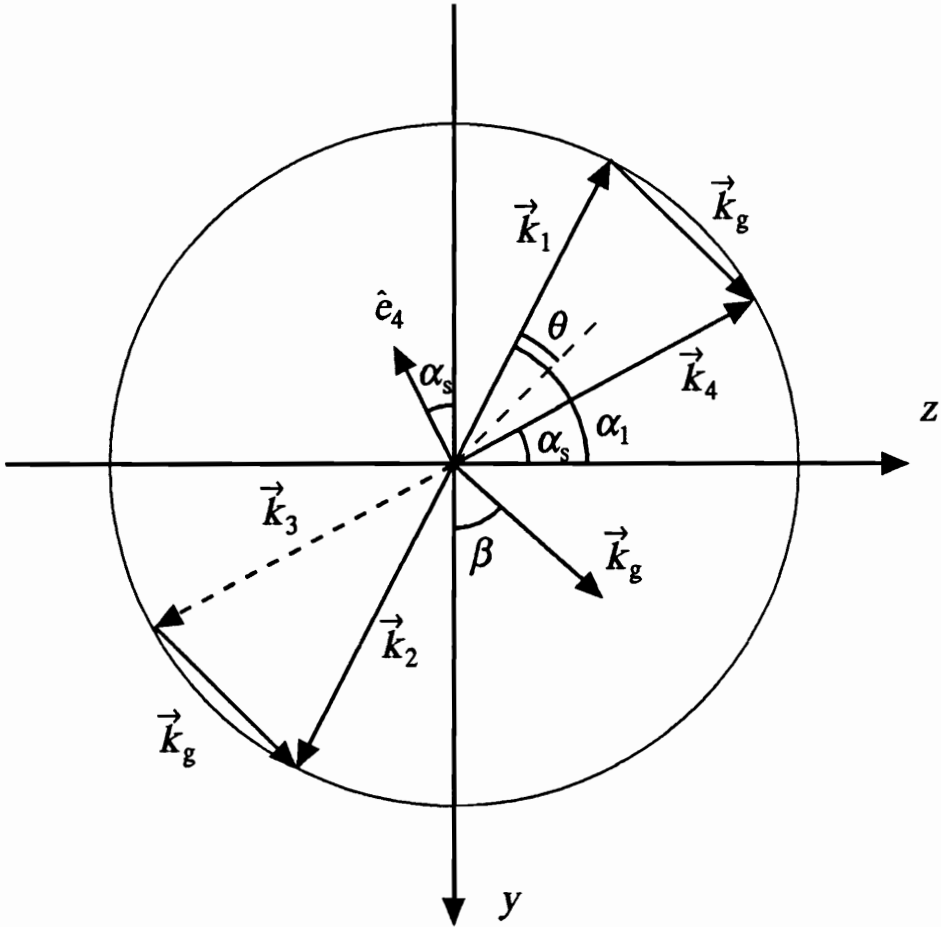


Figure 4.5: Wave vectors diagram for four-wave mixing. In the transmission grating only approximation, the grating wave vector $\vec{k}_g = \vec{k}_4 - \vec{k}_1 = \vec{k}_3 - \vec{k}_2$. β is the angle of the grating vector make with the crystal axis. 2θ is the angle between the signal and the pump A_1 . If A_4 has ordinary polarization, \hat{e}_4 is pointing out of the paper. If A_4 has extraordinary polarization, \hat{e}_4 is on the plane of the paper.

$\vec{k}_3 - \vec{k}_4$. They are formed by the interference of the various beams present inside the interacting region. These grating vectors all have magnitude larger than that of \vec{k}_g , $|\vec{k}_j| > |\vec{k}_g|, j = II, III, IV$. The resultant index gratings generated by these grating vectors all have a smaller magnitude than that of \vec{k}_g . In the single grating approximation, it is assumed that these gratings do not give rise to strong beam couplings, thus they are neglected. The approximation is usually appropriate under circumstances in which only one particular direction of the space-charge field leads to a strong electro-optic effect. This can be achieved either by an appropriate choice of the beam incidence angles so that the coupling coefficients of all the other gratings are small, or by the application in some cases of an electric field that enhances certain gratings. Another alternative is to use a pump A_2 which is incoherent with A_1 and A_4 .

Assuming that the beams have the same polarization, the dimensionless modulation index m , in 4WM, is

$$m = \frac{2(A_1^* A_4 + A_2 A_3^*)}{I_o}. \quad (4.25)$$

In the transmission grating only approximation (that means \vec{k}_g dominant and $\vec{k}_j, j = II, III, IV$ are negligible), the index grating with grating vector \vec{k}_g is given by replacing m in equation 4.7 with that in equation 4.25. This leads to [68]

$$n = n_o + \frac{n_I e^{-i\phi_I}}{2} \frac{A_1^* A_4 + A_2 A_3^*}{I_o} e^{i\vec{k}_g \cdot \vec{r}} + c.c. \quad , \quad (4.26)$$

where n_o is the ordinary refractive index, and $I_o = \sum_{j=1}^4 I_j$, with I_j being the intensity $|A_j|^2$ of the j th beam. For photorefractive BaTiO₃ in which diffusion is the dominant mechanism for the charge transport, the phase ϕ is $\pi/2$ [65] when no external electric field is applied. The expression for n_I is given by [65] (without externally applied field)

$$n_I = -\frac{r_{eff} n_o^3}{2} \frac{E_p E_d}{E_d + E_p}, \quad (4.27)$$

where E_d and E_p are given by in equation 4.9. In the wave equation governing the propagation of the beams in the crystal, it is customary to define a coupling coefficient

γ as

$$\gamma = \frac{i\omega n_I e^{-i\phi}}{2c \cos \alpha'}, \quad (4.28)$$

where it is assumed that the angles of the signal and the pumps with the normal of the crystal faces are the same : $\alpha_s = \alpha_p = \alpha'$, ω is the angular frequency of the laser beam, and c is the velocity of light. The coupling coefficient is therefore real in photorefractive BaTiO₃ without external applied field ($\phi = \pi/2$).

To obtain the coupled-wave equations similar to the one in equation 4.12, SVEA and the phase matching condition are employed. The incident angles of the signal and the pumps are assumed to be the same. On substituting equation 4.24 into the scalar wave equation 4.10 [68], we find

$$\begin{aligned} \frac{dA_1}{dz} &= -\gamma m A_4 - \alpha A_1, \\ \frac{dA_2}{dz} &= -\gamma m^* A_3 + \alpha A_2, \\ \frac{dA_3}{dz} &= \gamma m A_2 + \alpha A_3, \\ \frac{dA_4}{dz} &= \gamma m^* A_1 - \alpha A_4. \end{aligned} \quad (4.29)$$

4.4 Optimization of the PCM gain

To optimize the PCM gain, one needs to maximize the photorefractive effect. This can be achieved in two ways : optimization of the geometry and of the polarization of the incident beams, and of the intensity ratios of the beams.

4.4.1 Optimization of the geometry

The optimization of the PCM geometry includes the selection of the polarization of the beams used in the four-wave mixing and the choice of incident angle for the interacting beams. The importance of these two factors is shown in this section.

In comparing equation 4.20 and equation 4.22, one concludes that the photorefractive effect is maximized if one makes use of the large electro-optic coefficient

r_{42} . For this reason, extraordinary polarization of all the beams was used in all the experiments reported in this work.

The photorefractive effect can also be enhanced by appropriate geometrical arrangement of the interacting beams. By setting the incident beam angles for the pumps and the signal beam to specific values, the energy exchange of the pumps to the phase conjugate beam can be optimized. Physically, this geometrical optimization consists of maximizing the magnitude of the phase grating n_I in equation 4.27. This maximizes the transfer of energy from the read beam A_2 to the phase-conjugate beam A_3 .

On substituting the material parameters from table 4.1 into equation 4.27, 4.28, and 4.26, the coupling constant γ can be calculated and plotted against the angle β for various values of the angle 2θ . This is shown in figure 4.6, adapted from Fainman *et al* [70]. It is seen that maximum coupling occurs for grating vector angles β between 30° and 50° and for small values of θ . However, large grating angles inside the crystal are not achievable without index matching immersion because of the large refractive index of the crystal. This can be visualized by an example. Using the definition of β and θ in equation 4.18, the condition for optimum beam coupling (from figure 4.6) implies that values of α_s and α_p have to be roughly between 40° and 45° , and that their difference is small. However, one can only achieve angle α_s and α_p smaller than the critical angle (which is 24.4° for extraordinary polarization and 23.7° for ordinary polarization) It is therefore concluded that optimum beam angles ($\beta \simeq 40^\circ, \theta \simeq 2^\circ - 5^\circ$) are not achievable under normal circumstances. Two methods have been suggested to attain these optimum beam angles; one is to use a specially cut crystal, the other is to use immersion of the crystal in index-matching oil. The specially cut crystal method was first suggested by Fainman *et al* [70]. The cutting of the crystal is along the $(1\ 0\ 0)$, $(0\ 1\ 1)$, and $(0\ 1\ \bar{1})$ crystallographic planes [70]. Such a crystal cut will allow an orientation of the incident beams leading to $\beta = 45^\circ$. The second method to achieve optimum conditions is to immerse the crystal in an index-matching oil [49]. In this method, a prism coupler device is used to introduce the beams at the appropriate angles into the oil and then into the crystal. Using this

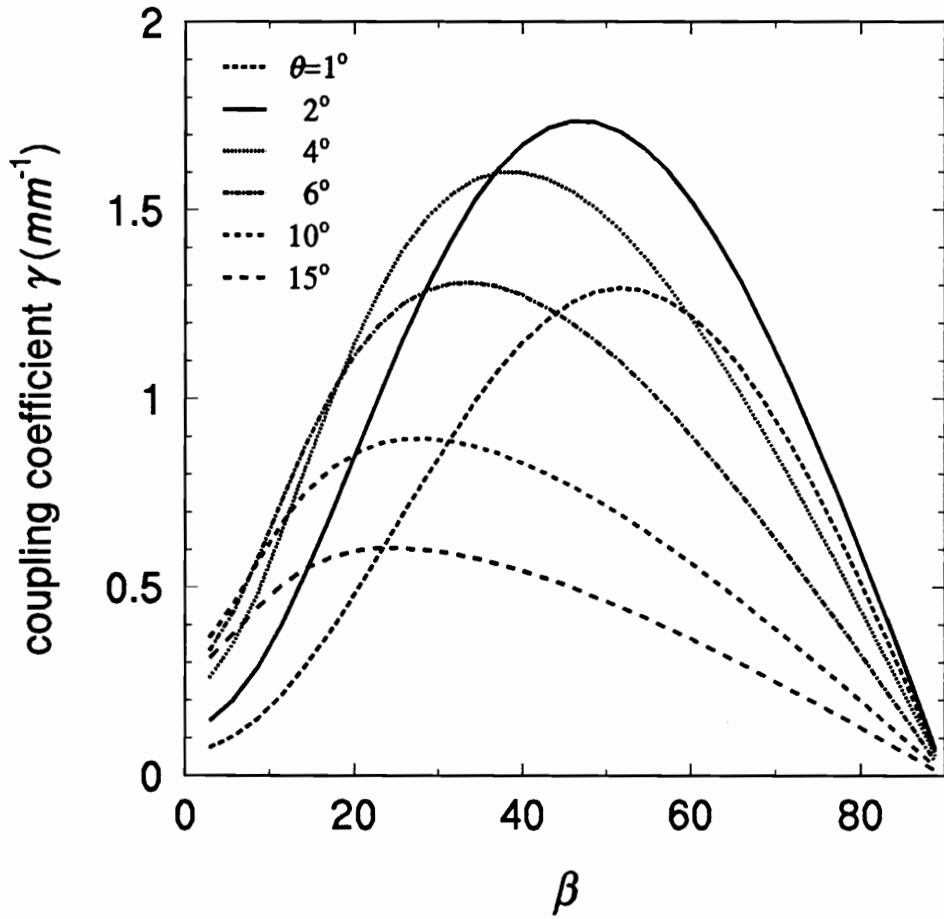


Figure 4.6: Plot of the coupling coefficient γ against the grating angle β used as the parameter (after Fainman *et al* [70]).

method, a steady-state phase-conjugate reflectivity of 50x has been reported [49]. However, optimum coupling does not necessarily lead to optimum performance. A large coupling constant does not amplify the signal only, it will also amplify the scattered noise. Very strong “fanning” effects (beam diffracted off grating resulting from the interference of amplified scattered light) have been shown to occur with the 45° cut crystal [73]. The fanning effect increases the speckle noise and may decrease the quality of the phase-conjugate image in addition to draining energy in “noisy channels”.

In our experimental arrangement, the incidence angle θ_p of pump 1 at the air-crystal interface was 48° to the normal of the crystal surface. From figure 4.7, it is seen that the optimum angle for the signal beam α_s is approximately 10° to the normal of the crystal surface. The optimum signal incident angle θ_s is therefore calculated to be approximately 25° to the normal.

In conclusion, the geometrical factor for the optimization of the beam coupling constant have been studied and maximally exploited. In our experiment, the largest beam coupling constant was obtained with the selection of extraordinary polarization beams and with beam angles $\alpha_p = 18.3^\circ$ for the pump 1 and $\alpha_s = 10^\circ$ for the signal.

4.4.2 Optimization of the intensity ratios of the interacting beams

To find the optimum beam ratios leading to the highest PCM reflectivity, the following analysis is outlined which follows closely the theoretical model given by Cronin-Golomb *et al* [68].

In the general case the coupled-wave equations 4.29 cannot be solved analytically. They have to be solved by numerical integration. However, in the case of negligible absorption and with the transmission grating only approximation, an analytical solution has been found by Cronin-Golomb [68]. The intensity reflectivity $R_{PCM} = |\mu|^2$ of a PCM is defined as

$$R_{PCM} = \frac{A_3^*(0)A_3(0)}{A_4^*(0)A_4(0)}, \quad (4.30)$$

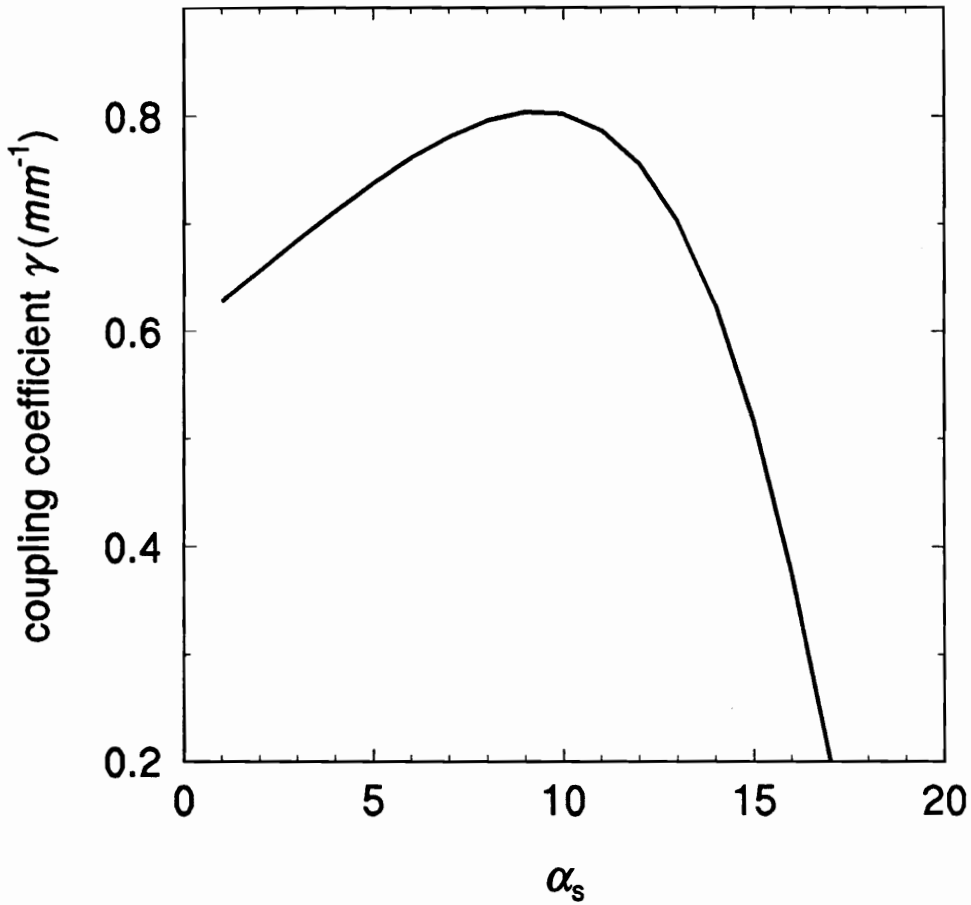


Figure 4.7: Plot of the coupling coefficient against the signal beam angle α_s , with the normal to the crystal surface. The pump 1 angle α_p is 18.4° . This curve shows that the optimum α_s is around 8° to 10° .

where A_3 and A_4 are defined at the entrance surface of $z = 0$, and it is found to be given by

$$R_{PCM} = \frac{4|c|^2}{(Q/T + I_2(l))^2}, \quad (4.31)$$

where

$$\begin{aligned} Q &= \sqrt{\Delta^2 + 4|c|^2}, \\ T &= -\tanh(\gamma l Q / 2I_o), \\ \Delta &= I_2(l) - I_1(0) - I_4(0), \\ I_o &= \sum_{j=1}^4 I_j, \quad I_j = |A_j|^2, \end{aligned} \quad (4.32)$$

and $|c|^2$ is given by the root of the equation

$$[|c|^2 - I_1(0)I_2(l)](Q/T + \Delta)^2 + 4|c|^2[I_2(l) + Q/T]I_4(0) = 0. \quad (4.33)$$

Equation 4.33 is solved numerically using the Muller's method [55]. The result is substituted into equation 4.31 to obtain the PCM reflectivity. To determine the optimum beam intensities, it is convenient to define the beam intensity ratios

$$\begin{aligned} \text{signal-to-pump ratio, } r &= \frac{I_4}{I_1}, \\ \text{pumps ratio, } q &= \frac{I_2}{I_1}. \end{aligned} \quad (4.34)$$

A contour plot of the PCM reflectivity is shown in figure 4.8 in the $\log r - \log q$ plane. The coupling strength γl was chosen to be -4 for the calculation. It is seen that there is a spur of reflectivity for small signal-to-pump ratio at $\log r \sim -3$ to -4 and pumps ratio at $\log q \sim -2$. Some slices of this contour plot are shown in figure 4.9. It is seen that each reflectivity curve for different r reaches a maximum for a different q . This indicates that there is an optimum pumps ratio for each signal-to-pump ratio. The reflectivity peak is higher and shifts toward smaller pumps ratio for smaller signal-to-pump ratio. This indicates that large PCM reflectivity is obtainable with low signal intensity, roughly three to four orders of magnitude smaller than the intensity of pump 1, and with low intensity of pump 2. The peak of the

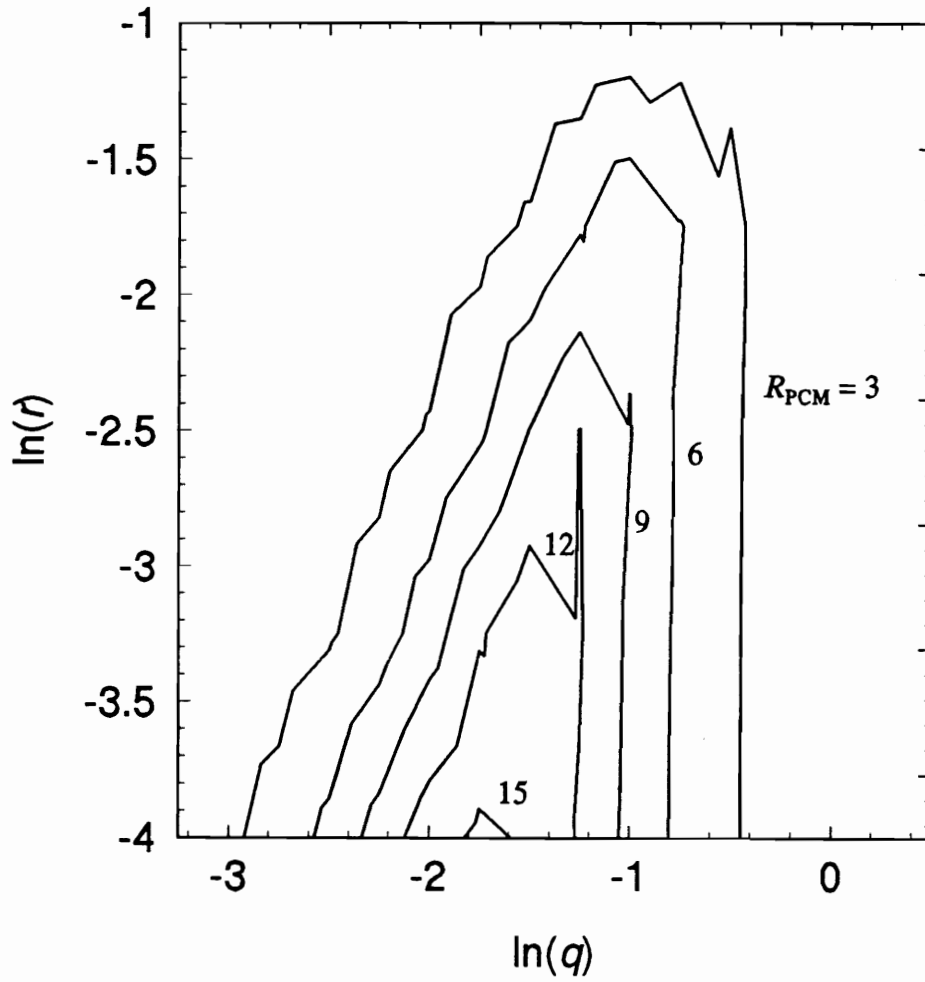


Figure 4.8: Contour plot of the PCM reflectivity versus log of signal-to-pump ratio and log of pump ratios. This contour plot is used to assist in the determination of the best beams ratio in four-wave mixing.

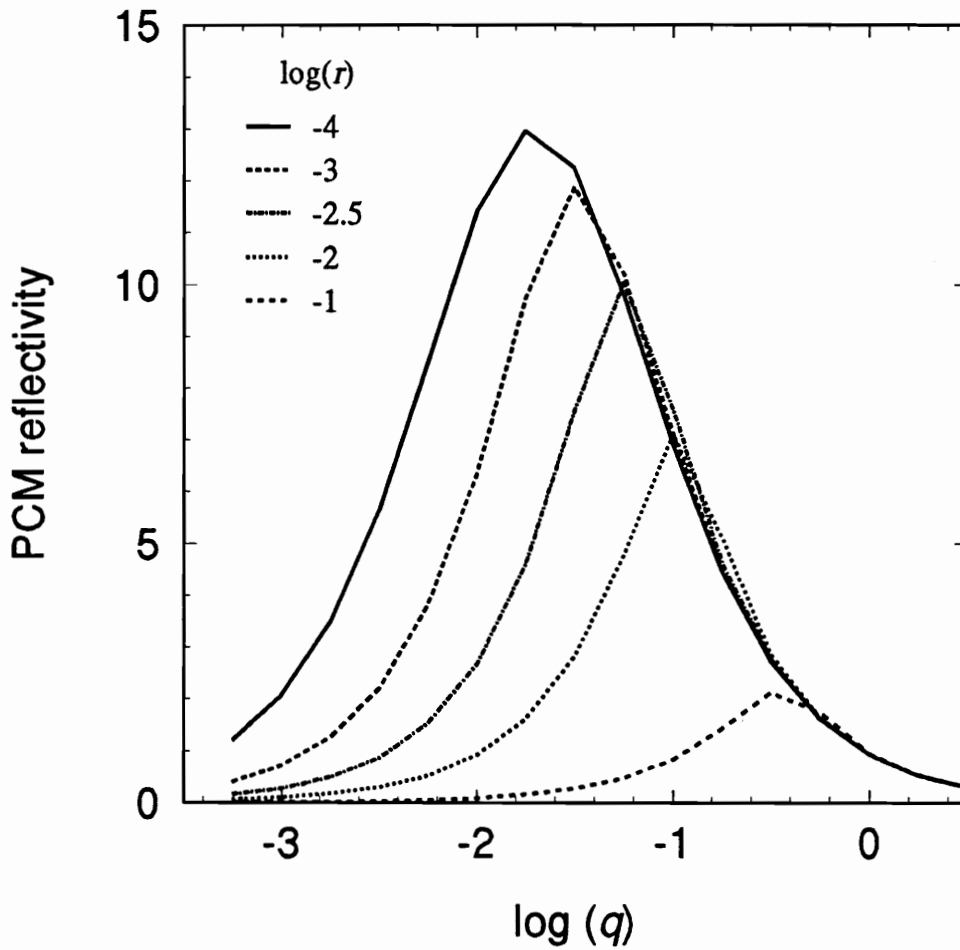


Figure 4.9: PCM reflectivity curves for various log signal-to-pump ratio. Notice that the peak of the PCM reflectivity curves slowly levels off for small signal-to-pump ratio. The peaks of these curves also shift towards smaller pump ratios.

PCM reflectivity gradually levels off with even smaller signal-to-pump ratio. Thus, an optimum signal-to-pump ratio is around $\log r = -3$ to -4 . With even smaller signal-to-pump ratio the signal-to-noise ratio (SNR) decreases as the signal strength becomes comparable to scattered noise.

4.5 Experimental measurement of the PCM reflectivity

An experiment was set up to measure and optimize the PCM reflectivity. The experimental setup is shown in figure 4.10.

A single domain crystal of photorefractive BaTiO_3 with dimension $6\text{mm} \times 5\text{mm} \times 5\text{mm}$ is used as the PCM. The crystal was grown by and purchased from Sanders Associates. The crystal c -axis is parallel to the long edge of the crystal. The crystal appears to be transparent with a pale yellow colour. The absorption coefficient for extraordinary polarized light at 514nm is measured to be 0.11mm^{-1} . The large absorption coefficient is an indication that the analytical solution discussed in section 4.4.2 may not predict accurately the performance of the PCM.

The incidence angles of the various beams are shown in figure 4.11. The angles inside the crystal are calculated, using Snell's law, to be $\alpha_s = 3.3^\circ$ and $\alpha_p = 18.4^\circ$ for the signal and pump 1 respectively. The corresponding coupling coefficient γ , determined using figure 4.7, is found to be approximately 0.7mm^{-1} about 6 times larger than the absorption coefficient α .

The phase-conjugate signal I_{conj} is extracted using a pellicle beam splitter (PBS), and its intensity is measured by a power meter equipped with a silicon photodiode. The PBS is set at an incident angle $\theta = 28^\circ$. At this angle the reflectivity $R_{PBS(\theta)}$ of the PBS, for the extraordinary polarization, is 0.104.

The powers of the beams I_1 , I_2 , and I_4 are measured using another power meter before they enter into the crystal. When I_{conj} reaches a steady state, the intensity

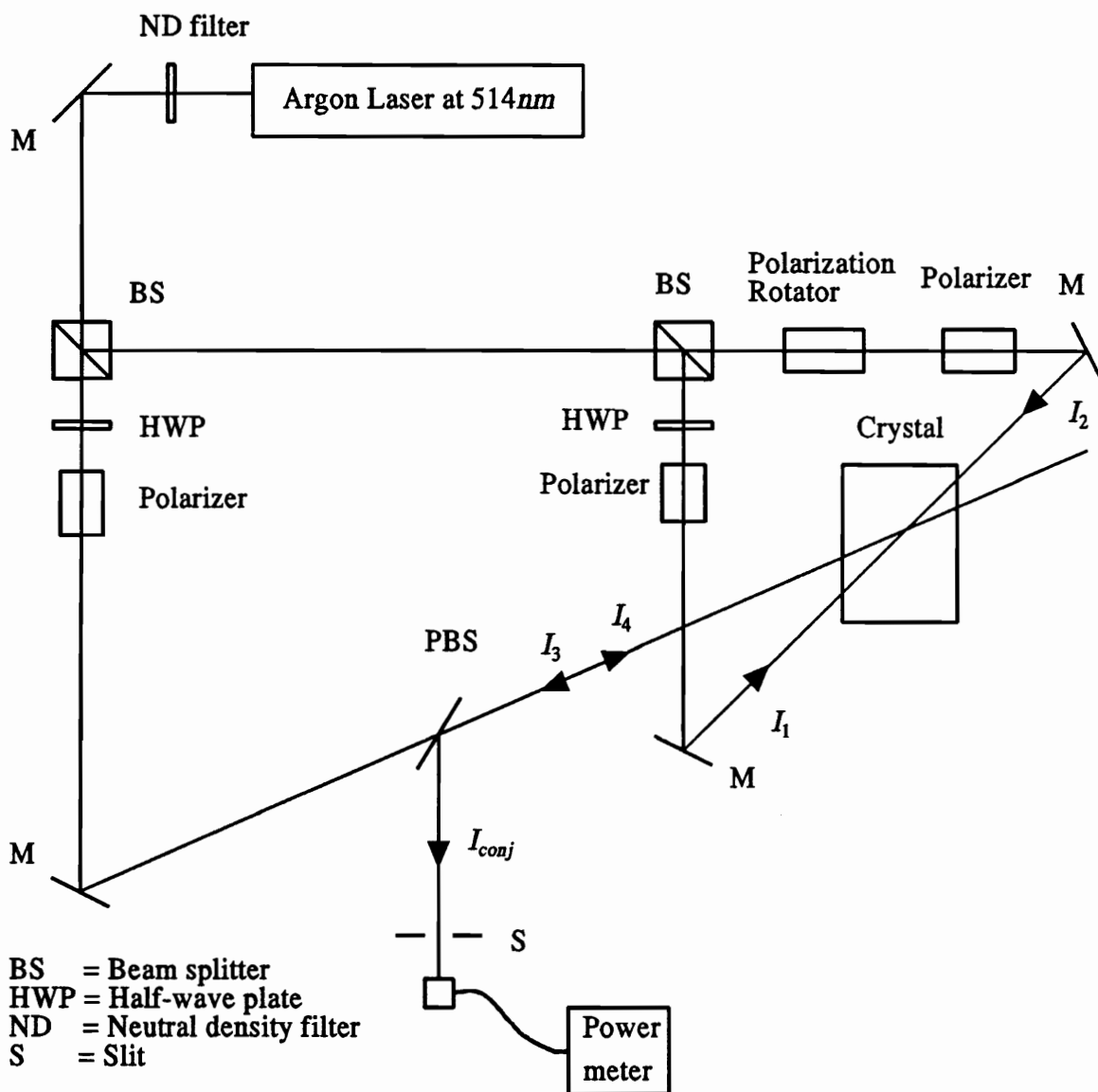


Figure 4.10: Experimental setup for the measurement of the PCM reflectivity. All the four interacting beams A_i , $i = 1, 2, 3, 4$ have extraordinary polarization. Their intensity were controlled either by the combination of a half-wave plate and a calcite polarizer, or by the combination of a polarization rotator and a calcite polarizer.

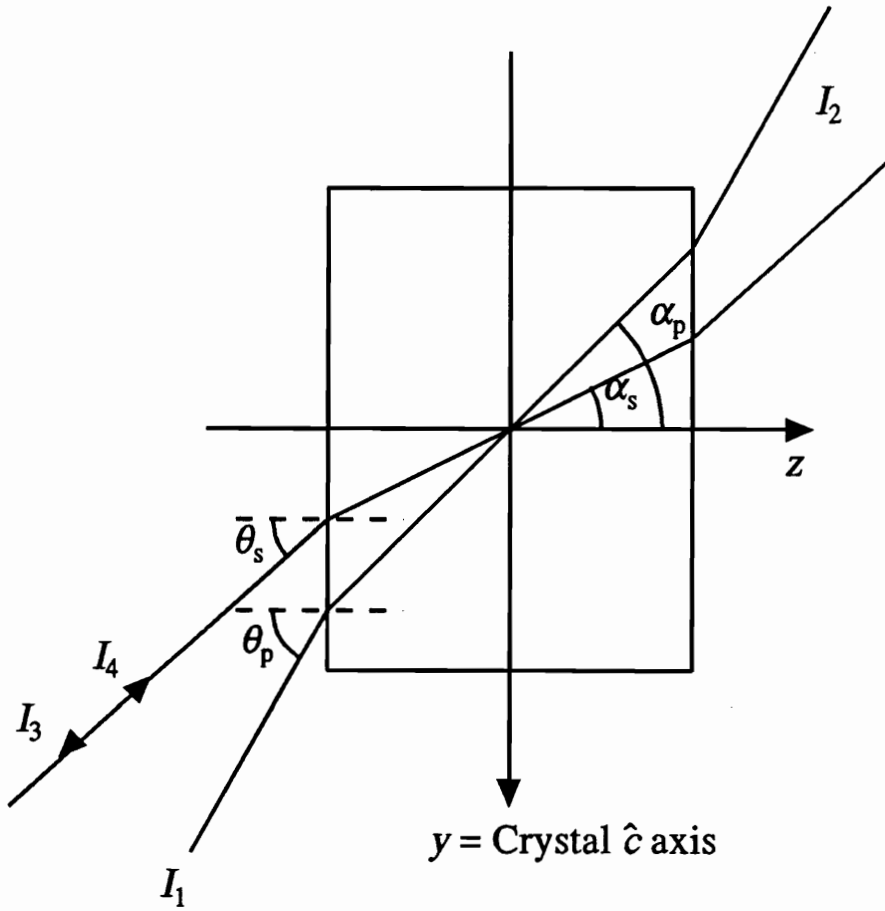


Figure 4.11: Expanded geometry of the interacting beams in four-wave mixing. θ_s and θ_p are the incidence angles of the signal and pump 1 respectively.

reflectivity R_{PCM} of the PCM is determined using

$$R_{PCM} = \frac{I_{conj}}{I_4} \frac{1}{R_{PBS(28^\circ)}}. \quad (4.35)$$

In the following sections, the phase conjugate reflectivity with various signal-to-pump and pumps ratios is determined experimentally.

4.5.1 PCM reflectivity versus pumps ratio

For this measurement, the power of the signal I_4 was fixed at $0.33\mu W$. The diameter of the laser beams was about $2mm$. The power of the beams was measured instead of the intensity. In the case where the angles of all the beams with the normal to the crystal faces are roughly the same, the ratios of the power are approximately equal to the ratios of the intensity in equation 4.34. The PCM reflectivity was measured with various powers of the pump 2 (I_2), and the power of pump 1 (I_1) was used as a parameter to generate different PCM reflectivity curves. These curves are given in figure 4.12.

When comparing figure 4.12 with figure 4.9, it is seen that the theoretical plot shares some common features with the experimental data in figure 4.12. These features include (1) a peak PCM reflectivity for each curve; and (2) the peaks of the curves reaches a plateau of maximum reflectivity as the signal-to-pump ratio becomes small.

While these two figures share some similarities, some disagreements between theory and experiment are visible. Two discrepancies between the experimental data and the theoretical calculation can be identified.

First, the peaks in the measured reflectivity curves appear at different location from that of the theoretical curves. For example, the experimental PCM reflectivity curves display a maximum reflectivity at pumps ratio of $\log q \sim -0.4$. The theoretical PCM reflectivity curve, with the same signal-to-pump ratio r , peak at $\log q = -1.3$. This indicates that a higher pump 2 intensity is needed in experiment than the theoretical prediction to achieve the peak reflectivity. Secondly, the peaks of the PCM

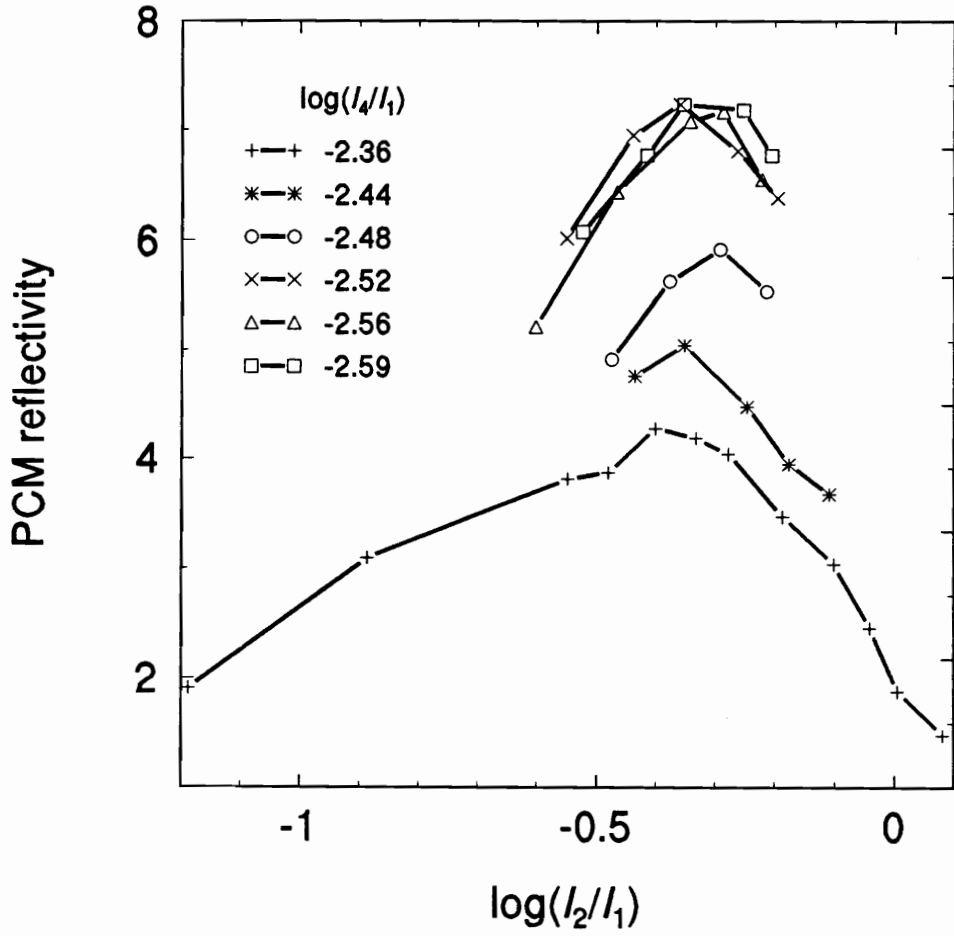


Figure 4.12: Experimental measurement of PCM reflectivity against log pump ratios for fixed signal-to-pump ratio. These curves show a saturation of the PCM reflectivity when $\log r \leq -2.5$.

reflectivity curves appear for the same pumps ratio for the range of signal-to-pump ratios used. This is different from the theoretical curves in which the peaks shift to a smaller pumps ratio for smaller signal-to-pump ratio. Furthermore, the measured reflectivity curves show a narrower range of signal-to-pump ratio, from $\log r = -2.36$ to -2.5 , to produce peak height saturation. The range of signal-to-pump ratio in the analytic solution show peak height saturation is at $\log r < -4$ (figure 4.9).

4.5.2 PCM reflectivity against signal-to-pump ratio

In the second set of measurements, the intensity of pump 1 and pump 2 were fixed at $110\mu W$ and $50\mu W$ respectively. The PCM reflectivity was measured with various input intensities for the signal.

The results of the measurements are shown in figure 4.13. Several theoretical plots are shown in the same figure. It is seen that the trend of the falling PCM reflectivity with increasing signal-to-pump ratio is roughly the same as that obtained from the theoretical model. However, the corresponding pumps ratio does not match what is calculated from the theoretical model. Again, there is roughly one order of magnitude difference in the pumps ratio between the theory and the experiment for the corresponding PCM reflectivity.

4.5.3 PCM reflectivity against total beam intensity

In the third set of measurements, the signal-to-pump power ratio was fixed at $\log r = -2.5$. The reflectivity of the PCM was measured as a function of the pump ratio, and the total intensity of the beams is used as the parameter.

The results of the measurements are shown in figure 4.14. Two sets of measurements were made with I_1 fixed at $110\mu W$ and $220\mu W$, and I_4 at $0.3\mu W$ and $0.6\mu W$ respectively. It is observed that the shapes of the two curves are similar, and the locations of the peaks are about the same, at $\log(I_2/I_1) = -0.36$. However, the reflectivity curve with $I_1 = 110\mu W$ is higher than the one with $I_1 = 220\mu W$ by

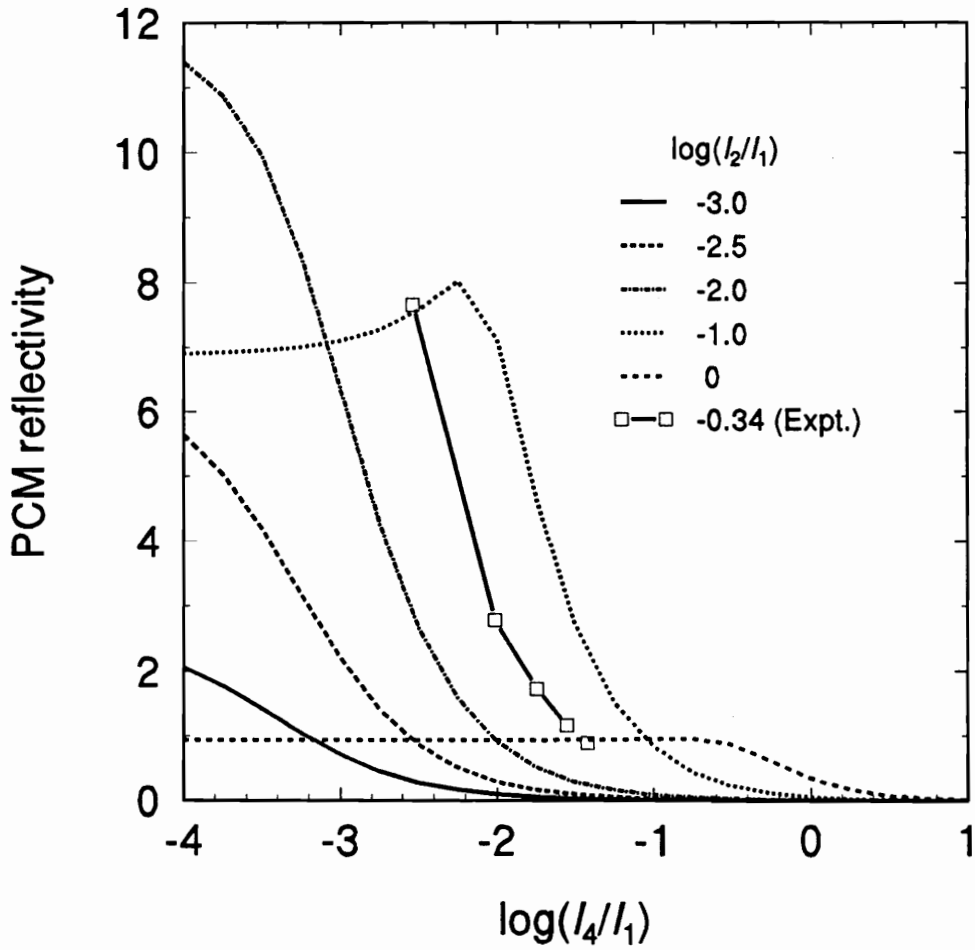


Figure 4.13: Experimental measurement of PCM reflectivity against log signal-to-pump ratio for fixed pumps ratio. The reflectivity curve shows a decrease in reflectivity with increasing signal-to-pump ratio, which is consistent with the theoretical curve.

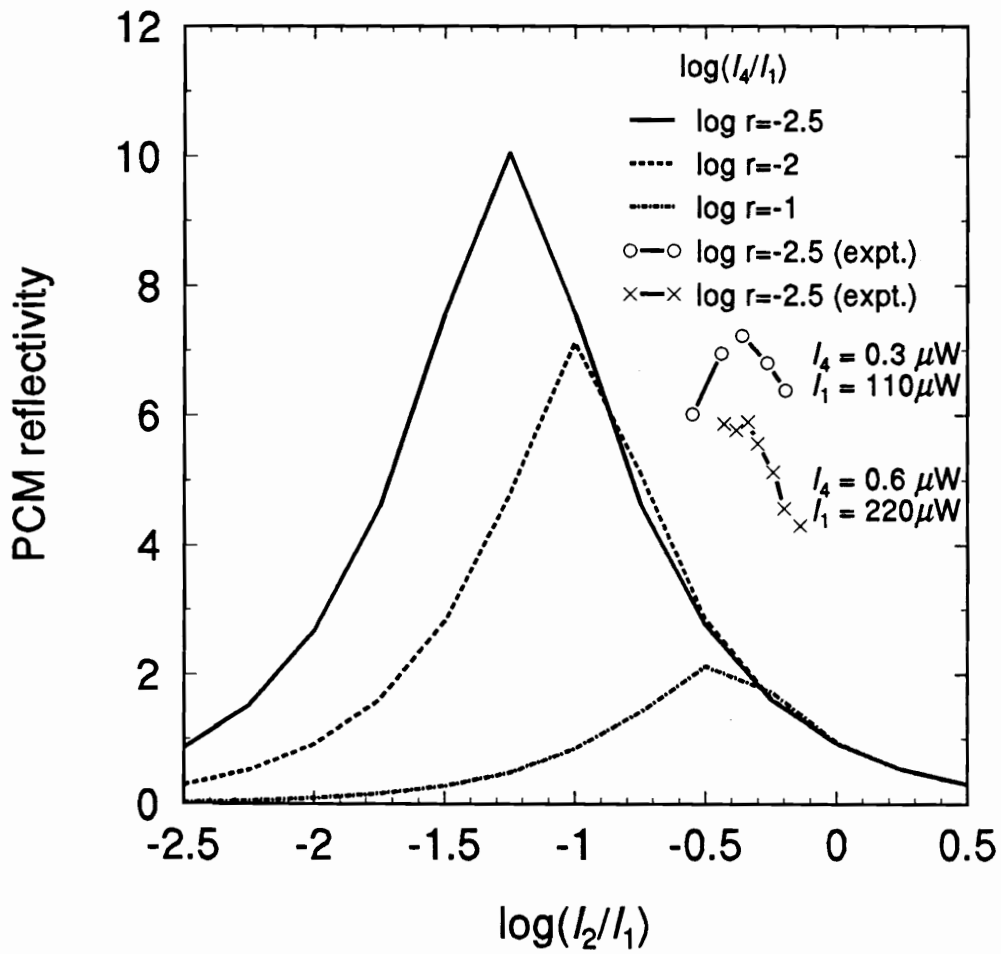


Figure 4.14: Experimental measurement of PCM reflectivity against total beam intensity for a fixed signal-to-pump ratio. The curves show that the reflectivity decreases with increasing the total beams intensity.

17%. This indicates that the PCM reflectivity also depends on the total intensity I_o of the beams interacting inside the crystal. This dependence is predicted theoretically by the relationship $T = -\tanh(\gamma IQ/2I_o)$ in equation 4.32. As I_o increases, $\lim_{x \rightarrow 0^+} \tanh(x) = x$. The theory thus predicts a decrease of reflectivity as I_o increases. The same trend is shown by the experimental results.

Some theoretical curves are plotted along with the experimental data in figure 4.14. The peak reflectivity of $\log r = -2.5$ is larger than the experimental values by roughly 30%. This can be accounted for by the absorption that was not incorporated in the theory. The peak location is at $\log q = -1.28$. When comparing the peak location with the experimental data, I_2 is approximately one order of magnitude larger for the peak. This discrepancy is consistent with the last two sets of experiments.

In conclusion, the shape of the experimental curves are found to be similar to the analytical solution. However, in the experiments, the PCM reflectivity is consistently lower than expected. And the intensity of pump 2 needs to be approximately ten times stronger than the theoretical model predicts to reach the peak reflectivity.

To account for these discrepancies, the absorption coefficient appears to be one of the important factors. With absorption, the phase-conjugate beam is attenuated. Therefore, the PCM reflectivity as defined in equation 4.30 will take smaller values. This accounts for the lower peak reflectivity values measured in the experiments. To account for the discrepancy in the location of the reflectivity peaks, one has to note that the phase conjugate signal is generated by reading with pump 2 the hologram written by the signal and pump 1. If absorption is present, then a larger pump 2 intensity is needed to generate the same phase-conjugate signal intensity by diffraction on the grating. This may explain the shift of curves in figure 4.13 and figure 4.14.

From the experimental data in section 4.5.1, it is seen that the optimum pump ratio for a given set of parameters (for example geometry, absorption coefficient, etc.) is near $\log q \sim -0.3$ to -0.4 . This pump ratio provides maximum phase-conjugate reflectivity through-out the other experiment, as for example in section 4.5.3. One of the possible reasons for the different between the expected results and the measured

result may be due to the fact that power was measured instead of intensity. The power ratio is different from the intensity ratio because the angle α_s of the signal is not the same as α_p of the pumps. Another source of discrepancy is that the interacting beams are plane wave in the theory while beams of gaussian shape were used in the experiments.

4.6 PCM fidelity and stability

In the previous two sections, the ability of the PCM to amplify a beam optically was investigated. The second attribute of a PCM which is essential for iterative image processing is the ability to heal phase distortion. In this section, the ability to cancel phase errors is experimentally investigated. The stability of the PCM is also investigated.

4.6.1 PCM fidelity

The experimental setup is shown in figure 4.15. To demonstrate the phase healing ability of the PCM, a distortion glass was inserted in the optical path between the object on the figure and the PCM. An airforce resolution chart was used as the object. A lens was placed before the crystal to focus the beam into it. Another lens was placed behind the crystal to reimage the distorted image. The phase-conjugate signal was extracted with a beam splitter as shown in figure 4.15. The phase-conjugate signal and the distorted image were recorded on photographic film.

The distorted image and the phase-conjugate image are shown in figures 4.16 a and b respectively. The quality of the phase-conjugate image is good and shows that almost all the phase distortions have been cancelled as the image propagates back through the distorting glass. The phase conjugate image shows a resolution of about 10 *lines/mm*.

While the PCM shows capacity of removing phase errors, it is not without limitations. The first limitation is that only a small interaction area is available due to the

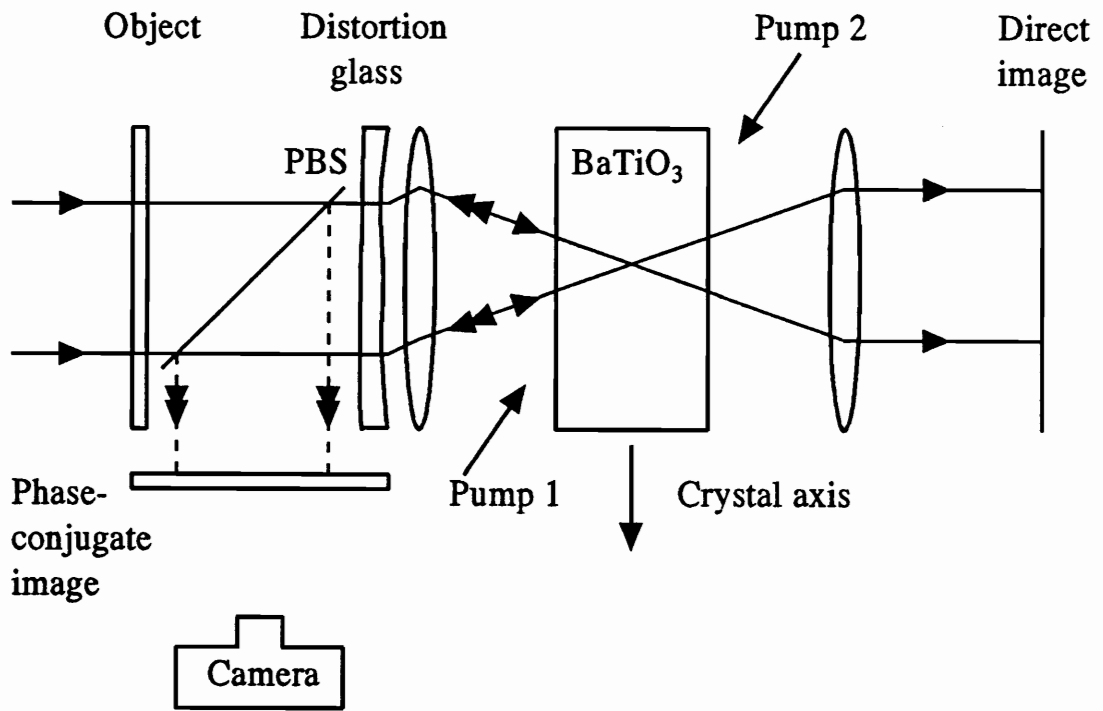
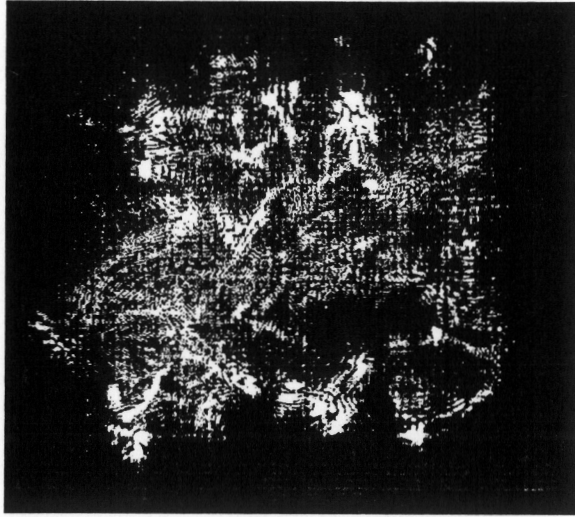
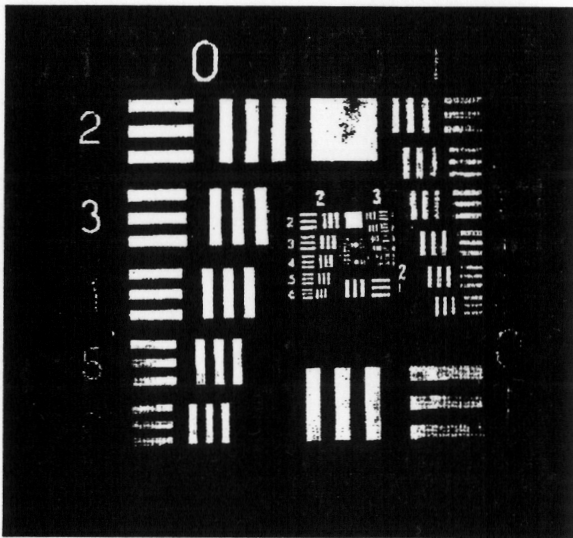


Figure 4.15: Schematic experimental setup for the restoration of phase distortion. A phase distorting glass is placed between the object and the PCM. The pellicle beam splitter (PBS) is placed in between the object and the distorter to extract the phase conjugate image.



(a)



(b)

Figure 4.16: Demonstration of a phase distortion “healing” by a PCM. The size of the image area is 1.5 mm^2 . (a) Distorted image behind the distortion glass. (b) Phase-conjugate image which showing that the phase distortion has been removed.

small size of the crystal. In the theory of chapters two and three, it was assumed that the interaction area on the PCM is infinite and that the reflectivity is uniform over the entire area. In reality, the interaction region is limited by the physical dimension of the crystal. Since BaTiO₃ is hard to grow in large dimension, only crystals of small sizes are available (typically in linear dimensions of 5mm to 10mm). Due to the small size, one has to focus the signal beam into the limited interaction region of the crystal by a lens. If the focal plane of the lens is at the interaction region, only the spatial frequencies within this region are reflected. The rest of the higher spatial frequencies of the signal are lost resulting in a lower quality of the image.

The second limitation is that only the phase distortion can be cancelled. If the distortion contains amplitude attenuation and phase distortion, only the phase distortion is recovered. Therefore, any irregularity and scratches on the surface of the crystal or other optical elements cannot be compensated for.

4.6.2 PCM stability

Another critical aspect for the success of the experiment is that a long term stability for the light source is needed for a slow material such as BaTiO₃ to reach a steady state. Since the phase-conjugate signal travels in the reverse direction of the incident signal beam, some of the light signal will re-enter the laser source and interfere with the beam produced in the laser cavity, inducing intensity fluctuations. To avoid fluctuations of the laser caused by this external feedback, a non-reciprocal device called a Faraday isolator should be placed in the optical path. This device will rotate the polarization of light in one direction by 45° when light enters into the device from one side. If light enters from the other side of the device, the polarization will be rotated by 45° more. This makes the polarization of the feedback perpendicular to that of the laser beam and thus it can be blocked by a polarizer. The isolator achieves this rotation by the Faraday effect (see for example [74]). A good Faraday isolator can reach a rejection ratio of 1000:1 between the signal and the feedback.

In the experimental setup, since a Faraday rotator was not available, a neutral

density (ND) filter was used instead. This neutral density filter acts as a loss filter in both the forward and the backward direction and thus reduces the amount of light fed back into the laser. In the forward direction, the laser intensity is attenuated by a factor equal to the transmission coefficient T of the filter. When the phase-conjugate signal goes through the filter in the backward direction, it is again attenuated by the same amount before entering the laser so that the ratio feedback intensity to laser output drops by T^2 .

By trial and error, a ND filter of optical density 1 (intensity transmission coefficient = $T = 0.1$) was used. This was found to be sufficient to stabilize the PCM reflectivity.

4.7 Conclusion

In this chapter, a PCM using degenerate 4WM in photorefractive BaTiO₃ was investigated theoretically and experimentally. The reflectivity of the PCM was optimized with respect to both the geometrical parameters and the interacting beam intensity ratios. The quality of the phase-conjugate image was found to be good and the ability of the PCM to cancel phase distortion was verified. The stability of the phase conjugation was improved by placing a loss filter at the output of the laser source.

Chapter 5

The transient behavior of a PCM cavity

5.1 Introduction

A PCM cavity is a non-linear feedback system in which self-oscillation and chaos in the cavity field have been observed [75]. These features are common to other nonlinear feedback system such as laser oscillators [75, 76, 77]. The self-oscillating output can interfere substantially with the use of a PCM cavity in iterative image processings. The effect on the output of a PCM cavity when it is above the threshold of self-oscillation is shown in section 5.2. Some of the precautions of using the PCM cavity in iterative processing are identified.

Due to the slow response time of the photorefractive PCM, the cavity dynamics can be easily observed. This study shows some interesting phenomena in a PCM cavity. For example, the cavity shows a critical slowing down of the cavity decay time near the transition to self oscillation. The experimental results are presented in section 5.3.

5.2 Effect on the output image quality when the PCM cavity is above the threshold of self-oscillation

Self-oscillation in a PCM cavity is defined as a state in which a finite output exists without an external input signal. In other words, a PCM cavity above threshold will start resonance oscillation just like a laser cavity. The threshold condition in a PCM cavity is obtained when the gain from the PCM compensates the losses in the end mirror and intra-cavity optical elements. In terms of the feedback parameter β (defined in chapter two), this condition implies that $|\beta| = 1$. This section experimentally investigates the effect of self-oscillation on the input image in a PCM cavity when it is above threshold.

The schematic diagram of the experimental setup is shown in figure 5.1. The reflectivity of the dielectric mirror was 95%, and the steady-state PCM reflectivity was about three. The high PCM reflectivity ensures that the cavity is above threshold initially when the mirror is aligned with the optical axis. The PCM reflectivity was measured with the dielectric mirror tilted farther off the optical axis so that the signal is only reflected once from the PCM.

An airforce resolution chart was used as the input image to the cavity, and the phase conjugate image was extracted from the cavity by a pellicle beam splitter. A portion of the phase conjugate image is magnified and is shown in figure 5.2. A time sequence of pictures of the phase conjugate image shows the evolution of the image in a PCM cavity above threshold.

It is seen that the airforce chart image appears momentarily at the beginning. This indicates that the input signal has a faster rise time than other modes inside the cavity. Subsequent pictures show that a random speckle pattern eventually builds up and resonates alone with the input image. The cavity modes (speckle pattern) interfere with the input image and greatly degrade the quality of the input. This time sequence of pictures show that although the input image has a faster build-up time, its field is not large enough to suppress the build up of the other modes when

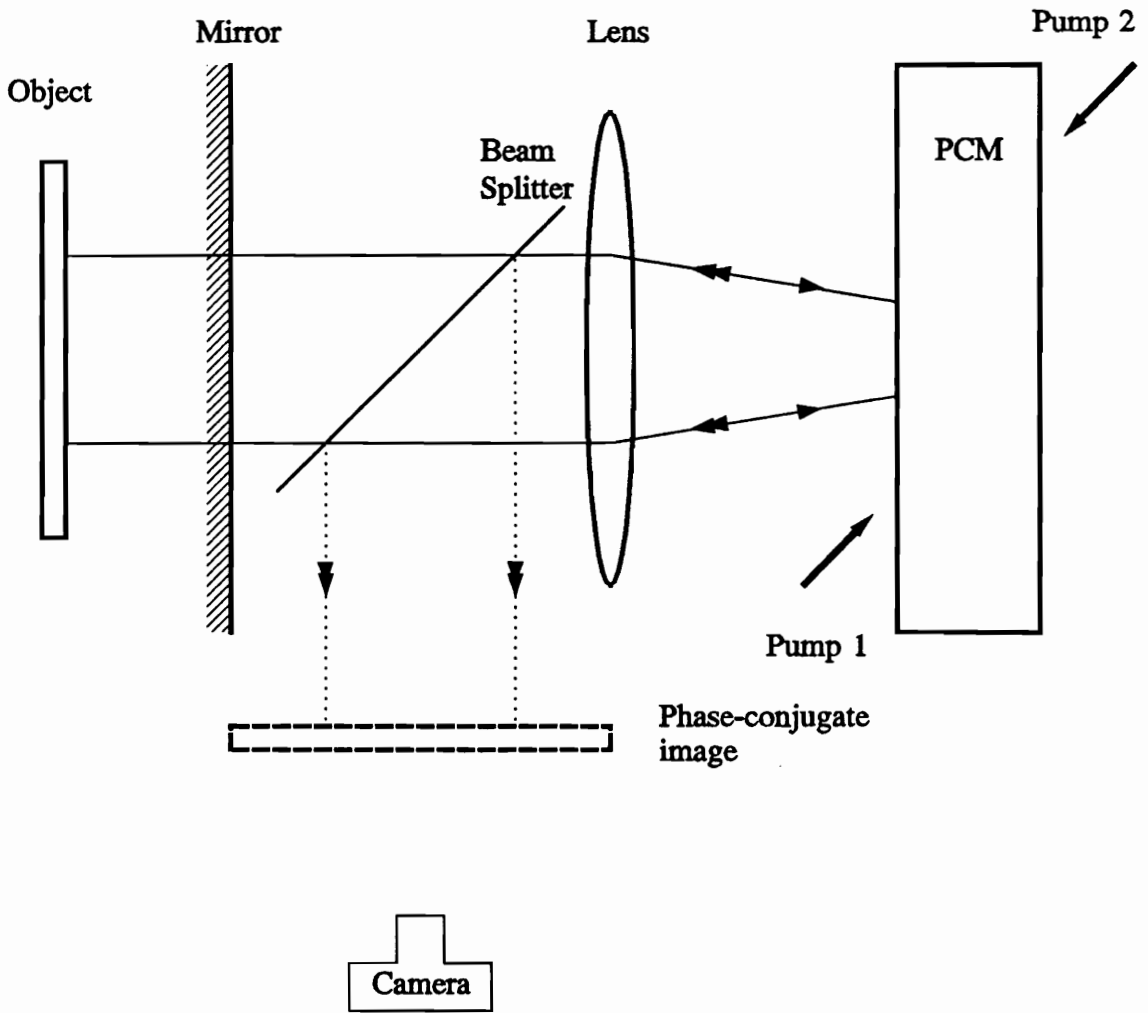


Figure 5.1: Schematic diagram of the experimental setup to observe the effect on the input image when the cavity is above the threshold of self-oscillation.

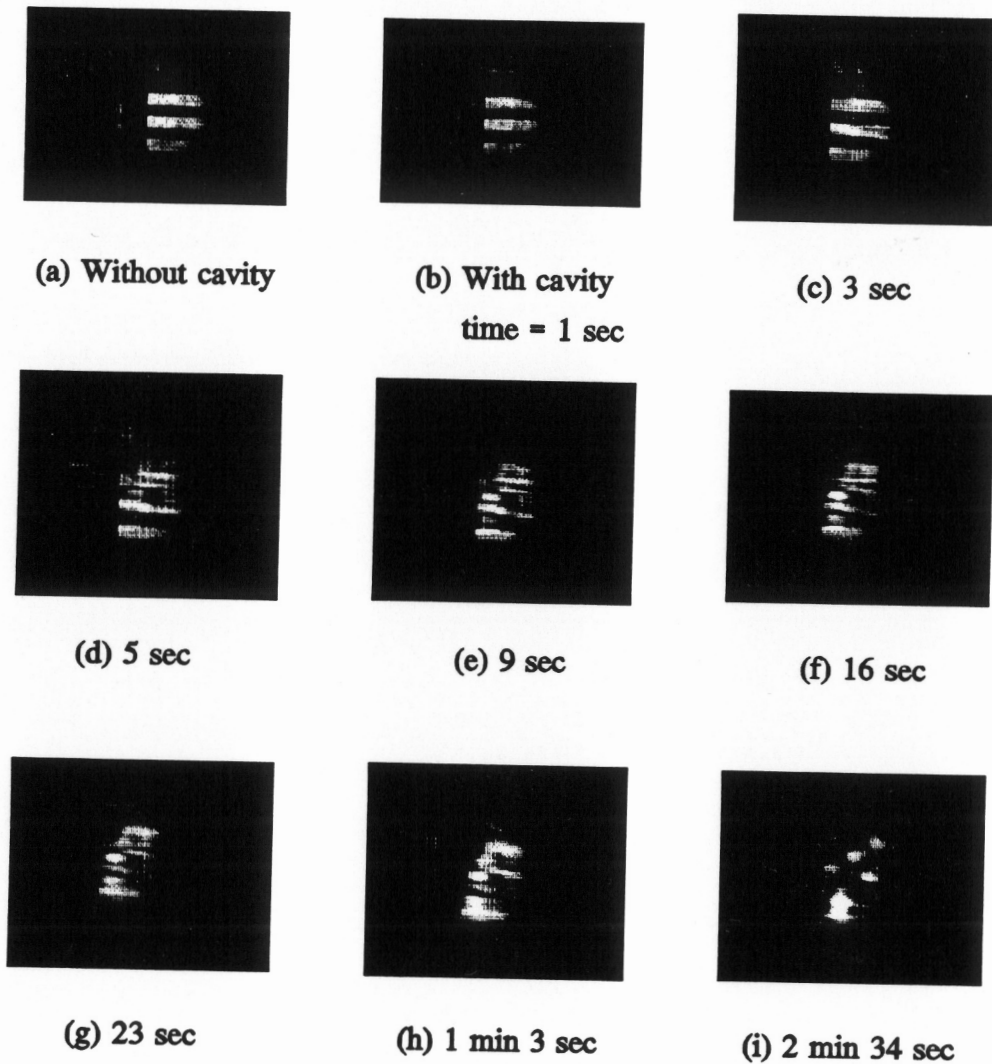


Figure 5.2: Time sequence of evolution of the image in a PCM cavity above threshold. (a) The phase conjugate image without a cavity. (b) With the mirror aligned with the optical axis, the input has been launched into the cavity for 1 second. (c)–(i) Evolution of the input and the build up of the cavity modes (speckle pattern). This time sequence pictures show that a PCM cavity above threshold cannot be used in image processing because the cavity mode greatly distort the input image.

the cavity is above threshold.

In conclusion, the cavity modes greatly distort the input object when the cavity is above threshold. This shows that a PCM cavity cannot be used as an image processing device when it is above threshold.

5.3 Decay time of PCM cavity

The decay time of the cavity is defined to be the time t required for the cavity field to decay to $1/e$ of its value when the input is cut off. It is assumed that the decay curve can be approximated by an exponential function $e^{-t/\tau}$, where τ is the decay time constant.

Examples of the cavity build-up and decay curve when the cavity are above and below the threshold is shown in figure 5.3. The steady-state cavity field intensity is found to increase as the cavity approaches threshold. The transition to self-oscillation is shown to be progressive, and depends on the PCM reflectivity.

The experimental measurements of the decay time constant is shown in figure 5.4. The diverging decay time constant is observed to occur for a log (pumps ratio) between 0.4 and 0.5. In collecting these data, the backward propagating pump I_2 was fixed at a power of $1.66mW$, while the power of the forward propagating pump I_1 varies to change the pumps ratio. The change in pumps ratio alters the reflectivity of the PCM and varies how close the cavity is to the threshold condition. The incident angles of the signal and pump were $\theta_s = 1.5^\circ$ and $\theta_p = 40.5^\circ$ respectively.

The increase in the decay time as one approaches threshold can be understood qualitatively in the following way. The signal field that induces the grating at location 1 (refer to figure 2.1) inside the PCM consists of a part from the input field and the other part from the feedback field at location 2. As the input is cut off from the cavity, the signal field that induces the grating at location 1 comes from the field at location 2 only. Without the feedback, the gratings at both these locations are washed out by the pumps. With feedback, these gratings are sustained by their mutual feedback.

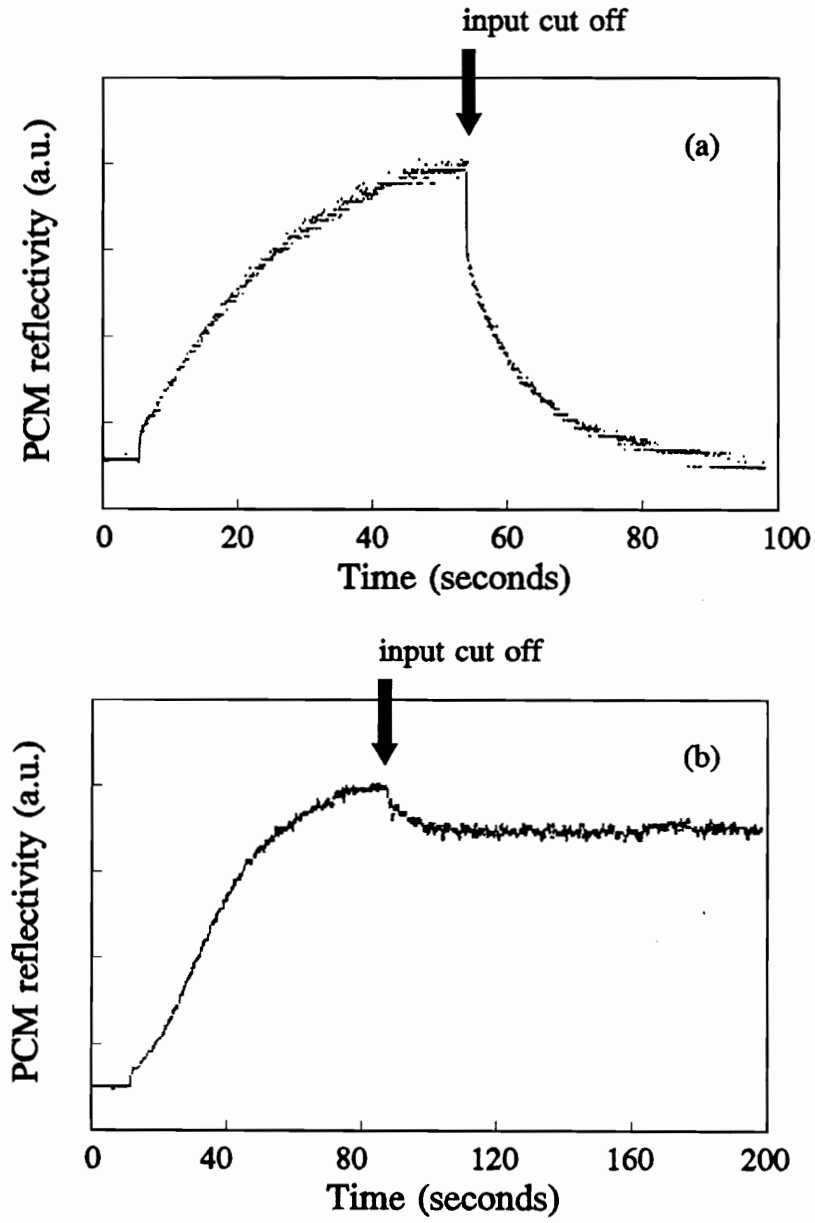


Figure 5.3: Typical rise and decay of the cavity field in a PCM cavity. In (a), the cavity is below threshold, the final field drops to zero after the input is cut off. In (b), the cavity is above threshold.

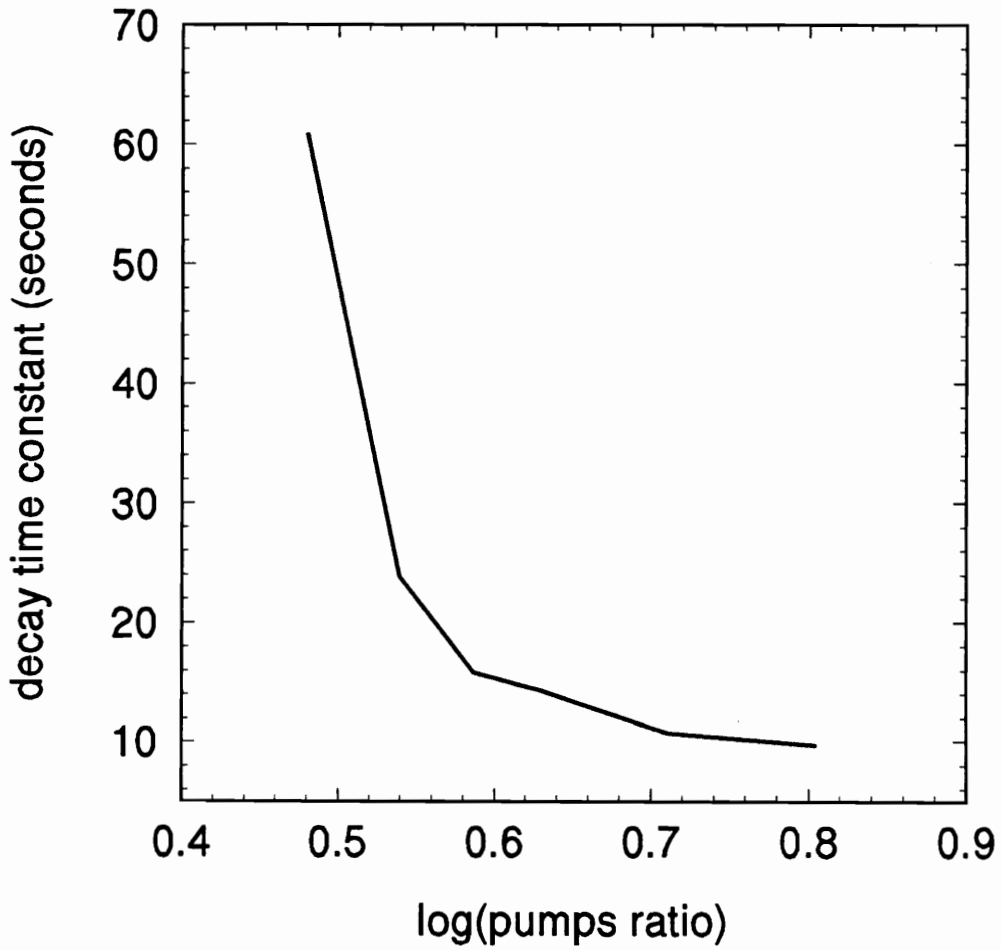


Figure 5.4: Experimental measurement of the decay time constant in a PCM cavity versus the log of pumps ratio. The reflectivity of the PCM is increasing when the pumps ratio is smaller.

When the cavity is close to threshold, the feedback is strong enough to sustain the gratings for a longer period of time. Therefore, the decay time constant is lengthened.

One can also understand the lengthening of the decay time constant through the concept of the resonance of an eigenmode inside the cavity. An ideal PCM cavity without noise supports any input transverse field as a resonant eigenmode. Near threshold, the input mode is near resonance, corresponding to a stronger cavity field which takes a longer time to decay.

The effect of this increase in the time constant may sometimes be found useful. A two-PCM cavity has been suggested to be used as an optical image storage device [78]. This feature does not affect the usage of the PCM cavity as an image processing device, since the output of the cavity is recorded once steady state is reached while the input is being launched into the cavity continuously.

5.4 Conclusion

In conclusion, the threshold of the self-oscillation is reached when the PCM gain compensates the cavity losses. If a PCM cavity is to be used in image processing, it has to be operated below threshold. This conclusion is clear from the results of section 5.2 which show how self-oscillations affect the quality of the image.

It is also found that the decay time of a PCM cavity diverges as the cavity approaches threshold. The lengthening of the decay time constant may be used as an indicator of whether the cavity is above threshold.

Chapter 6

Image resolution enhancement/ extrapolation : an example of the use of a cavity with a PCM in iterative processing

In this chapter, an image resolution enhancement/extrapolation algorithm is optically implemented using a cavity with one PCM. The restoration algorithm is based on the Gerchberg algorithm which uses iterations to recover an object from the band-limited image collected (see chapter 3 for a detailed theoretical description).

There are several reasons for implementing this algorithm rather than other restoration algorithms. First, this optical implementation can serve as a test of whether iterative algorithms can be implemented in a PCM cavity. The fact that the algorithm requires iterations to achieve enhancement provides a factor to determine whether iterations have been performed. If an enhancement of the distorted image is observed, then one knows that iterative processing has been performed. Second, this algorithm is suitable to be implemented in a PCM cavity because it only requires truncation op-

erations (spatial and spatial frequency truncations) which do not require phase filters and thus are not limited by the characteristics of the cavity (section 2.3). Third, the algorithm can be implemented conveniently because of the intrinsic positive feedback of the cavity. There is no need for tuning the phase of the feedback parameter in a cavity which uses four-wave mixing in photorefractive materials as the PCM. In the most usual experimental configuration for optical phase conjugation using photorefractive BaTiO₃, the primary and secondary paths share the same optical pumps inside the crystal so that the cavity automatically provides a positive feedback. This can be understood by noticing that the sharing of the same pumps means that $\text{ARG}[r_{pcm1}] = \text{ARG}[r_{pcm2}]$ (equation 2.10), which means that the feedback parameter β is real and the cavity provides a positive feedback. The intrinsic positive feedback of the cavity enhances the ease of the optical implementation of the Gerchberg algorithm because a positive feedback is required by the algorithm. It also means that the tuning and the determination of the phase of the feedback is not required in such a cavity configuration.

In section 6.1 the components of the optical implementation are described. The actual experimental setup and the results are described in section 6.2. Finally, section 6.3 contains the discussion of the results.

6.1 Experimental setup

6.1.1 General description

Figure 6.1 is a block diagram of the experiment which implements the Gerchberg algorithm. It consists of a unit which produces a suitable input to the system, the PCM cavity with optical elements representing some operators in the forward and feedback branches, an observation and recording port, and a forward output port to measure the forward amplification of the image. The forward output is needed to observe and determine when the steady-state of the cavity is reached.

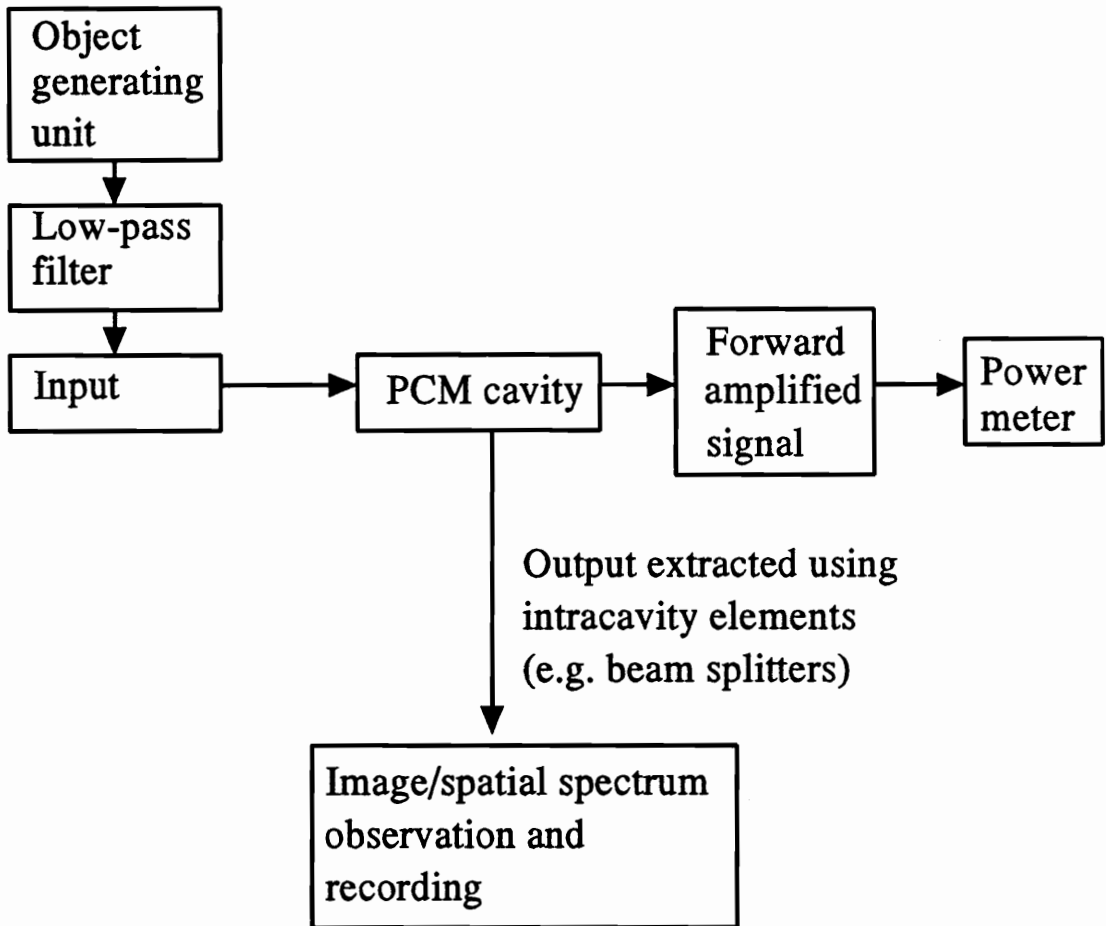


Figure 6.1: Block diagram of the experimental setup. The object generating unit produces an input object to be used for processing. The low-pass filter degrades the object. The restored output and its power spectrum are extracted using intra-cavity elements (beam splitters). A power meter at the output of the PCM cavity measures the forward amplification of the PCM cavity to determine when the steady-state of a PCM cavity is reached.

6.1.2 Object generation

Very simple objects were used in the experiment. They were generated using a combination of grating, cylindrical or spherical lens, and a slit. These objects are either line objects with two or three lines, or point objects with two or three points. a line object (one-dimensional) can be easily generated by a combination of a cylindrical lens, a grating and a slit as shown in figure 6.2. Without the grating, the cylindrical lens focuses a plane wave to a line. To produce several lines, a grating is inserted between the cylindrical lens and the slit, which diffracts the focusing beam onto the slit. The separation y between the lines is given by (small angles)

$$y \simeq \frac{\lambda d}{a}, \text{ for } a \gg \lambda, \quad (6.1)$$

where λ is the wavelength of the laser source, d is the separation between the grating and the slit, and a is the line spacing of the grating. The line separation is adjusted by varying d . The slit S_1 selects the number of lines used in the experiment.

Point objects are generated using the same technique with the cylindrical lens replaced by a spherical lens. The separation of the points is, again, given by equation 6.1.

6.1.3 Low-pass filter

The low-pass operation is achieved by using a spherical lens and a slit (in our case, a slit mirror M) in the spatial frequency plane of the object. The object, which is on the slit S_1 (figure 6.2) plane, is placed at the front focal plane of the spherical lens. This optical configuration accomplishes a two-dimensional Fourier transform of the object [39]. At the back-focal plane of the spherical lens, spatial frequencies f_x, f_y of the object are defined as

$$f_x = \frac{x_\xi}{\lambda f} ; \quad f_y = \frac{y_\xi}{\lambda f}, \quad (6.2)$$

where (x_ξ, y_ξ) are the co-ordinates at the mirror plane, and f is the focal length of the spherical lens. If a spatial frequency filter (a slit) is placed at this plane to select

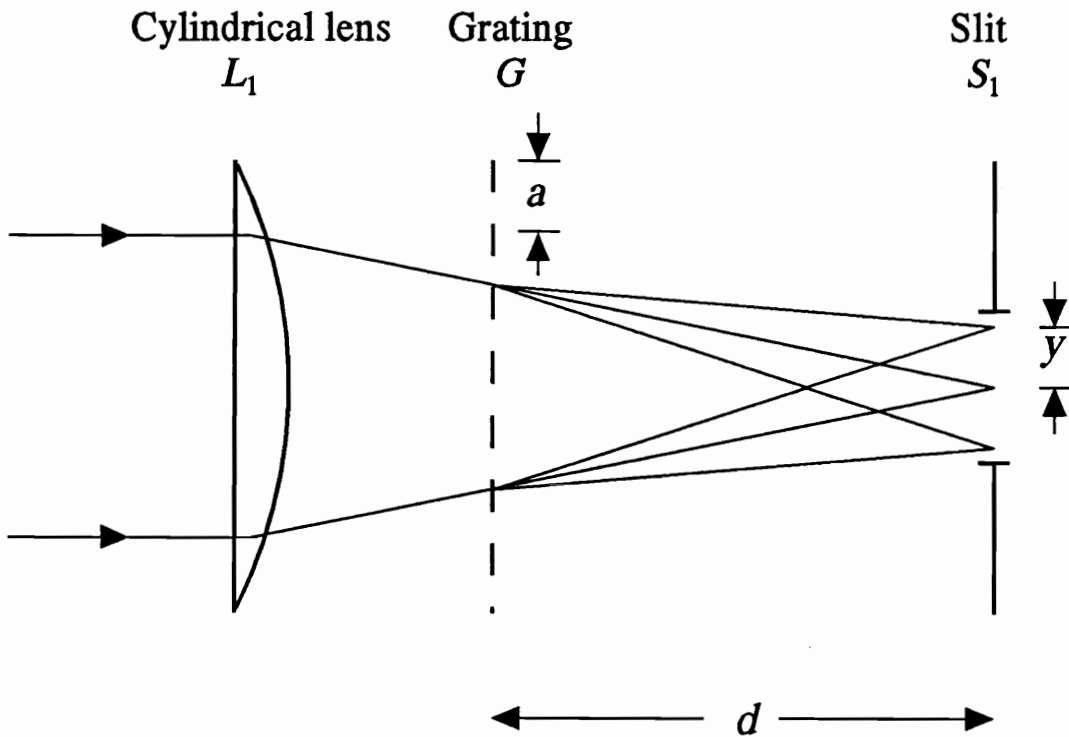


Figure 6.2: Diagram of the setup used to generate objects consisting of several lines. A cylindrical lens is used to focus a plane wave into a line. Several lines are generated by inserting a ronchi grating of 100 *lines/inch* between the lens and the slit. The separation of the lines is determined by the distance between the grating and the slit. The opening of the slit selects the numbers of lines.

a particular set of frequencies, a low-pass or band-pass operation is accomplished. If the opening $t(x_\xi, y_\xi)$ of the slit is given by

$$t(x_\xi, y_\xi) = \begin{cases} 1 & , \text{if } |x_\xi| \leq \sigma , \\ 0 & , \text{otherwise,} \end{cases} \quad (6.3)$$

then the slit represents a low-pass operation of cutoff spatial frequency $\frac{\sigma}{2\lambda f}$ line/mm along the x -direction.

6.1.4 The PCM cavity

Figure 6.3 shows a schematic diagram of the setup for the PCM cavity that implements the Gerchberg algorithm. The input mirror has a transparent slit in it, representing a low-pass filter \hat{T}_B . In the feedback loop, the slit mirror also serves as the complementary high-pass filter which is required by the algorithm. A slit adjusted to the size of the object and representing the truncation \hat{T}_D is placed in the back-focal plane of L_3 . Since both the primary and the secondary paths pass through the slit, the secondary path contains an additional operator \hat{T}_D . This contrasts with figure 3.10 where only the primary path contains \hat{T}_D , and no operation is performed in the secondary path.

Since the opening representing the truncation operator \hat{T}_D is symmetrical, we have $\hat{\mathcal{F}}\hat{T}_D\hat{\mathcal{F}}^{-1} = \hat{\mathcal{F}}^{-1}\hat{T}_D\hat{\mathcal{F}}$, and the output E_o , using the notation and symbols defined in section 3.3.5, can be written as

$$E_o = \tau E_i + \beta \{ \hat{T}_D \hat{\mathcal{F}} [\hat{I} - \hat{T}_B] \hat{\mathcal{F}}^{-1} \}^2 E_o , \quad (6.4)$$

where $\beta = |r|^2 r_{pcm1}^* r_{pcm2}$ as before.

On expanding E_o and E_i in a complete set of eigenfunctions $\{\phi_k\}$ of the operator $\hat{\mathcal{G}} = \hat{T}_D \hat{\mathcal{F}} [\hat{I} - \hat{T}_B] \hat{\mathcal{F}}^{-1}$ as in section 3.3.5, one can relate the k th coefficient of expansion of the output to that of the input by

$$\begin{aligned} e_{ok} &= \frac{1}{1 - \beta(1 - \lambda_k)^2} \tau e_{ik} \\ &\simeq \frac{1}{\lambda_k(2 - \lambda_k)} \tau e_{ik} , \quad \text{for } \beta \rightarrow 1 \text{ and SIGN } [\beta] = 1 \end{aligned} \quad (6.5)$$

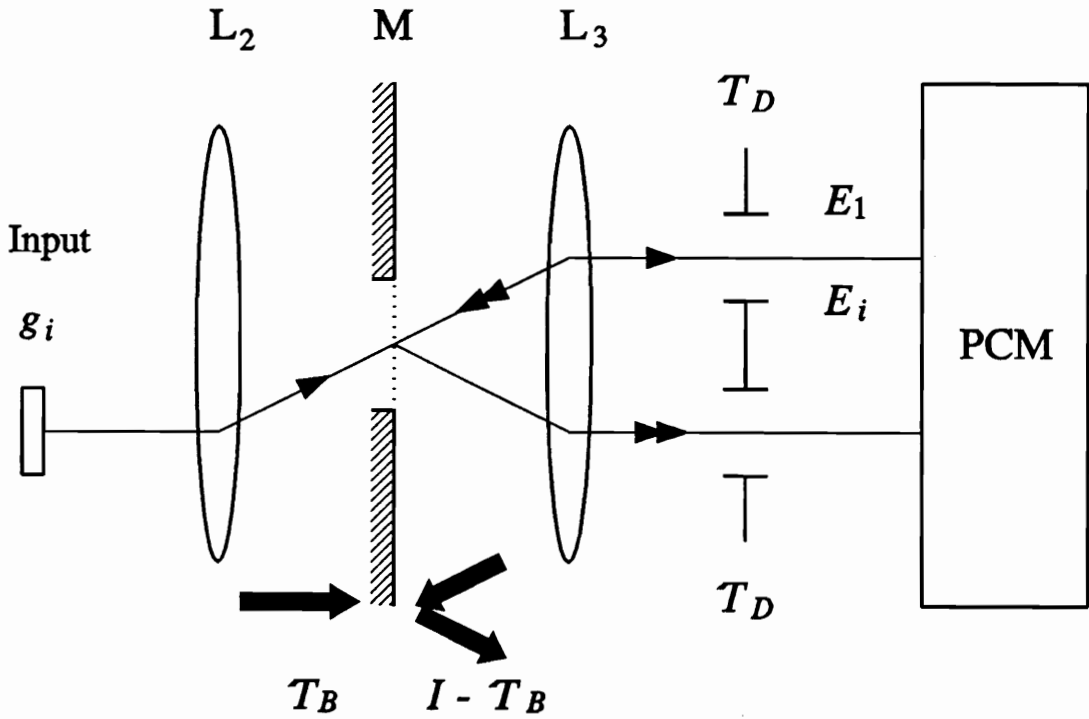


Figure 6.3: Schematic diagram of the optical cavity used to implement the Gerchberg algorithm. This diagram is similar to figure 3.10 except that the secondary path has an additional slit which represents one more truncation operation in the spatial domain in the feedback loop.

It is interesting to note that the contributions of the eigenfunctions corresponding to large eigenvalues ($\lambda \simeq 1$) are approximately the same as in an inverse filter, while the contributions of small eigenvalues ($\lambda \ll 1$) are attenuated by a factor of two when compared with their contributions in an inverse filter. This could be interpreted as some kind of regularization (a reduction of sensitivity to noise).

6.1.5 Observation and recording of the image

There are two outputs for the cavity, output ports 1 and 2. They are extracted from the cavity using two pellicle beam splitters PBS_1 and PBS_2 (figure 6.5). Output port 1 is used to observe the extrapolated spectrum on mirror M. Output port 2 is used to observe the distorted and the restored object. Film was used to record the intensity distribution of the images and their spectra. In recording the distorted and the restored objects, both images were recorded on the same roll of film to insure that these data were recorded with the same contrast. Kodak T-max 100 film with D-76 developer was used in the experiments. A standard developing procedure was closely followed to ensure constant density and contrast of different rolls of film.

The procedure to convert the density of the film back to an intensity scale is described below. A step wedge target of known optical density (O.D.) from O.D.=0.3 to O.D.=3 in ten steps is photographed using back-lighting. This produces an optical density variation on the developed film which was measured. This was used as a look-up table to convert the density on the film back to an intensity scale.

Figure 6.4 is a plot of the optical density of the film T-max versus the input intensity. The solid line represents a third-order polynomial curve fitting result. Note that the film density saturates at some larger intensity. In the experiment, different exposures of the same image are taken to insure that a properly exposed picture is obtained. In the case where point objects are used, which is likely to result in an image with a dynamic range larger than the response of the film, a cylindrical lens is used to spread out the object spatially in the vertical direction so that proper exposure can be obtained. Therefore, the film records of the objects are always in a

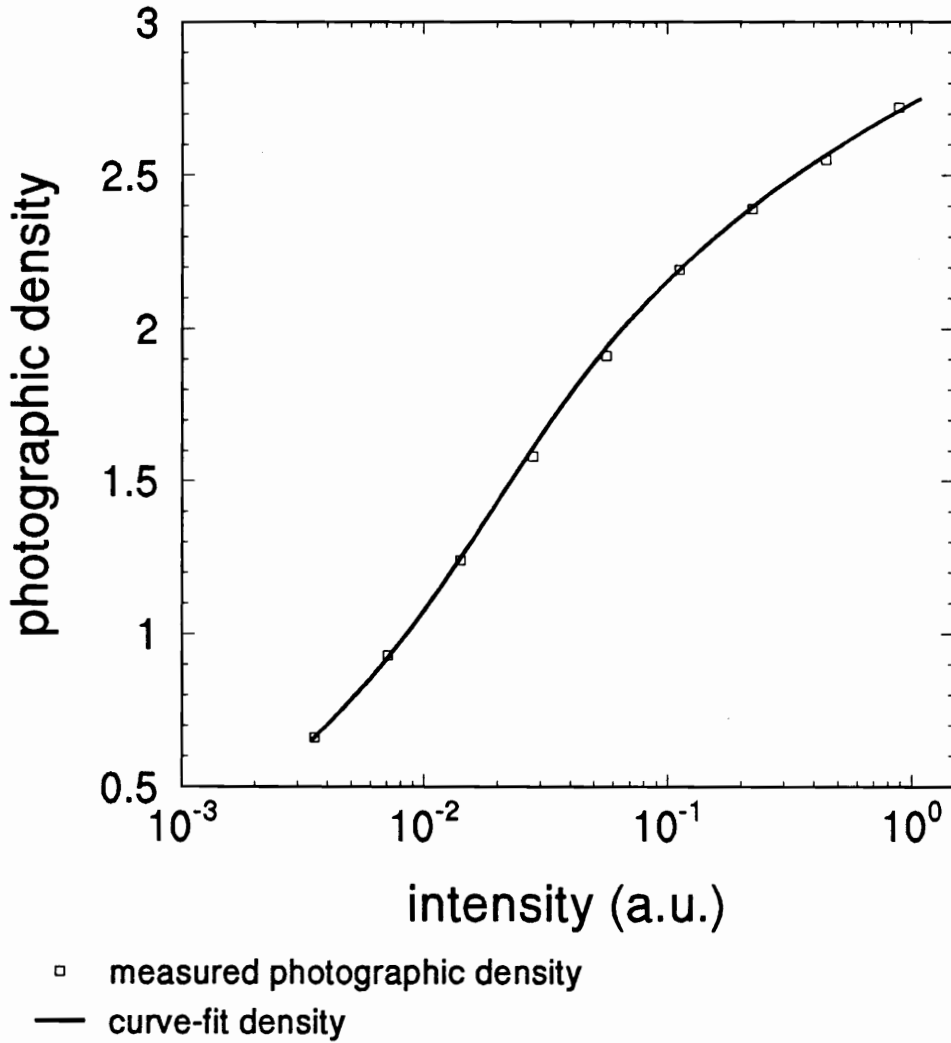


Figure 6.4: Plot the photographic density versus input intensity for T-max film developed in Kodak D-76 developer. The solid line is a third-order polynomial curve fitting result, which serves as a look-up table to translate the recorded density back to the image intensity distribution.

one-dimensional spread-out format regardless of whether the object is a line or point object.

In the process of converting the density of the film back to intensity, a microdensitometer from Elmer-Perkin was used to scan the density of the film. The film is scanned in two dimensions. The vertical dimension is averaged to obtain the intensity in one dimension.

6.2 Experimental results

The experimental setup is shown in figure 6.5 which lumps together the components described in the last section. The PCM in the setup of figure 6.5 is an externally pumped single crystal of BaTiO_3 ($5 \times 5 \times 6 \text{mm}$ from Sanders) in a degenerate four-wave mixing configuration as described in chapter 4. The laser is a single mode Argon laser from Coherent operating at 514nm . The incident angle between the pump beam and the signal beam with the crystal normal were $\theta_p = 47.5^\circ$ and $\theta_s = 15.8^\circ$, respectively (these incident angles were measured in air, at the air-crystal interface). Polarization was extraordinary for all the beams. The pump beams had powers of the order of $26 \mu\text{W}$ for I_1 and $14 \mu\text{W}$ for I_2 . The pump beam diameters were about 1mm in the crystal. The signal-beam power was of the order of 20nW . With these parameters, a PCM reflectivity of about 1.7 was achieved. In the experiments, the reflectivity was adjusted to bring the cavity close to but not above threshold. This condition of course depends on the losses introduced by the various intra-cavity elements (pellicle beam splitters, mirror M, lenses).

The lenses L_2 and L_3 had 16mm focal lengths which provided a 1:1 imaging of the data and of the slit S_1 onto the truncation slit \hat{T}_D which was 0.11mm wide. The adjustment of the size of the slit S_2 was done (with M removed) by placing a mirror behind the slit and looking at slits S_1 and S_2 at the same time through a microscope. This provides a means to match the size and orientation of the two slits. After the alignment, mirror M is re-inserted into the spatial frequency plane of the input. The

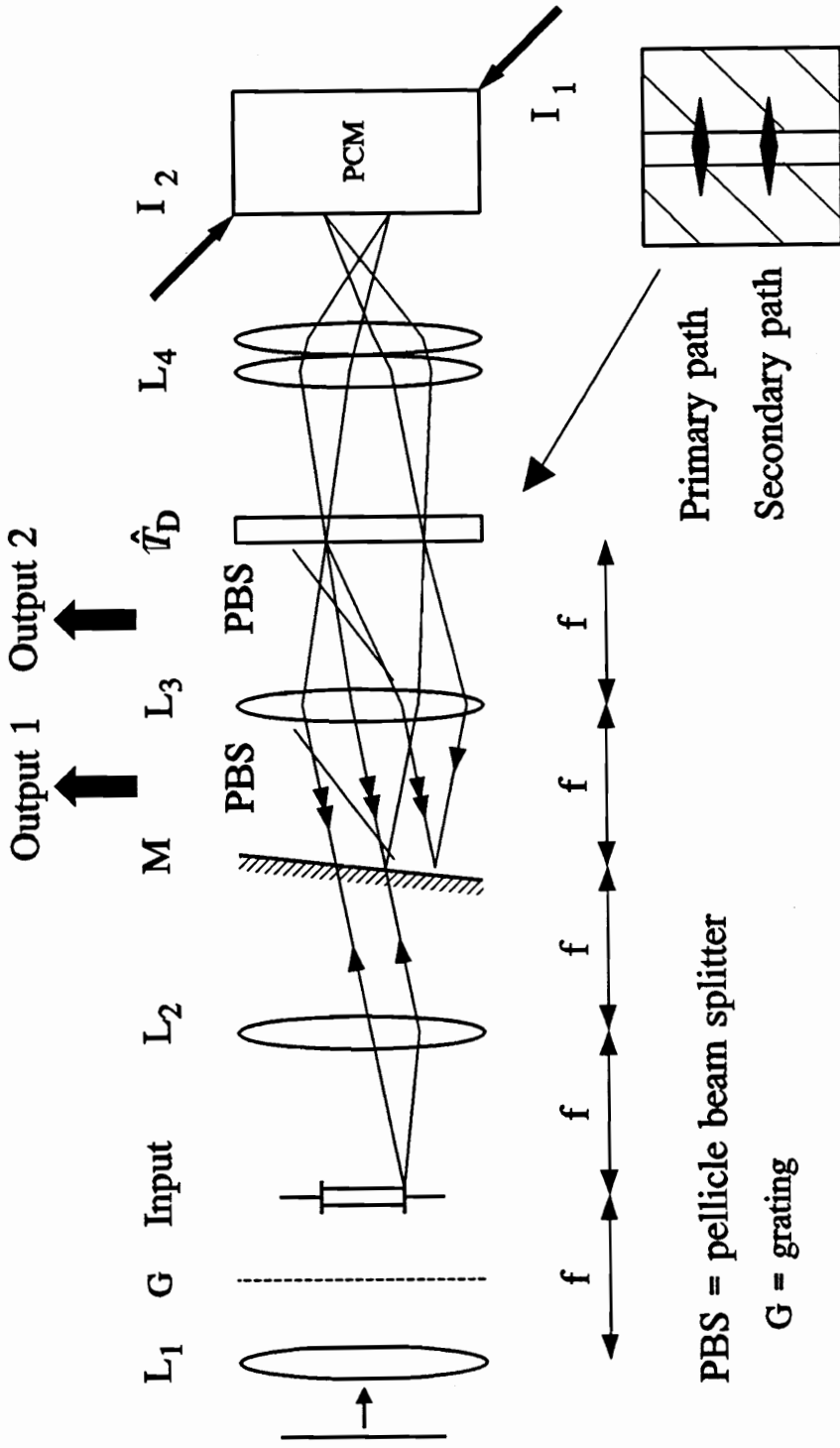


Figure 6.5: Setup used for the experimental implementation of the Gerchberg algorithm. Phase conjugation is achieved by degenerate four-wave mixing in a single crystal of BaTiO₃. The mirror M is slightly tilted to separate the primary and the secondary path. Output ports 1 and 2 extract the extrapolated spatial frequency information and the enhanced spatial output, respectively.

slit in the input mirror had an opening of 1.21mm which acted as a low-pass filter with a cutoff spatial frequency of about 7.4 lines/mm . The truncation slit was re-imaged onto the PCM with additional lenses L_4 .

The main reason for using a line input is to provide for two well separated paths in the cavity while still using a small interaction region in the crystal.

Figure 6.6 shows some results for an input consisting of two sharp points. Both input and output data were recorded on the same roll of film and with the same exposure time, ensuring that both data sets were recorded with the same contrast. The visibility V of the peaks is defined by [74]

$$V = \frac{I_{max} - I_{min}}{I_{max} + I_{min}}, \quad (6.6)$$

where I_{max} is the maximum intensity of the spot on the left and I_{min} is the minimum intensity between the two spots. Figure 6.6 shows an improvement of visibility of the two peaks by a factor of about 30% (from a value of 0.6 in the input to a value of 0.8 in the output). A three-point object did not show a noticeable difference in the visibility using similar set-up.

Figure 6.7 shows a trace through the extrapolated spectrum which for a two-peak object should resemble a cosine function. Figure 6.7 shows that the part of the low-pass spectrum which with a sharp cutting edge, and the part of the extrapolated spectrum. The extrapolated spectrum shows a drop in intensity near the edges of the low-pass spectrum. This is because these edges of the slit in the input mirror were not perfectly sharp because of the way it was evaporated, thus providing little feedback in these regions of the mirror. The extrapolation becomes increasingly noisy, as expected, as one extends further toward higher spatial frequencies.

In a one-path geometry, the characteristics of the cavity impose a restriction on the type of objects that can be used (section 2.3.1). The restriction is that the object must satisfy the condition $E(x, y) = E^*(-x, -y)$. In a one-dimensional case, this restriction implies that the object has to be symmetrical. To demonstrate the restoration of a symmetrical object in a cavity with one-path geometry, a nearly symmetrical object is used (a power meter has to be used to determine the intensity

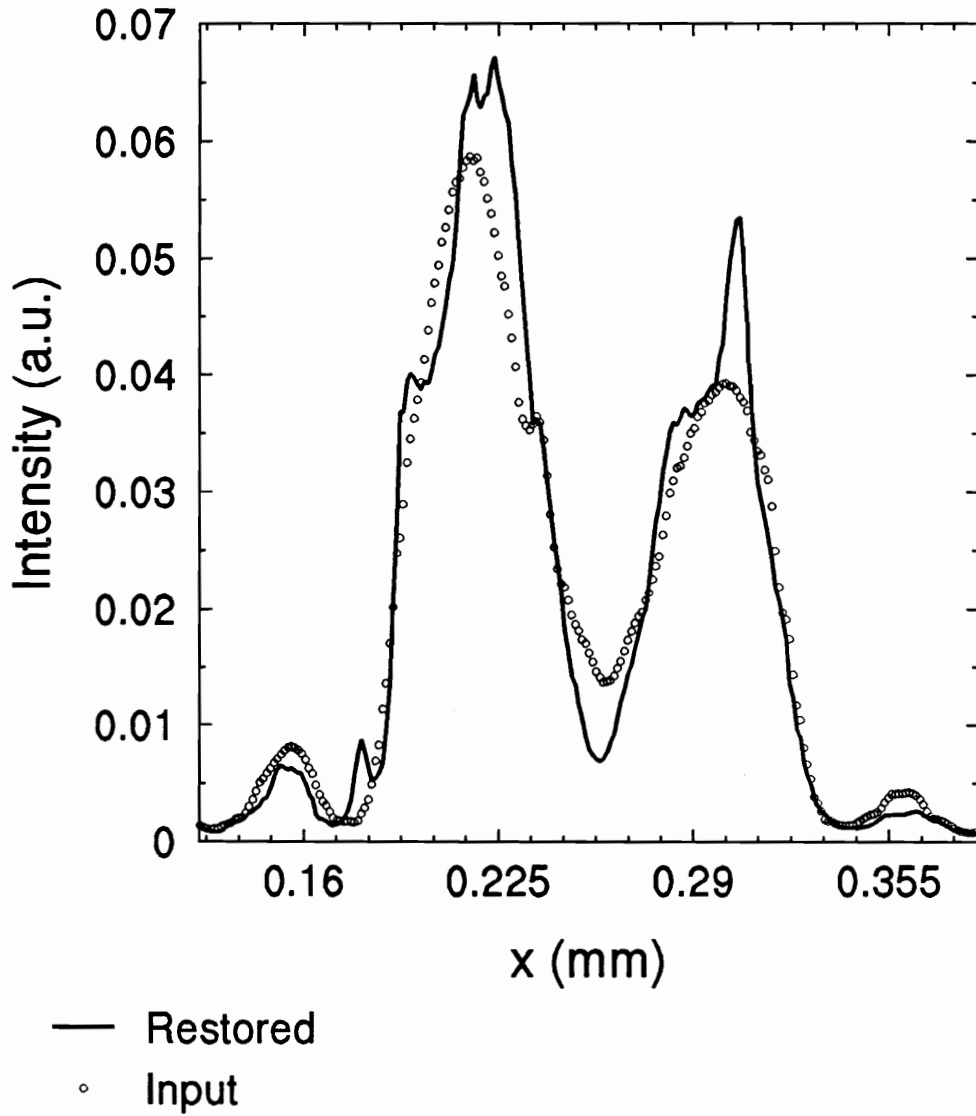


Figure 6.6: Trace through the intensity distribution of the degraded image of a two-pixel input (dotted line), and through that of the restored image (solid line). The restored image shows a 30% improvement in visibility.

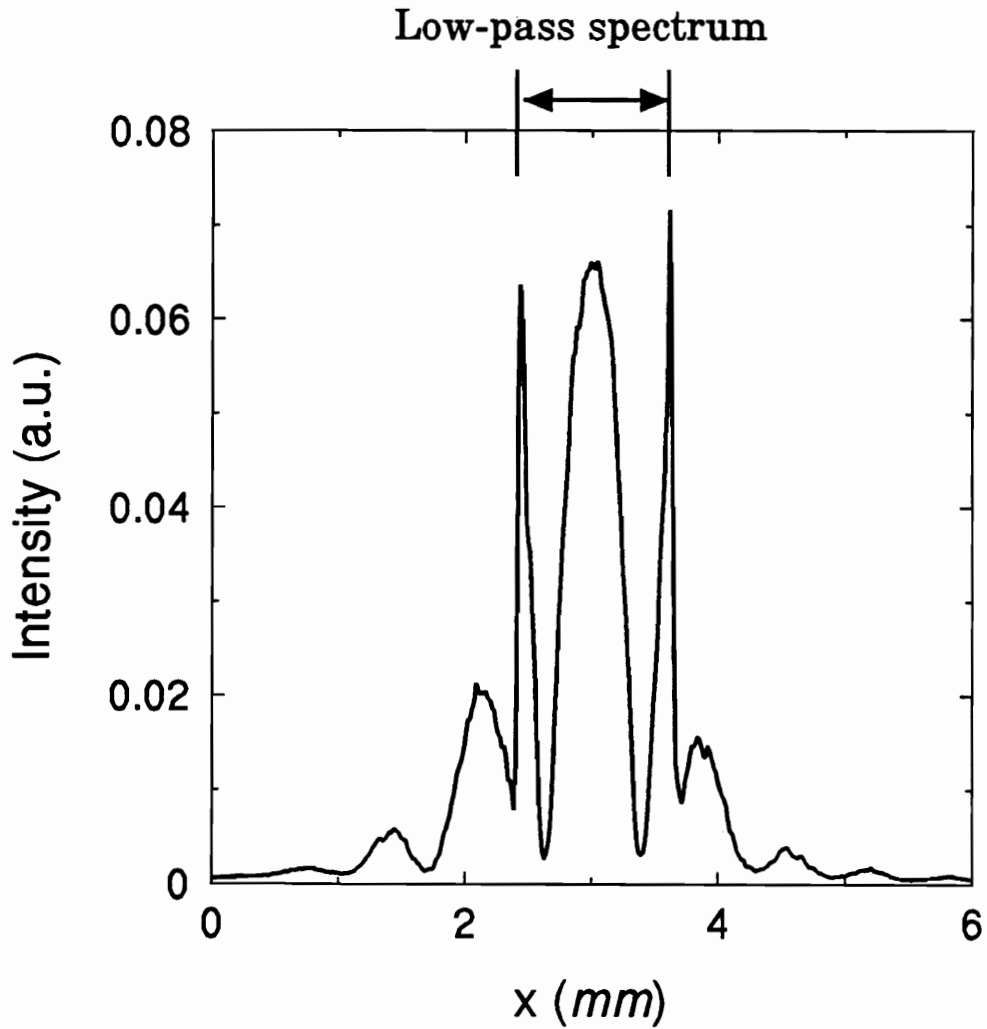


Figure 6.7: Output at port 1 showing the extrapolated spatial frequency spectrum. The center portion is the input spectrum. The low intensity at the boundary of the band-limiting slit are due to the soft edges of the mirror leading to low gain in these regions.

of these peaks). The object consists of two sharp points which have been low-passed with the slit mirror. To achieve a one-path geometry, the mirror M is aligned normal to the optical axis so that the primary path overlaps with the secondary path in figure 2.1. Figure 6.8 shows a trace through the object and the restored object. The output shows an improvement of visibility of about 140% in spite of an obvious departure from the required symmetry. The humps on the left of the restored-object trace are due to diffraction of noise by the slits, which also shows some asymmetry.

Figure 6.9 shows a trace through a three-point object and the corresponding restored object. The visibility of the three points does not show a significant improvement. This experimental result confirms the computer simulation (section 3.3.4) that a more complicated object requires a larger number of iterations than a for simpler object, to achieve the same degree of visibility improvement. Also the effect of noise becomes more critical.

6.3 Discussion

The results shown in the last section may not appear very spectacular. One must keep in mind, however, that the restoration algorithms discussed have very severe fundamental limitations and that their implementation with an analog optical device such as that shown in the last section raises serious technical challenges.

The fundamental limitation comes from the ill-posed nature of the problem (which means that the results of its solution are very sensitive to a change in the initial data). Indeed, even if it is generally agreed that super-resolution and analytic continuation are feasible with noise-free data, the extent to which they are feasible in the presence of noise is debatable. The fact that significant improvement was observed on a two-pixel image but not on a three-pixel image may be due mainly to this limitation. Some authors [79] would even claim that they are not physically realizable at all unless the data contain no more than a single pixel. In this case, of our, one could argue that the problem has shifted from a problem of resolution to that of mere detection. Whatever the conclusion, there is still plenty of room for debate on the subject.

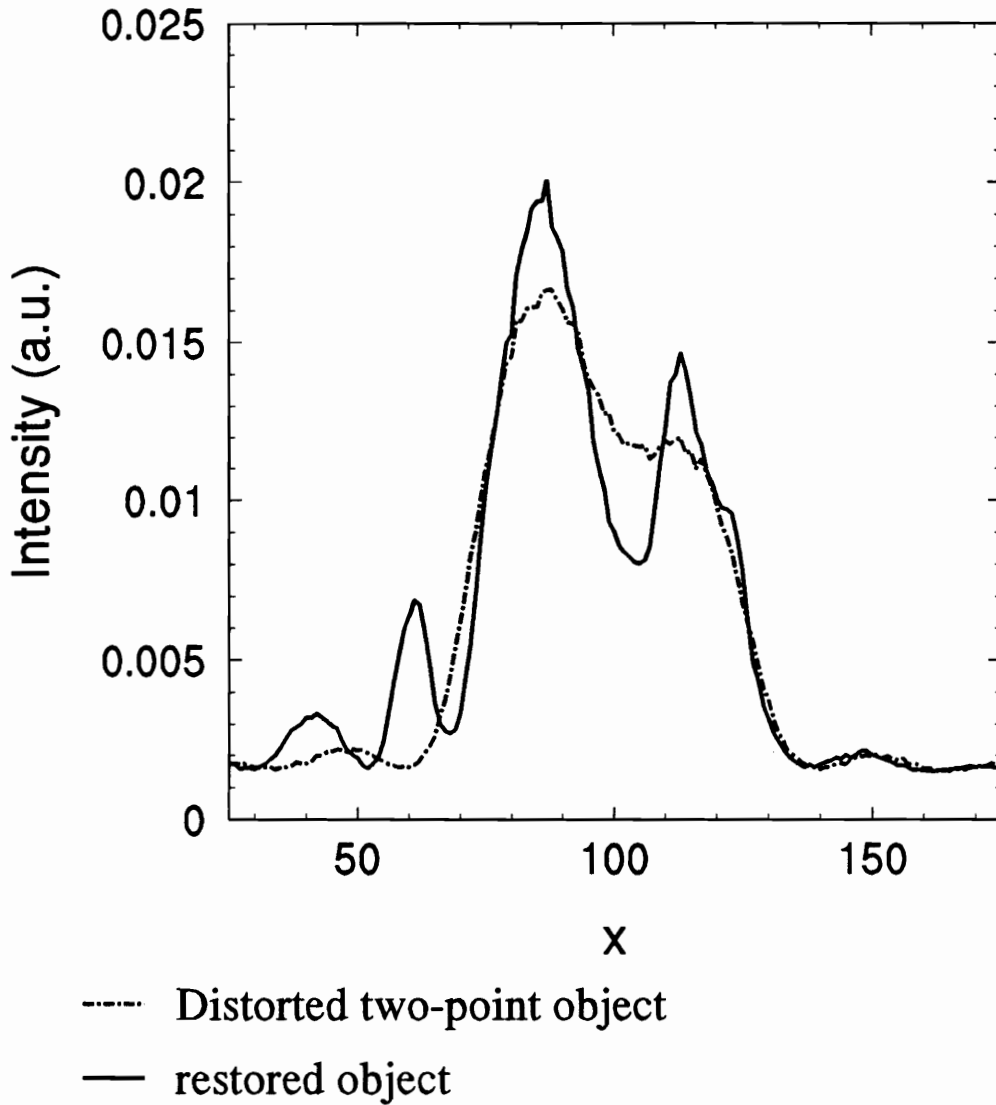


Figure 6.8: Trace through the intensity distribution of the degraded image of a two-pixel input (dotted line), and that of a restored image (solid line) using a one-path geometry. The restored image appears to be better resolved, however this does not necessarily mean that a one-path geometry is more successful than a two-path geometry (see discussion in section 6.3).

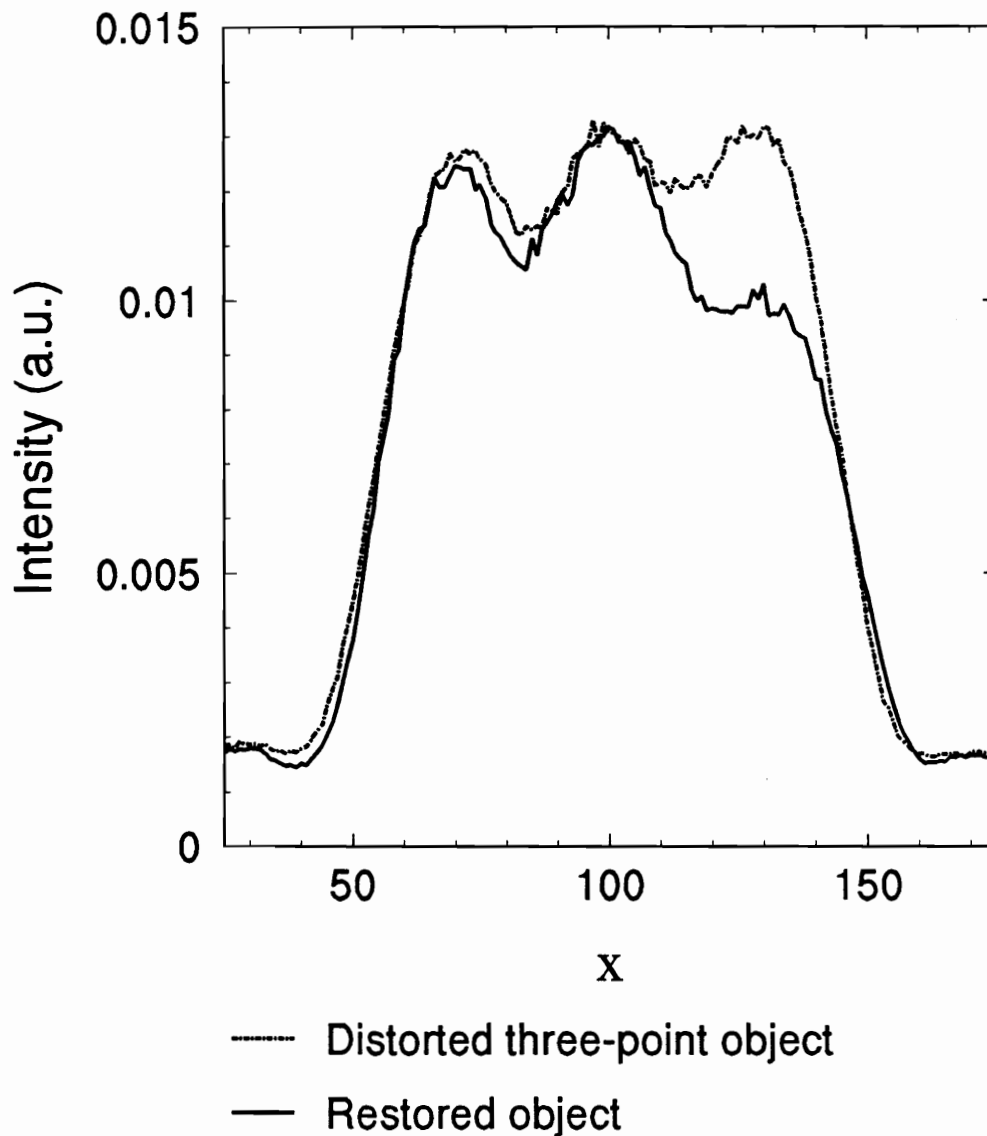


Figure 6.9: Experimental result of the restoration of a three-pixel object using a one-path geometry. The improvement in resolution is not significant. The low intensity in the right pixel of the restored image may be due to the nonuniformity of the PCM reflectivity.

In trying to implement these ill-posed algorithms with analog devices, one must face the fact that noise is unavoidable. Thus, at best, the expectation for spectacular or even just successful results must remain modest.

These are the reasons for choosing the simplest possible object for which the concept of resolution is still meaningful (i.e. a two-pixel object). Experiments with more complicated objects did not lead to reproducible results. This may be due to some fundamental limitations or, more likely, to some technical difficulties such as that of determining the exact phase of the feedback parameter and the limited coherence length of the laser.

A number of experimental challenges had to be faced in the implementation described in section 6.2, the most important one being that one needs a cavity with positive feedback operating close to threshold. This is the most unstable situation for an optical cavity. In our experimental setup, the fact that we used a cavity with photorefractive gain in BaTiO_3 (a slow material, inherently difficult to control) enhanced these difficulties. They showed up in many different ways. For example, when the gain of the PCM is increased to bring the cavity closer to threshold, a critical slowing down is observed (section 5.3).

For reasons probably tied to the above observations, it was also found difficult to maintain the phase of the PCM reflectivity constant over a long period of time. If that phase changes differently for the two paths in the cavity, the phase of the feedback parameter changes, drastically altering the transfer function of the feedback system.

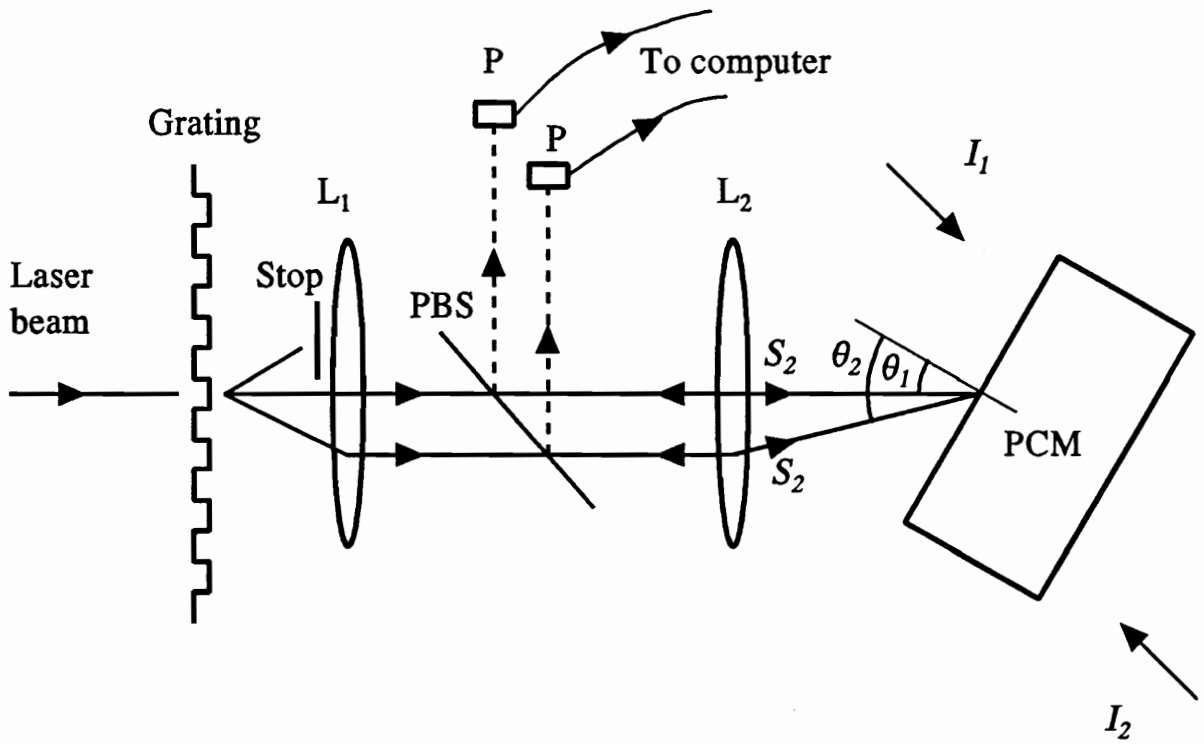
A second technical difficulty is that the laser had a limited coherence length. As had been shown in the computer simulation in section 3.3.4, a very large number of iterations was required to achieve dramatic restoration enhancement, and it took even more iterations for more complicated objects. However, the number of iterations was limited by the coherence length of the laser. To increase the number of iterations, one may shorten the cavity length. However, it is not realistic to hope to achieve the tens of thousands of iterations required to produce a very dramatic improvement for

complicated objects.

A third difficulty is that the edges of the high-pass mirror M were soft and did not reflect much of the information back into the cavity. This information is critical to the success of the algorithm because of the progressive nature of the algorithm. In the algorithm, the output of the next iteration depends upon the result of the last iteration. The soft edges of the mirror added noise into the iteration because they reflect much less light, and the first iteration is mainly from these signals. To narrow the soft edges of the mirror, one may use evaporation methods that produce collimated coating beam (or better masks). Additional analyses are required to determine the exact nature of the influence of the soft edge on restoration.

It was also observed that when the two paths (primary and secondary) share the same interaction region in the photorefractive crystal, a competition takes place. The primary-path beam is usually much stronger than the secondary-path beam which contains the extrapolated data. Independently the weaker beam has a higher reflectivity, as expected. In the presence of the stronger beam, however, the reflectivity of the weaker one drops sizably. This drop of gain for the secondary path indirectly limits the amount of extrapolation achievable.

To understand more about the nature of this competition, an additional experiment, as shown in figure 6.10, was carried out without the cavity mirror. Two signal beams of different intensity were used to simulate the primary-path and the secondary-path beams. These beams were produced by an unexpanded laser beam diffracted from a grating of 100 *lines/mm*. Only the zero-order beam of about $0.96\mu W$ power and one of the first-order beams of $0.5\mu W$ power were selected. These signals were collimated by placing the grating in the front focal plane of lens L_1 , and were re-imaged into the crystal by the lens L_2 . The crystal was located at the back focal plane of L_2 to make sure that they overlapped and shared the same interaction region in the crystal. The strong beam entered into the crystal at an incident angle θ_1 of 14.5° and the weak beam entered at an incident angle θ_2 of 16.0° . The small difference in these incident angles ensured that the phenomenon was not due to a change in the coupling coefficient (section 4.4). The phase-conjugate signals were extracted from



P = Photodetector
 PBS = Pellicle beam splitter

Figure 6.10: Diagram of the setup used to observe the competition of two sets of gratings in the same interaction region of the PCM. A grating is used to generate two signal beams with different intensities. These beams are collimated and then focused inside the crystal by lens L_1 and L_2 , respectively. The phase-conjugate signals are extracted from the cavity by a pellicle beam splitter and are measured by two photodetector connected to a computer for recording.

the beam path by a pellicle beam splitter, and the phase-conjugate reflectivities of these two beams were measured using two different photo-detectors connected to a computer for data acquisition. During the experiment, one of the beams was turned on at the beginning, and when its steady-state reflectivity was reached, the second beam was then turned on. The result of the measurements is shown in figure 6.11.

Figure 6.11(a) shows that when the strong signal beam S_1 is turned on first, the phase-conjugate reflectivity of the weak signal beam S_2 levels out at about 1.6. However, in figure 6.11(b), if the weak signal beam is turned on first, it reaches a reflectivity of about 2.5. When the strong beam is turned on afterward, the reflectivity of the weak beam drops back to 1.6. Other experiments with different strong and weak beam intensity ratios confirmed this behavior. These results show that a strong-signal beam will have a larger phase-conjugate reflectivity than a weak-signal beam when the two beams share the same interaction region, independently of whether the strong grating is initially present in the region or not. Furthermore, the results show that this competition is due to mechanism in the PCM, and not due to the competition of the cavity modes. This phenomenon is likely due to the coupling of the beams inside the crystal. Additional analysis is needed to better understand the physics behind this phenomenon.

These results also provide an insight as to why the results of the restoration in a one-path PCM cavity (figure 6.8) appear to be better than those of a two-path PCM cavity (figure 6.6). In a one-path geometry, the primary path overlaps with the secondary path, and both the images from the primary (inverted) and the secondary (upright) paths superimpose on the input image. Since the primary-path image has the stronger intensity, the presence of the secondary-path image may not be significant. Therefore, the output of the cavity is essentially the overlapping of the input and its inverted image. When using an unsymmetrical object this superposition may result in an apparent improvement of resolution.

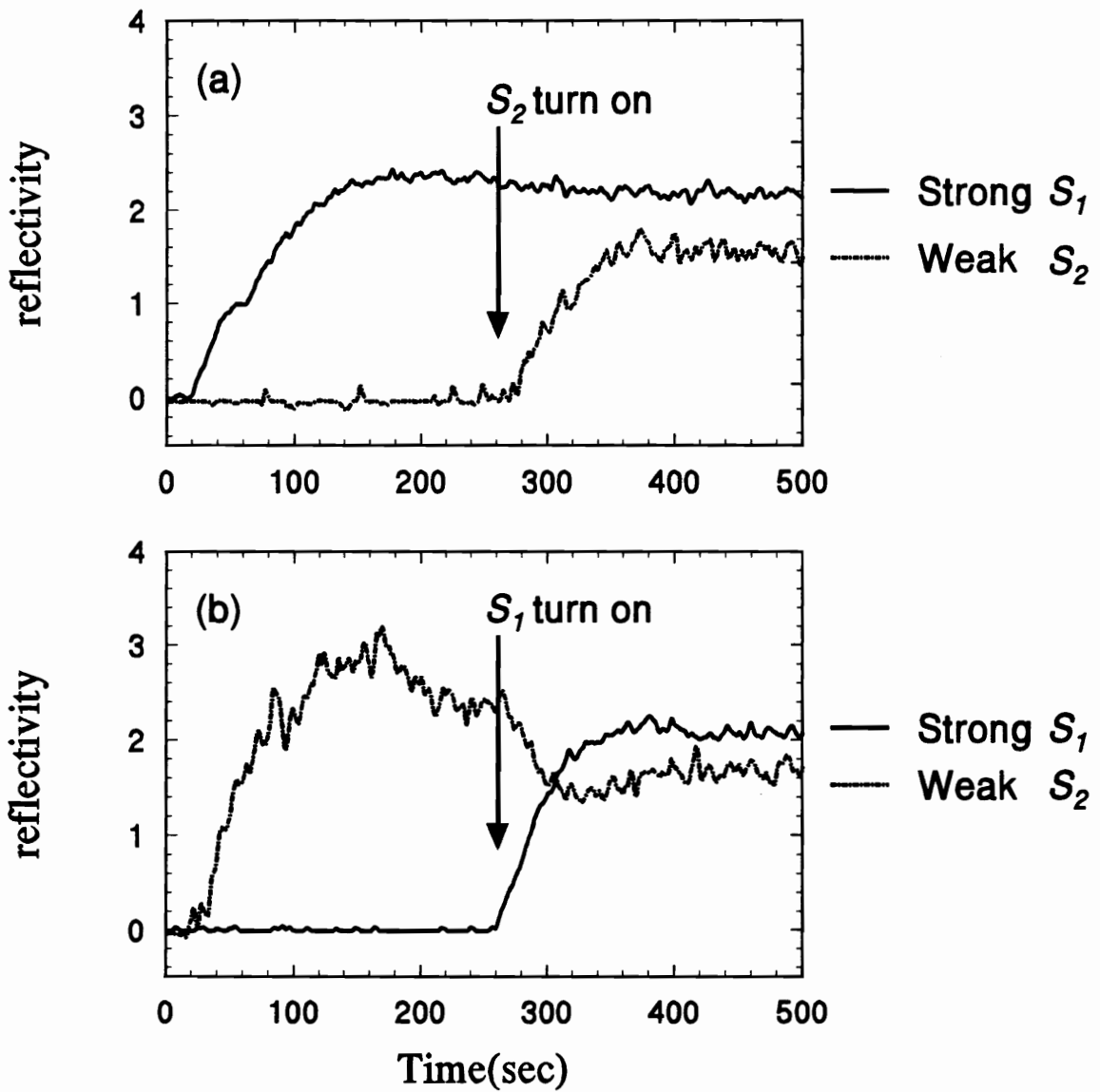


Figure 6.11: Results of an experiment showing the competition between a strong and a weak signal sharing the same interaction region in the PCM. In (a), the strong beam S_1 is first turned on, and the weak beam S_2 is then turned on when S_1 has reached its steady state. In (b), the weak beam S_2 is first turned on, and the strong beam S_1 is then turned on when S_2 has reached its steady state. These results show that a photorefractive PCM favor the strong grating at the expense of the weaker one.

6.4 Conclusion

An optical implementation of the Gerchberg algorithm was described, the experimental result of which seems to indicate that recovery using Gerchberg-type algorithms is feasible optically but only for a class of objects consisting of very few pixels. These limitations were to be expected from the nature of the problem. Some technical problems, such as the finite coherence length of the laser and stabilization of the phase of the feedback, were also identified. In addition to these problems, the PCM displays a competition when multiple beams are present in the interaction region. Additional studies are needed to understand this phenomenon quantitatively.

Chapter 7

Summary

To explore the possibility of using a PCM cavity in iterative image processing, a new theory, based on operators, was developed to describe the steady-state output of the cavity. Using an appropriate expansion of the cavity fields into eigenfunctions of the forward and feedback operators, the transfer characteristics of the cavity were found. These characteristics make a PCM cavity different from a conventional cavity. The three most significant characteristics were identified. They are the need for a two-path geometry, the dependence of the feedback on the PCM phase rather than cavity length, and the cancellation of phase operations. The first two characteristics have been discussed elsewhere, and the third characteristic is a new discovery of this dissertation. The cancellation of operations using phase-filters in the cavity automatically ensures a closed-loop operator with real eigenvalues. It therefore seems that there are no restrictions to the class of signals that can be processed, and that the cavity can accommodate a broad class of band-limited functions.

To delineate further the potentials of a PCM cavity in image processing, several applications of the cavity were described under the framework of the (idealized) steady-state theory. It was shown that contrast enhancement, transfer function synthesis to achieve inverse filtering, and image restoration based on the Gerchberg algorithm can probably be implemented in this kind of cavity. In the computer simulation of the Gerchberg algorithm, the results showed that a band-limited image could be restored

using iterations at least in a noise-free environment. However, the results also showed that it took a large number of iterations to achieve a substantial enhancement, and the more complicated the objects the larger the number of required iterations.

An experimental investigation of the PCM cavity was then carried out. The cavity was built using a PCM that can achieve gain and restore phase errors. For this PCM, a four-wave mixing geometry using a photorefractive BaTiO₃ crystal was chosen. The advantages of using BaTiO₃ for the PCM are that it requires low pump-powers, and that it has large electro-optic coefficients when compared with other materials. Using the extraordinary polarization in all the beams, a maximum reflectivity of about seven was achieved with external angles of incidence of 8° for the signal and 50° for the pump beam. The powers of the pumps were 110 μW for I_1 and 50 μW for I_2 with an unexpanded beam diameter of about 1 mm.

A stable output of the feedback cavity requires a stable feedback and a stable PCM reflectivity. To achieve a stable feedback environment, an optical table and a plastic box were used to minimize the influence of the external mechanical vibration and the effect of air current. The reflectivity of the PCM was stabilized by inserting a neutral-density filter in the beam path. The neutral-density filter acted as a double-loss filter to the signal which re-enters the laser and perturbs its output. It was found that a neutral density filter of optical density 1 was sufficient to stabilize the reflectivity of the PCM.

A PCM cavity is a non-linear feedback system in which self-oscillation and chaos in the cavity field have been observed [75]. Chaotic outputs appeared when the cavity was above threshold of self-oscillation. These chaotic outputs were shown to interfere and degrade a cavity image and should therefore be avoided by tuning the cavity below self-oscillation. The tuning was achieved by adjusting the power of one of the pumps of the PCM, which changed its reflectivity. One indicator showing how close the cavity is to the threshold was the decay time of the cavity. It was found that the cavity field decay time diverges when the cavity is close to threshold. Therefore by monitoring the decay time of the cavity, one can determine how close the cavity is to the threshold.

To verify the theoretical prediction that the cavity can be used in iterative image processing, an experiment was set up to implement an image restoration scheme based on the Gerchberg algorithm. The experimental results showed that optical implementation of the Gerchberg algorithm is possible but it is limited to objects with a few pixels. The results agreed with the conclusion of the computer simulations that the resolution of very simple objects (such as two pixels) can be improved. The spectrum of the improved image showed an extrapolation beyond the low-pass frequencies of the input.

Experiments with a more complicated (three-pixel) object did not show such positive results. This could be due to several factors. First, it was difficult to maintain the phase of the PCM reflectivity constant over a long period of time, because the cavity with a positive feedback was close to threshold. Second, a more complicated object requires a larger number of iterations to produce the same degree of resolution enhancement, but the number of iterations was limited by the coherence length of the laser. Third, the edges of the high-pass mirror were soft and did not reflect much of the information back into the cavity. Finally, with noise present, even the simulation predicts very limited improvement [4].

The experiments also revealed limitations of the PCM itself. It was found that the reflectivity over the PCM may not be uniform as was assumed in the theory. This was particularly noticeable when the objects were comparable in size to the diameter of the pump beams. The nonuniformity may be due to the gaussian distribution of the intensity of the pump beams. One possible method to improve the uniformity of the PCM reflectivity would be to expand and collimate the pump beams.

In conclusion, the optical implementation of iterative algorithms in a PCM cavity seems to be feasible, but it is limited by the restricted class of operations and by the effective number of iterations achievable.

7.1 Recommendation

A system which may be more practical for implementing iterative processing could be a cavity with two PCMs (figure 2.4). Several advantages of a two-PCM cavity make it more attractive than a one-PCM cavity. For example, the reflectivities and the phases of the two paths could be adjusted independently. This would make it possible to achieve negative feedback (by varying the phase of one of the pumps) which is not possible in the one-PCM cavity with one interaction region. Finally, a two-PCM cavity would not have the problem of grating competition which occurs in a one-PCM cavity, because the two sets of gratings would then be located in two different crystals.

The problem of competition in a one-PCM cavity may turn into an advantage in other considerations. For example, signal selection as well as recognition require competition between modes. This competition could be provided by the PCM coupled with an optical cavity. However, more study is needed to better understand the phenomenon of mode competition before it can be implemented and used.

REFERENCES

- [1] R. V. Pole, H. Wieder, and E. S. Barrekette, "Reactive optical information processing. I : Theory of information recovery and resonator mode structure," *Appl. Opt.*, **6**, pp. 1571–1575, 1967.
- [2] J. N. Cederquist, "Optical feedback processing," in *Optical signal processing*, (J. Horner, ed.), pp. 525–565, Academic, 1987.
- [3] P. De Santis, F. Gori, G. Guattari, and C. Palma, "Optical system with feedback," *Opt. Acta*, **23**, pp. 505–518, 1976.
- [4] G. Cesini, G. Guattari, and G. Lucarini, "An iterative method for restoring noisy images," *Opt. Acta*, **25**, pp. 501–508, 1978.
- [5] R. J. Marks II and D. K. Smith, "Iterative coherent processor for bandlimited signal extrapolation," *SPIE International Optical Computing Conference*, **231**, pp. 106–111, 1980.
- [6] D. P. Jablonowski and S. H. Lee, "A coherent optical feedback system for optical information processing," *Appl. Phys.*, **8**, pp. 51–58, 1975.
- [7] P. E. Kotljar, E. S. Nezhvenko, B. I. Spektor, V. I. Feldbush, "Optical processing in feedback systems," in *Optical information processing, Vol. 2*, (E. S. Barrekette, G. W. Stroke, Y. E. Nesterikhin, and W. E. Kock, ed.), pp. 155–170, Plenum, New York, 1976.
- [8] D. Z. Anderson, "Coherent optical eigenstate memory," *Opt. Lett.*, **11**, pp. 56–58, 1986.
- [9] B. H. Soffer, G. J. Dunning, Y. Owechko, and E. Marom, "Associative holographic memory with feedback using phase-conjugate mirrors," *Opt. Lett.*, **11**, pp. 118–120, 1986.
- [10] P. De Santis and F. Gori, "On an iterative method for super-resolution," *Opt. Acta*, **22**, pp. 691–695, 1975.

- [11] T. W. Hansch, F. Varsanyi, and A. L. Schawlow, "Image amplification with dye lasers," *Appl. Phys. Lett.*, **18**, pp. 108–110, 1971.
- [12] R. P. Akins and S. H. Lee, "Coherent optical image amplification by an injection-locked dye amplifier at 632.8nm," *Appl. Phys. Lett.*, **35**, pp. 660–663, 1979.
- [13] F. Laeri, T. Tschudi, and J. Albers, "Coherent CW image amplifier and oscillator using two-wave interaction in a BaTiO₃," *Opt. Comm.*, **47**, pp. 387–390, 1983.
- [14] H. Rajbenbach, Y. Fainman, and S. H. Lee, "Optical implementation of an iterative algorithm for matrix inversion," *Appl. Opt.*, **26**, pp. 1024–1031, 1987.
- [15] J. AuYeung, D. Fekete, D. M. Pepper, and A. Yariv, "A theoretical and experimental investigation of the modes of Optical resonators with phase conjugate mirrors," *IEEE J. Quantum Electron*, **QE-15**, pp. 1180–1188, 1979.
- [16] I. M. Bel'dyugin, M. G. Galushkin, and E. M. Zemskov, "Properties of resonators with wavefront-reversing mirrors," *Sov. J. Quantum Electron*, **9**, pp. 20–23, 1979.
- [17] A. E. Siegman, P. A. Belanger, and A. Hardy, "Optical resonators using phase conjugate mirrors," in *Optical Phase Conjugation*, pp. 465–535, Academic Press, 1983.
- [18] R. A. Fisher, ed., *Optical phase conjugation*. Academic, New York, 1983.
- [19] B. Ya. Zel'dovich, N. F. Pilipetsky, V. V. Shkunov, *Principles of phase conjugation*. Springer-Verlag, Berlin, 1985.
- [20] J. Feinberg, D. Heiman, A. R. Tanguay Jr., and R. W. Hellwarth, "Photorefractive effects and light induced charge migration in Barium Titanate," *J. Appl. Phys.*, **51**, pp. 1297–1305, 1980.
- [21] B. Fischer, M. Cronin-Golomb, J. O. White, A. Yariv, and R. Neurgaonkar, "Amplifying continuous wave phase conjugate mirror with Strontium Barium Niobate," *Appl. Phys. Lett.*, **40**, pp. 863–865, 1982.
- [22] R. W. Gerchberg, "Super-resolution through error energy reduction," *Opt. Acta*, **21**, pp. 709–720, 1974.
- [23] L. J. Cutrona, E. N. Leith, L. J. Porcello, W. E. Vivian, "On the application of coherent optical processing techniques to synthetic-aperture radar," *Proc. IEEE*, **54**, pp. 1026–1032, 1966.
- [24] E. N. Leith and J. Upatnieks, "Wavefront reconstruction with diffused illumination and three-dimensional objects," *J. Opt. Soc. of Am.*, **54**, p. 1295, 1964.

- [25] A. VanderLugt, "Signal detection by complex spatial filtering," *IEEE Trans. on Inf. Theory*, **IT-10**, pp. 139–145, 1964.
- [26] J. L. Horner and P. D. Gianino, "Phase-only matched filtering," *Appl. Opt.*, **23**, pp. 812–816, 1984.
- [27] P. N. Tamura and J. C. Wyant, "Matrix multiplication using coherent optical techniques," *Proc. SPIE : Optical Information Processing*, **83**, pp. 97–104, 1976.
- [28] L. J. Cutrona, E. N. Leith, C. J. Palermo, and L. J. Porcello, "Optical data processing and filtering systems," *IRE Trans. Inf. Theory*, **IT-6**, pp. 386–400, 1960.
- [29] J. W. Goodman, "Operations achievable with coherent optical information systems," *Proc. IEEE*, **65**, pp. 29–38, 1977.
- [30] D. G. Feitelson, *Optical computing : A survey for computer scientists*. The MIT Press, 1988.
- [31] M. O. Hagler and S. V. Bell, "Nyquist stability conditions for laser feedback amplifiers with Gaussian or Lorentzian gain profiles," *J. Opt. Soc. of Am. A*, **3**, pp. 308–318, 1986.
- [32] P. N. Tamura and J. C. Wyant, "On-axis coherent feedback system for image processing," *Proc. SPIE/OSA on Image Processing*, **74**, pp. 57–61, 1976.
- [33] S. H. Lee, "Optical analog solution of partial differential and integral equations," *Opt. Eng.*, **24**, pp. 41–47, 1985.
- [34] H. Rajbenbach, Y. Fainman, and S. H. Lee, "Optical implementation of an iterative algorithm for matrix inversion," *Appl. Opt.*, **26**, pp. 1024–1031, 1987.
- [35] J. Cederquist and S. H. Lee, "The use of feedback in optical information processing," *Appl. Phys.*, **18**, pp. 311–319, 1979.
- [36] A. W. Lohmann, "Suggestions for hybrid image processing," *Opt. Comm.*, **22**, pp. 165–168, 1977.
- [37] G. Hausler and A. Lohmann, "Hybrid image processing with feedback," *Opt. Comm.*, **21**, pp. 365–368, 1977.
- [38] T. Sato, K. Sasaki, and R. Yamamoto, "Image processing system using incoherent image feedback," *Appl. Opt.*, **17**, pp. 717–720, 1978.
- [39] J. Goodman, *Introduction to Fourier Optics*. McGraw-Hill, 1968.
- [40] I. Stakgold, *Boundary value problems of Mathematical Physics, Vol I*. The MacMillan Company, 1967.

- [41] S. H. Lee, B. Bartholomew, J. Cederquist, "Two improved coherent optical feedback systems for optical information processing," *SPIE Semin. Proc.*, **83**, pp. 78–84, 1976.
- [42] J. Cederquist and S. H. Lee, "Coherent optical feedback for the analog solution of partial differential equations," *J. Opt. Soc. of Am.*, **70**, pp. 944–953, 1980.
- [43] J. Cederquist and S. H. Lee, "Confocal feedback systems with space variance, time sampling, and secondary-feedback loops," *J. Opt. Soc. of Am.*, **71**, pp. 643–650, 1981.
- [44] S. Johnston and S. H. Lee, "Confocal optical feedback processing system : an improved optical design," *Appl. Opt.*, **22**, pp. 1431–1438, 1983.
- [45] P. A. Belanger, A. Hardy, and A. E. Siegman, "Resonant modes of optical cavities with phase conjugate mirrors," *Appl. Opt.*, **19**, pp. 602–609, 1980.
- [46] J. F. Lam and W. P. Brown, "Optical resonators with phase-conjugate mirrors," *Opt. Lett.*, **5**, pp. 61–63, 1980.
- [47] M. Cronin-Golomb, B. Fischer, S. K. Kwong, J. O. White, and A. Yariv, "Non-degenerate optical oscillation in a resonator formed by two phase conjugate mirrors," *Opt. Lett.*, **10**, pp. 353–355, 1985.
- [48] G. Indebetouw, and K. P. Lo, "Real time Moire interferometry using a Fabry-Perot cavity with a phase conjugate mirror," *Appl. Opt.*, **28**, pp. 3893–3896, 1989.
- [49] H. Klumb, A. Herden, T. Kobialka, F. Laeri, and T. Tschudi, "Active coherent optical feedback system with phase-conjugating image amplifier," *J. Opt. Soc. of Am. B*, **5**, pp. 2379–2385, 1988.
- [50] B. R. Frieden, "Image enhancement and restoration," in *Picture processing and digital filtering*, (T. S. Huang, ed.), ch. 5, Springer-Verlag, 1979.
- [51] C. K. Rushforth, "Signal restoration, functional analysis, and Fredholm integral equations of the first kind," in *Image recovery: Theory and application*, (H. Stark, ed.), ch. 1, Academic Press, 1987.
- [52] C. K. Rushforth and R. L. Frost, "Comparison of some algorithms for reconstructing space-limited images," *J. Opt. Soc. of Am.*, **70**, pp. 1539–1544, 1980.
- [53] D. Slepian and H. O. Pollak, "Prolate spheroidal wave functions, Fourier analysis, and uncertainty-I," *Bell Syst. Tech. J.*, **40**, pp. 43–63, 1961.
- [54] B. R. Frieden, "Prolate spheroidal wavefunctions," in *Progress in Optics IX*, (E. Wolf, ed.), ch. 8, pp. 313–407, North-Holland, 1971.

- [55] IMSL, *Math library routine*. IMSL, 1989.
- [56] W. H. Press, B. P. Flannery, S. A. Teukolsky, and W. T. Vetterling, *Numerical recipes. "Fortran version."*. Cambridge University Press, 1989.
- [57] A. Papoulis, "A new algorithm in spectral analysis and band-limited extrapolation," *IEEE Trans. on Circuits and Systems*, **CAS-22**, pp. 735–742, 1975.
- [58] R. J. Marks II, "Coherent optical extrapolation of 2-D band-limited signals : processor theory," *Appl. Opt.*, **19**, pp. 1670–1672, 1980.
- [59] A. Ashkin, G. D. Boyd, J. M. Dziedzic, R. G. Smith, A. A. Ballman, J. J. Levinstein, and K. Nassau, "Optically-induced refractive index inhomogeneties in LiNbO_3 and LiTaO_3 ," *Appl. Phys. Lett.*, **9**, pp. 72–74, 1966.
- [60] F. S. Chen, "A laser-induced inhomogeneity of refractive indices in KTN," *J. Appl. Phys.*, **38**, pp. 3418–3420, 1967.
- [61] F. S. Chen, "Optically induced change of refractive indices in LiNbO_3 and LiTaO_3 ," *J. Appl. Phys.*, **40**, pp. 3389–3396, 1969.
- [62] F. S. Chen, J. T. LaMacchia, and D. B. Fraser, "Holographic storage in Lithium Niobate," *Appl. Phys. Lett.*, **13**, pp. 223–225, 1968.
- [63] J. B. Thaxter and M. Kestigian, "Unique properties of SBN and their use in a layered optical memory," *Appl. Opt.*, **13**, pp. 913–924, 1974.
- [64] J. P. Huignard, J. P. Herrian, and F. Micheron, "Optical storage in $\text{LiNbO}_3 : \text{Fe}$ with selective erasure capability," *Rev. Phys. Appl.*, **10**, pp. 417–423, 1975.
- [65] N. V. Kukhtarev, V. B. Markov, S. G. Odulov, M. S. Saskin, and N. L. Vinetskii, "Holographic storage in electro-optic crystals," *Ferroelectrics*, **22**, pp. 949–960, 1979.
- [66] T. J. Hall, R. Jaura, L. M. Connors and P. D. Foote, "The photorefractive effect - A review," *Prog. Quant. Electr.*, **10**, pp. 77–146, 1985.
- [67] A. Yariv, *Optical Electronics*. Holt, Rinehart and Winston, Inc, 1985.
- [68] M. Cronin-Golomb, B. Fischer, J. O. White, and A. Yariv, "Theory and applications of four-wave mixing in photorefractive media," *IEEE J. Quantum Electron*, **QE-20**, pp. 12–30, 1984.
- [69] D. W. Vahey, "A nonlinear coupled-wave theory of holographic storage in ferroelectric materials," *J. Appl. Phys.*, **46**, pp. 3510–3515, 1975.
- [70] Y. Fainman, E. Klancnik, S. H. Lee, "Optimal coherent image amplification by two-wave coupling in photorefractive BaTiO_3 ," *Opt. Eng.*, **25**, pp. 228–234, 1986.

- [71] M. B. Klein, "Photorefractive properties of BaTiO₃," in *Photorefractive materials and their application (I)*, (P. Gunter and J.-P. Huignard, ed.), pp. 195–236, Springer-Verlag, 1988.
- [72] H. Kogelnik, "Holographic image projection through inhomogeneous media," *Bell Syst. Tech. J.*, **44**, p. 2451, 1965.
- [73] J. E. Ford, Y. Fainman, and S. H. Lee, "Enhanced photorefractive performance from 45°-cut BaTiO₃," *Appl. Opt.*, **28**, p. 4808, 1989.
- [74] K. D. Moller, *Optics*. University Science Books, 1988.
- [75] G. C. Valley and G. J. Dunning, "Observation of optical chaos in a phase-conjugate resonator," *Opt. Lett.*, **9**, pp. 513–515, 1984.
- [76] H. M. Gibbs, F. A. Hopf, D. L. Kaplan, and R. L. Shoemaker, "Observation of chaos in optical bistability," *Phys. Rev. Lett.*, **46**, pp. 474–477, 1981.
- [77] R. S. Gioggia and N. B. Abraham, "Routes to chaotic output from a single-mode, DC-excited laser," *Phys. Rev. Lett.*, **51**, pp. 650–653, 1983.
- [78] S. S. Lafleur and R. C. Montgomery, "Real-time dynamic holographic image storage device, U.S. patent number 4,913,534," *Appl. Opt.*, **29**, p. 3976, 1990.
- [79] Y. A. Anan'ev and A. Y. Bekshaev, "More about the problem of superresolution in optics," *Opt. Spectrosc. (USSR)*, **64**, pp. 139–141, 1988.

VITA

Kanwai Peter Lo was born on June 23, 1961 in Hong Kong. He received his Bachelor of Science at the Hong Kong Baptist College in June, 1984. He then came to Virginia Tech in September, 1984, and received his Doctor of Philosophy in September, 1991.